RICE UNIVERSITY

Filtration of Complex Suspensions Using Nanofiltration and Reverse Osmosis Membranes: Foulant-Foulant and Foulant-Membrane Interactions
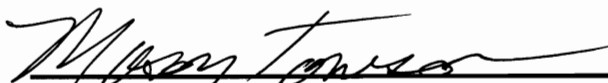
by

Alison Eleanore Contreras

A THESIS SUBMITTED
IN PARTIAL FULFILLMENT OF THE
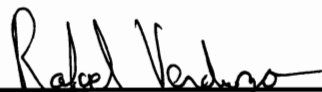REQUIREMENTS FOR THE DEGREE

Doctor of Philosophy

APPROVED, THESIS COMMITTEE

Qilin Li, Chair, Assistant Professor, Civil and
Environmental Engineering, Rice University

Mason B. Tomson, Professor, Civil and
Environmental Engineering, Rice University

Rafael Verduzco, Louis Owen Assistant
Professor, Chemical and Biomolecular
Engineering, Rice University

Albert S. Kim, Associate Professor, Civil and
Environmental Engineering, University of
Hawaii at Manoa

HOUSTON, TEXAS
April 2011

Abstract

Filtration of Complex Suspensions Using Nanofiltration and Reverse Osmosis Membranes: Foulant-Foulant and Foulant-Membrane Interactions

by

Alison Eleanore Contreras

Membrane filtration is a promising advanced treatment method that has the technological capability to treat waters containing contaminants that typically escape traditional water treatment methods, including trace micro-pollutants as well as high salt concentrations. The accurate prediction of nanofiltration and reverse osmosis membrane performance in industrial applications is dependent upon understanding the fouling behavior of representative feed solutions. Combining conventional crossflow filtration experiments and characterization of foulant-foulant and foulant-membrane interactions, three mechanisms involved in combined fouling of organic and inorganic colloidal foulants are identified: increased hydraulic resistance of the mixed cake layer structure, hindered foulant diffusion due to interactions between solute concentration polarization layers, and changes in colloid and membrane surface properties due to organic adsorption. A range of typical organic foulants that exhibited different interactions in the membrane system were studied in combination with inorganic silica on low and high salt-rejecting membranes. Autopsying of the fouled membrane using

transmission electron microscopy (TEM) helped identify combined fouling layer structure. Direct organic adsorption of BSA onto inorganic colloids was shown to cause the greatest synergistic fouling through creation of an aggregated fouling layer structure. A stratified, active salt-rejecting layer of natural organic matter minimizes cake enhanced osmotic pressure (CEOP) and reduces fouling. The presence of divalent ions can lead to the creation of salt concentrating layers by causing aggregation of alginate molecules and enabling CEOP.

The effect of membrane surface chemistry on adsorptive fouling by organics was studied using self-assembled monolayers (SAMs) with different ending functionalities. Surfaces were characterized by hydrophobicity and surface free energy incorporating van der Waals and Lewis acid-base interactions. Acid-base interactions were dominant for all model membrane surfaces tested and total interfacial energies predicted natural organic matter and polysaccharide adsorption, but do not account for protein adsorption. Specific interactions, such as hydrogen bonding and electrostatic interaction between specific functionalities, play a more important role than non-specific electrostatic and hydrophobic interactions in adsorption of and irreversible fouling by proteins. Therefore, surface modifications of NF and RO membranes that minimize –COOH and –NH$_2$ as well as other charged sites may be an effective approach to develop fouling resistant membranes.

Acknowledgments

I first wish to express my sincere gratitude to my advisor Dr. Qilin Li for her guidance and insight throughout this PhD. research. Her knowledge and mentoring has helped shape me into a better researcher and scientist both in and outside of the laboratory. I would like to thank Dr. Mason Tomson, Dr. Albert Kim, and Dr. Rafael Verduzco for serving on my committee, for their interest in my research, and for their willingness to provide comments and critiques throughout this process. I would also like to sincerely thank Bo Chen and Wenhua Guo for their guidance in both XPS and TEM. Additionally, I thank my friends in the department and my research group, Liga, Yu-sik, Sen, Jianwei, Jinjian, Xiaolei and Cong, for their continued feedback, encouragement, and company during these past few years.

Finally, I would like to thank my family and friends for serving as the foundation upon which I am able to succeed at all. I whole-heartedly appreciate your advice, words of encouragement, and continuous loving support throughout this process. Mom and Dad, who knew 10 years ago what that decision to come to Rice would result in! Bethany and Saby, your generosity is unparalleled and I thank you for literally providing me a place to call home this final year. And finally Michael, thank you for your unwavering support and faith in me. I could not have done it without your support. Together, with God, we will make it through it all.

Contents

List of Figures

List of Tables

Chapter 1

Introduction

Increased development in regions with limited freshwater resources has led to necessary development of drinking water treatment technologies that treat non-traditional water sources. Membrane filtration is a promising advanced treatment method that has the technological capability to treat waters containing contaminants that typically escape traditional water treatment methods, including trace micro-pollutants and salts. However, the high operational costs associated with high pressures necessary to counterbalance decreased productivity as a result of membrane fouling remains the largest barrier to its widespread use. A better understanding of the mechanisms responsible for membrane fouling is necessary for developing more effective pre-treatment steps and chemical cleaning protocols as well as developing more fouling resistant membranes.

Most previous studies on membrane fouling have focused only on a single, well characterized foulant of homogenous physico-chemical properties (referred to in this paper as single fouling)[1, 2]. One marked limitation in applying the theoretical and experimental results obtained from these studies to water and wastewater filtration systems is that fouling in these systems is almost always caused by more than one type of contaminant with various particle/molecular sizes and surface characteristics, most commonly both colloidal materials and dissolved organic macromolecules, e.g., natural organic matter (NOM) and soluble microbial products. Previous studies on filtration of complex solutions (i.e., solutions containing both dissolved organic matter and colloids) have shown conflicting results, depending on the foulant used and the salt rejection of the membrane studied. The first part of this thesis focuses on understanding mechanistically the fouling behaviors of both high (reverse osmosis) and low (nanofiltration) salt-rejecting membranes that occur during filtration of a complex solution. In this study we explore not only the interactions between foulants, but also the interactions between the foulants and the membrane surface.

The second part of this thesis develops as the importance of the interactions between the membrane surface and the foulants emerges. Different theories have been applied to explain the membrane fouling behavior as a result of organic adsorption onto the membrane surface due to hydrophobic, entropic, and electrostatic interactions, but there is a lack in consistency in terms of the interactions involved and the goal of predicting fouling behavior based on foulant and membrane surface properties remains elusive. In the second part of this thesis,

the impact of specific membrane surface chemical functionalities as well as the molecular characteristics of organic foulants on adsorptive fouling is investigated using novel experimental techniques that allow molecular level characterization of the adsorption process. The adsorptive behavior is analyzed in terms of interfacial free energies. Additionally, different cleaning protocols are explored to understand mechanistically the effectiveness of various cleaning agents in eliminating fouling due to organic adsorption.

1.1. Organization of Thesis

The thesis consists of eight chapters. Chapter 2 presents a literature review on membrane chemistry and formation, factors that affect membrane fouling, both empirical and predictive membrane flux decline models, and organic adsorption. Chapter 3 contains a published journal article produced from this PhD. study entitled *Combined Fouling of Nanofiltration Membranes: Mechanisms and Effect of Organic Matter* (Journal of Membrane Science, Volume 327, Issues 1-2, 5 February 2009, Pages 87-95). Chapter 4 contains a manuscript in preparation for submission to Journal of Membrane Science concerning combined fouling mechanisms of both nanofiltration and reverse osmosis membranes, entitled *Comparing Structure and Resistance of Combined Organic and Colloidal Fouling Layers Formed During Nanofiltration and Reverse Osmosis*. Chapter 5 consists of a manuscript that is currently under review for publication at Environmental Science and Technology entitled *Studying the Impact of Membrane Surface Chemistry on Adsorption and*

Cleaning of Organic Foulants using QCM-D. It explores the effect of membrane surface chemistry on adsorption of common organic foulants in water and wastewater. Chapter 6, a manuscript in preparation for submission to Journal of Membrane Science entitled, *Surface and Interfacial Free Energy Analysis for Characterizing Organic Foulant Adsorption on Membrane Surface Functionalities* explores a more in-depth approach to predicting organic adsorption onto functionalized surfaces using a thermo-dynamic approach. Finally, in Chapter 7 a protocol for developing fully and semi-aromatic membrane surfaces mounted on a solid substrate for creating specialized membrane surface chemistry for use in a variety of instrumental techniques where membranes are not currently used is explored. A conclusion and summary of the work is included in Chapter 8. A list of nomenclature (including Roman and Greek characters, as well as abbreviations) used in the thesis is included after the References. Additional appendices are references that include detailed characterization of model foulants used in both filtration and adsorption experiments (Appendix A), the statistical tools used (Appendix B), information on chemical structures of the alkanethiol self-assembled monolayers (SAMs) (Appendix C), and finally, the abstract of a co-authored paper on modeling of combined fouling during dead-end filtration published in Langmuir 2009, *25 (14),* 7815-7827, entitled, *Fundamental Mechanisms of Three-Component Combined Fouling with Experimental Verification* (Appendix D).

Chapter 2

Literature Review

Membrane filtration is a promising water treatment technology that converts natural and waste waters into clean water using pressure driven flow across a selective barrier. This technology has practical application in drinking water purification, desalination, wastewater recycling, water softening and the food processing industry. The separation process purifies water by allowing water molecules to pass through the membrane barrier while retaining suspended solids and other substances on the membrane surface. Different types of membranes may be employed for liquid separation applications, including microfiltration (MF), ultrafiltration (UF), nanofiltration (NF) and reverse osmosis (RO) membranes, depending on both the quality of source water used and permeate water desired.

The pore-size for each membrane type vary distinctly, from MF membranes, which have the largest pore-size that allows for the separation of only the largest

contaminants, to RO membranes, which do not have physical pores and only filter through diffusion. RO membranes can exclude all substances except for water molecules, making it a useful technology for desalination. Figure 2.1 shows specifically what size range of foulant each membrane can filter and example foulants within that size range.

Figure 2.1 – Separation size range of different membrane technologies.
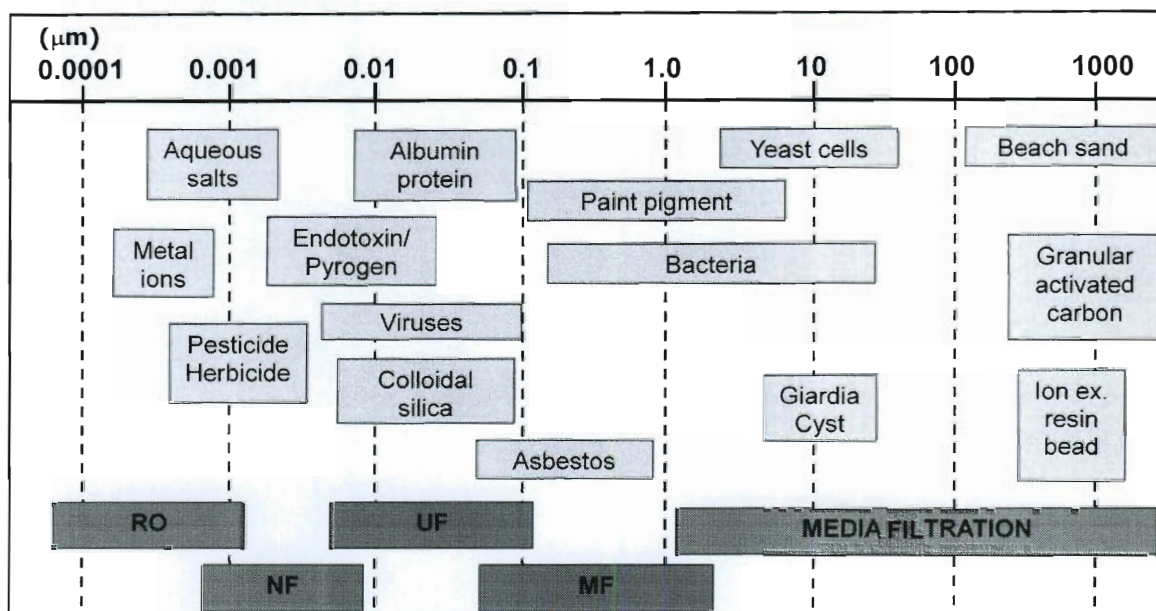
Synthetic membranes used for drinking water treatment can be assembled of both organic and inorganic materials. Organic membranes account for the majority of membranes used (including those in this study) and are typically assembled from

a polymer base, while inorganic membranes can be made of materials such as zeolite, aluminum oxide, or titanium oxide. Membranes can also vary in cross-sectional structure, from symmetric to asymmetric to thin-film composite structures, depending on the method used to cast the membrane. Membrane material and casting method is not chosen arbitrarily but is based on specific factors of the given application and feed water solution characteristics [3]. In thin-film composite NF and RO membranes, a thin separation layer of polyamide is formed on a structural support layer (polysulfone on non-woven support, for example) in order to provide high rejection of salt ions and dissolved materials in the thin separation layer while still being able to withstand high operating pressures with the structural support layer.

MF and UF configurations require minimal pretreatment steps due to their large pore sizes. However, due to increased rejection and consequently increased fouling potential, NF and RO membranes require more involved pretreatment steps. Generally, as membrane rejection increases an increase in operating pressure is also required which results in higher operating costs. The looser MF and UF membranes filter contaminants through size exclusion while tighter membranes (NF and RO) also employ Donnan exclusion (separation based on electrostatic repulsion).

In order to minimize operating costs and maximize clean water production, fouling can be minimized through modification to system conditions. Feed solution composition (i.e. pH, ionic strength, salt and organic composition, temperature), membrane unit geometry, operating pressure, and membrane characteristics (i.e.

surface roughness, zeta potential, hydrophobicity) can all affect the fouling proclivity of a membrane.

2.1. Composition of Nanofiltration and Reverse Osmosis Membranes

Modern reverse osmosis and nanofiltration membranes are predominately thin-film composite (TFC) membranes, consisting of a bi-layer film formed by a two-step process on a re-enforced fabric [4]. The bi-layer is usually a micro-porous structural support layer coated with an ultra thin barrier layer of polymeric composition that can be optimized for the desired flux and rejection properties (seen in Figure 2.2). The ultrathin barrier layer is the thinnest, yet most selective layer since it is in direct contact with the bulk solution. The microporous layer primarily provides the foundation and mechanical stability of the barrier layer during operational high pressures and the reinforcing fabric is also for mechanical stability.

Figure 2.2 – Schematic of a thin-film composite (TFC) membrane and TEM images of the membrane layer[4].
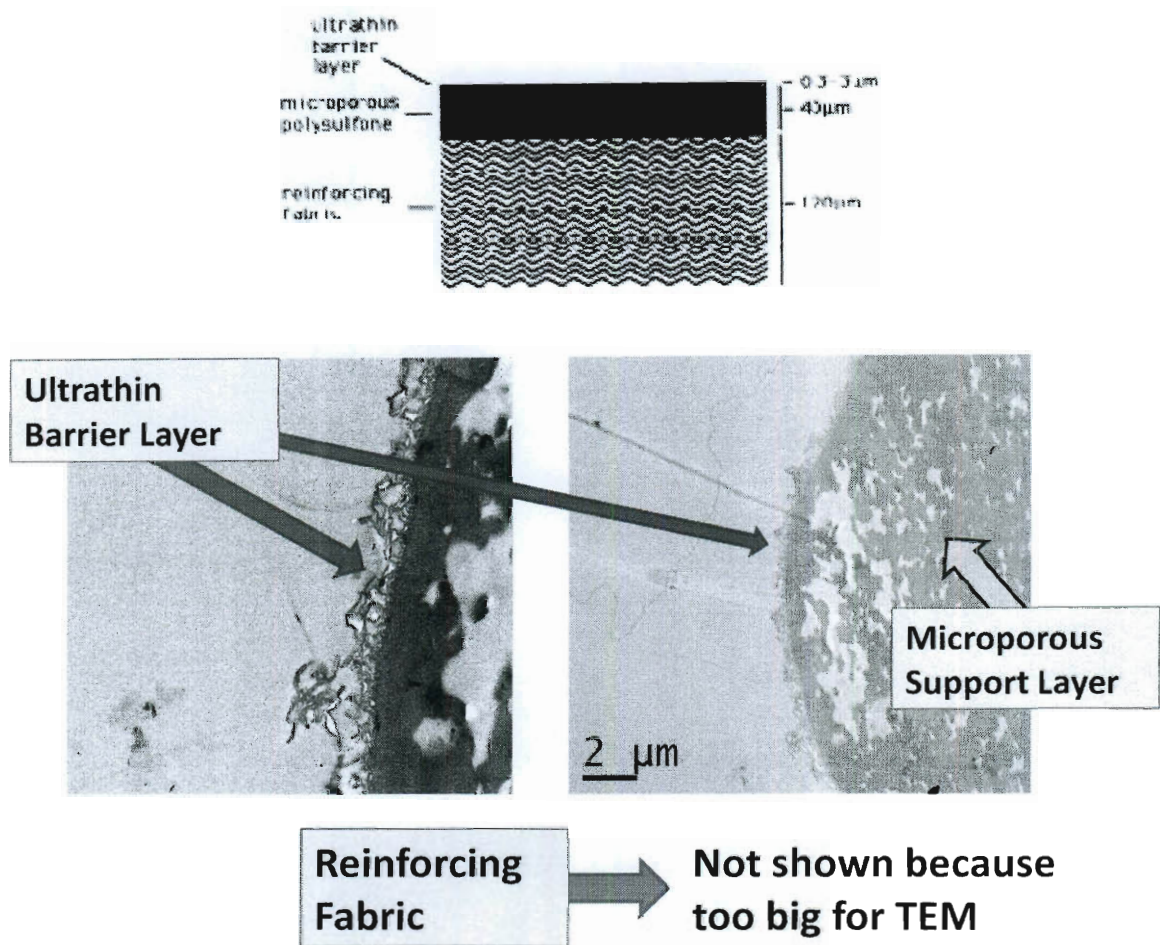
2.1.1. Microporous support layer.

The microporous support layer is typically made of polysulfone, although other polymers such as polycarbonate and poly(phenylene oxide) are also used, and the morphology and chemistry of this layer may influence the formation of the

ultrathin barrier layer. Polysulfone is usually favored for its low cost and strong stability against thermal, mechanical, chemical, and bacterial attack which may occur during filtration [4]. Key factors that control the characteristics of the support layer include choices of solvent, composition of the polymer (including concentration, MW and any additives), and the casting conditions, such as temperature and film thickness [5]. TFC membrane support layers are typically formed through a phase inversion process. The dissolved polymer composing the microporous support layer is spread evenly over the reinforcing fabric with a casting blade and immersed in de-ionized water to induce "phase inversion" – or precipitation into the fabric. The layer is left to soak in water for at least 30 seconds in order to entirely rinse the solvent and then removed, to lightly dry excess water and allow the rest of the moisture to adsorb for preparation of the interfacial polymerization process.

2.1.2. Ultrathin barrier layer.

The ultrathin barrier layer can be formed through several methods. The thin film can be cast separately and laminated to the microporous support, the support layer can be dip-coated into a solution of a polymer and dried in place, or a reactive monomer solution can be dip-coated onto the support layer and post-cured with heat or irradiation [4]. Additionally, another method called interfacial polymerization involves an in situ polycondensation reaction onto the microporous

support layer. At the microporous layer interface, the reaction occurs by bringing two immiscible solvents, amine monomers in aqueous solution and acid chloride monomers in an apolar solvent, into contact. Once in contact, these monomers partition across the interface to polymerize and form a polyamide layer anywhere from 50 to 100 nanometers thick. Due to the low solubility of acid chlorides in water, polymerization primarily occurs in the organic phase and therefore changes to the morphology of the resulting polyamide can be best controlled by altering the solubility and/or diffusivity of the amine. An example of chemistry typical in an interfacial polymerization reaction is seen in Figure 2.3.

Figure 2.3 - Example chemistry of an interfacial polymerization reaction, where a fully aromatic, highly cross-linked polyamide is formed due to the triple –COCl bonds [6]

trimesoyl chloride   1,3-benzenediamine

interfacially formed polyamide
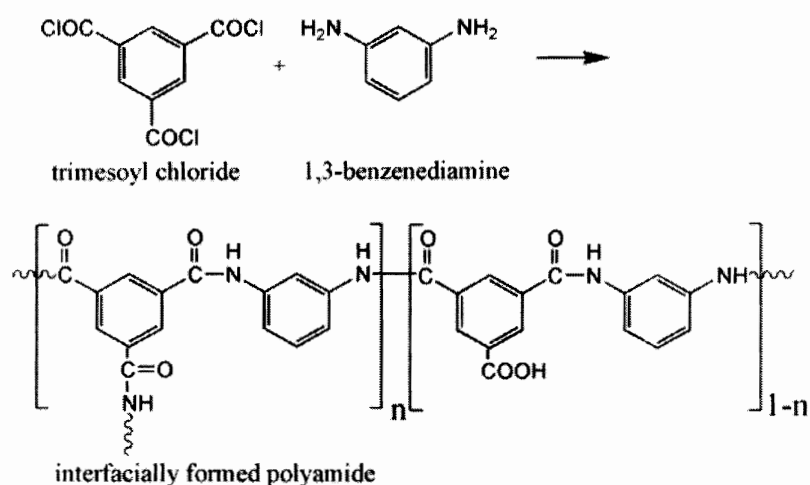
There are several other factors that affect the interfacial polymerization reaction. The concentration of the monomer as well as the chosen organic solvent and its respective properties will govern the amine monomer solubility and diffusivity. Reaction conditions, such as temperature, can affect solvent viscosity which in turn affects diffusivity of the monomers. Additives such as dimethylformamide (DMF), dimethyl sulfoxide (DMSO), NaOH, dimethyl piperazine, and triethanolamine (TEA) can also affect monomer solubility and diffusivity [7]. Heat curing may also be a necessary step to help stabilize the thin films, remove

residual organic solvent, and promote additional cross-linking in the polyamide layer [4].

2.1.3. Composition of commercial membranes.

An analysis of commercially available composite membranes with respect to their chemistries is made difficult due to the patents and proprietary laws protecting the membrane manufacturers and so consequently, very little information about their composition is known [4]. In a few recent studies, however, the physicochemical properties and elemental composition of commonly used commercial membranes have been dissected using a combination of analytical methods, including x-ray photo-electron spectroscopy (XPS), attenuated total reflection Fourier transform infared spectroscopy (ATR-FTIR), atomic force microscopy (AFM), transmission electron microscopy (TEM), and contact angle and streaming zeta potential measurements [6, 8, 9]. These studies were also able to differentiate between membranes with and without surface coatings, which are often added to enhance separation capabilities [4].

NF90 and NF270 (Dow FilmTec, Minneapolis, MN), high and low salt rejecting membranes, respectively, were among the nanofiltration membranes analyzed. LFC1 (Hydranautics, Oceanside, CA) was included in the analysis of reverse osmosis membranes. The NF90 membrane was determined to be an uncoated, fully aromatic polyamide membrane formed by the reaction between 1,3-

benzene-diamine (m-phenylenediamine) and trimesoyl chloride (1,3,5-benzentricarbonyl chloride) [9]. The LFC1 membrane was determined to be made from the same chemistry, but was coated with a polyvinyl alcohol (PVA) layer to create a more ion selective barrier layer. The NF270 was determined to be an uncoated semi-aromatic poly(piperazinamide) membrane formed by piperazine and trimesoyl chloride [9]. The knowledge of the chemical composition of commercially available membrane is useful for synthesizing similar surfaces.

2.2. Membrane Fouling

Membrane fouling can be reversible or irreversible. The original permeate flux of a membrane fouled from reversible fouling can be recovered after system pressure is released and the necessary cleaning protocol (such as backwashing or chemical cleaning) has been performed. Irreversible fouling causes a permanent decrease in membrane productivity through decreased permeate flux even after cleaning has been performed. Irreversible fouling will decrease the integrity of the membrane by reducing its lifetime and productivity.

In order to predict membrane permeate flux decline, a thorough understanding of all contributing fouling mechanisms is required. Membrane fouling occurs as a result of foulants being brought to and accumulating on the membrane surface. Mechanisms leading to flux decline for loose membranes, such

as MF and UF, include pore blocking (when foulants cover membrane pore surfaces) and pore constriction (when foulants reduce pore size by clogging pores). Concentration polarization and cake/gel layer formation are fouling mechanisms of all types of membranes. Fouling during NF and RO is often assumed to occur only on the membrane surface due to the tightness of NF and RO membranes and relative size of the foulants compared to membrane pore size [10].

2.2.1. Typical natural and wastewater foulants.

Feed streams treated by membrane filtration can contain a variety of suspended and dissolved substances depending on the geographical region and source of the water being treated. Typical foulants can be divided into four main categories: suspended inorganic colloids, dissolved organic macromolecules, inorganic precipitates, and bio-foulants (including extracellular polymeric substances or EPS). Colloids are ubiquitous in natural and waste waters and can vary in size from a few nanometers to a few micrometers. Aquatic inorganic colloids consist of clay minerals, colloidal silica, silicates, as well as iron, aluminum, and manganese oxides [11]. Natural organic matter (NOM) and humic substances are major organic foulants present in natural surface waters, while proteins and polysaccharides are found in larger concentrations in waste waters [12]. Additionally, emerging organic micro-pollutants are present at very low concentrations in waste waters (endocrine disrupting compounds (EDCs) and

pharmaceutically active compounds (PhACs)) yet are receiving much attention due to their potential long-term health effects [13, 14]. Scaling of membranes is caused by inorganic components, such as $CaCO_3$ and $CaSO_4$, which complicate fouling by precipitating out of the feed stream and crystallizing on the membrane surface, forming hard mineral deposits [15]. Bio-fouling, the least well understood type of fouling for nanofiltration and reverse osmosis membranes, is the deposition or growth of microorganisms on the membrane surface that results in flux decline [16]. Fouling of solutions containing multiple types of foulants is another situation that is poorly understood. Since individually their fouling mechanisms have been relatively well characterized, this study focuses on the fouling caused by suspended colloids and dissolved organic macromolecules in combination.

2.2.2. Factors affecting membrane fouling.

Fouling behavior is mainly influenced by three factors; hydrodynamic conditions at the membrane surface, membrane surface characteristics, and feed solution characteristics (including foulant characteristics and solution conditions).

2.2.2.1. Hydrodynamic conditions.

Filter geometry is very important during membrane processes, as hydrodynamic conditions determine particle accumulation and fouling layer

formation on the membrane surface, which in turn affects resistance and flux decline. Spiral wound, hollow fiber, plate and frame set-ups are all used in industrial applications. Incorporating spacers into membrane systems (such as the spiral wound set-up) is one way to enhance surface hydrodynamics. While all three configurations can include cross-flow dynamics, spiral wound and hollow fiber membranes have the additional advantage of maximizing membrane filtration area through radial filtration through a tube-like membrane. Seen in Figure 2.4, a cross-flow configuration utilizes tangential dynamics along the surface of the membrane, while a "dead-end" configuration only allows for flow through the membrane (perpendicular to the membrane).

Figure 2.4 - Comparison of cross-flow vs. dead-end filtration.
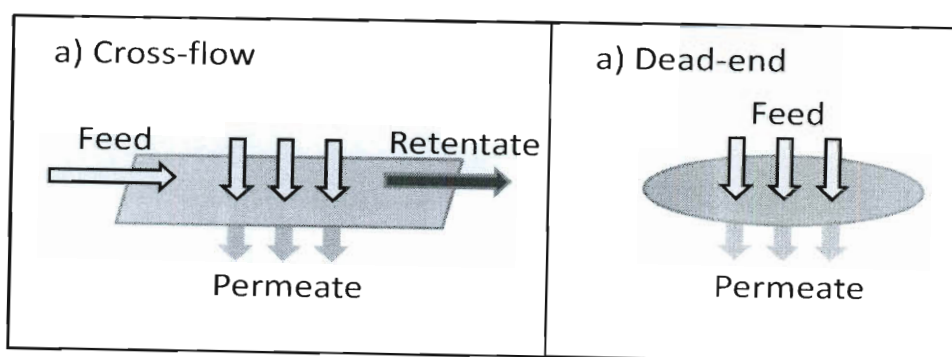
The advantage of cross-flow filtration over dead-end filtration is that accumulation of particles on the membrane surface is reduced [17]. Cross-flow filtration creates shear effects on the surface of the membrane that can help alleviate the formation of thick fouling layers. In cross-flow configurations, the retentate (concentrated water retained by the membrane) can also be recycled back to the beginning to be filtered again, whereas in dead-end filtration the fluid exposed to filtration is limited by permeate flux.

In addition to cross flow rate, operating pressure and permeate flux can also have an impact on fouling behavior [2, 18, 19]. Higher operating pressures result in higher convective transport of foulants, increasing permeate flux through the membrane [2]. However, high operating pressures also has the adverse effect of creating higher permeation drag force and more compressed fouling layers that may counteract the advantage the higher permeate flux produces [18].

2.2.2.2. Membrane characteristics.

Nanofiltration membranes are usually characterized by hydrophobicity, surface roughness, surface charge, molecular weight cut-off (MWCO), permeability, and porosity of the thin outermost layer [10, 20, 21]. The hydrophobicity of nanofiltration membranes is considered one of the most influential factors in membrane fouling [21]. A large portion of fouling is thought to be caused by organic compounds that adsorb on the membrane surface via hydrophobic interactions. If

the membrane surface is charged, electrostatic attraction or repulsion forces between charged foulant components and the membrane surface can also influence the degree of fouling [19].

Colloidal fouling has been shown in most studies to correlate to the roughness of the membrane surface [22, 23]. NF and RO membranes exhibit ridge-and-valley structures on the surface, which could lead to preferential accumulation of small colloids into the valleys (where there is the least resistance) causing a more severe flux decline than smooth membranes [24]. Surface roughness also affects fouling layer morphology, with smooth membranes producing a denser fouling layer than rough membranes, where fouling layers are more open [25]. Membrane permeability can govern flux decline by allowing a faster flow through the membrane. This increased permeate flux rate brings more foulants to the membrane surface, resulting in faster cake layer growth [10].

2.2.2.3. Feed solution characteristics.

Fouling behavior is often dependent on the type of foulant being filtered as characterized by its surface charge, molecular weight or particle size, or hydrophobicity. Solution conditions (i.e. pH, salt ion type, and ionic strength) can affect foulant characteristics, membrane surface properties, and how foulants interact with each other and the membrane surface. Fouling is the greatest during filtration of solutions that have conditions in which foulant molecules are the least

stable and exhibit the weakest attractive interactions [26, 27]. For example, hydrophilic uncharged dissolved foulants exhibited the least fouling at neutral pH, while negatively charged components perform better at high pH [21]. Additionally, organic fouling experiments performed with bovine serum albumin (BSA) on reverse osmosis membranes show that fouling of solutions with a pH close to BSA's iso-electric point (IEP) created the greatest fouling flux decline due to aggregation caused by weakened electrostatic repulsion of the BSA molecules [27]. High ionic strength solutions enhance double layer compression and charge-shielding effects, leading to weaker electrostatic repulsion, also creating more rapid fouling conditions [27]. Solution chemistry can also affect the charge and configuration of organic molecules, such as natural organic matter (NOM). Calcium ions have been shown to significantly enhance fouling in the presence of NOM by forming complexes which result in highly compacted fouling layers and thus more severe flux decline [2, 26, 28].

The strength of the intermolecular adhesion forces between bulk foulants and the membrane surface has been shown to control the rate of fouling [29]. Furthermore, the strength of the foulant-foulant interactions also plays a key role in determining the rate and extent of organic fouling [30]. In a study by Lee and Elimelech (2006) [30], it was found that stronger intermolecular adhesion forces between organic foulants existed under conditions of low pH, high ionic strength and in the presence of calcium ions.

2.3. Single Foulant Filtration

Flux of clean water (m³/m²·s), v_0, through a membrane can be directly related to applied pressure across a membrane through Darcy's law:

$$v_0 = L_p \Delta P = \frac{\Delta P}{\mu R_m}$$
Equation 2.1

where L_p is the permeability of the membrane (m/s·Pa), ΔP is the trans-membrane pressure (Pa), μ is the solution viscosity (Pa·s), and R_m is the hydraulic resistance due to the membrane (m⁻¹). As long as clean water is being filtered, the relationship between flux and applied pressure will remain linear. In the presence of solutes (either salt ions and/or foulants), additional layers of resistance will form at the membrane surface as a result of the rejection of these constituents. During these conditions, the resistance-in-series model expresses membrane permeate flux, v_w, as:

$$v_w = \frac{\Delta P - \Delta \pi_m}{\mu(R_m + R_{cp} + R_f)}$$
Equation 2.2

where $\Delta \pi_m$ is the change in osmotic pressure across the membrane (Pa) due to rejection increasing the concentration of salt ions and R_{cp} and R_f are the hydraulic

resistances due to the foulant concentration polarization (CP) layers (of both salt ions and foulant particles) and the fouling layer (m^{-1}), respectively.

Concentration polarization is the phenomenon in which the solute or particle concentration in the vicinity of the membrane surface is higher than that in the bulk [3]. Concentration polarization is a form of reversible fouling, disappearing as soon as the system pressure is released, and is determined by three transport mechanisms. These mechanisms include: transport to the membrane surface by convective permeate flow, back transport away from the membrane surface by diffusion, and transport along the membrane surface as convective tangential flow [3]. Back transport through diffusion incorporates Brownian diffusion, shear-induced diffusion, and/or inertial lift (for particles << 1µm, shear-induced diffusion and inertial lift are negligible) [1]. Solute transport within the CP layer is often described with the convective diffusion equation:

$$\frac{\partial C}{\partial t} + \vec{v} \cdot \nabla C - \nabla(D\nabla C) = 0$$

Equation 2.3

where D is the back diffusion coefficient, $\vec{v}$ is the permeate flow velocity and C is the concentration of the solute. In the presence of a complex suspension, the diffusion term may be completely different from that when a single non-interacting foulant is present due to solute-solute interactions.

2.3.1. Colloidal fouling.

The fouling layer formed at the membrane surface during colloid filtration is commonly called a cake layer. Two approaches have been used to theoretically describe the formation of a cake layer. In the thermodynamic approach, or phase-transition model [31], concentration polarization transforms into a cake phase only after a certain critical concentration at the membrane surface is exceeded, depending on the pressure of the system and size of particle filtered [32]. This approach simplifies surface interactions [33] and the effect of physical chemical properties of the colloids and membrane surface by assuming that once the critical concentration is reached, all particles transported to the membrane surface deposit.

The other approach, a particle adhesion model, contends that the amount of particles that will deposit on the membrane surface is determined by a particle adhesion probability that considers surface roughness and particle size [34]. The major limitations of this model include the absence of particle or surface interactions during the calculation of particle adhesion probability, concentration polarization effects, and back transport mechanisms. Previous studies have clearly shown that fouling layer formation and membrane flux decline strongly depend on the interactions between the particle and membrane surface [29, 30].

Resistance attributed to the colloidal cake layer (R_c) is calculated through the equation:

$$R_c = \hat{R}_c \frac{m_p}{A_m}$$

Equation 2.4

where $\hat{R}_c$ is the specific resistance of the colloidal cake layer, m_p is the mass of particles deposited on the membrane, and A_m is the membrane area. The specific resistance can be approximated using the properties of spherical particles through the Carman-Kozeny equation [35],

$$\hat{R}_c = \frac{180\mu(1-\varepsilon)}{\rho_p d_p^2 \varepsilon^3}$$

Equation 2.5

where ε is the porosity of the cake layer, ρ_p is the density of the particles (kg/m³), and d_p is the particle diameter (m) [35]. This model assumes a hydrodynamic diameter and the empirical condition of almost touching mono-dispersed, incompressible spheres. The effect of neighboring particles is considered in Happel's cell model, which allocates fluid within a mono-dispersed cake layer to individual solid spheres located in a concentric spherical cell consisting of the sphere and a fluid envelope, on the surface of which tangential stress is nullified [36]. Neither model accurately represents a complex solution with a distribution of particles of different surface characteristics.

2.3.2. Organic fouling.

The fouling layer formed by organic macromolecules is often referred to as a gel layer. Complications arise when modeling gel layers since in addition to convective and diffusive mechanisms, adsorption onto the membrane surface is also involved. Consequently, gel layer formation is much less understood and models predicting flux behavior are mostly empirical or semi-empirical [37, 38]. Pore blocking and pore constriction are also organic fouling mechanisms that only contribute to flux decline during MF and UF [38, 39].

2.4. Filtration of Complex Solutions

One marked limitation in applying the theoretical and experimental results obtained from studies involving one or two foulants to full-scale water and wastewater filtration systems is that fouling in these systems is almost always caused by more than one type of foulant with various particle sizes and surface characteristics, most commonly both colloidal materials and dissolved organic macromolecules, e.g., natural organic matter (NOM) and soluble microbial products. Several studies have identified that poly-dispersed suspensions form cake layer structures with resistances different than mono-dispersed suspensions and that interactions that occur between foulants can be correlated to flux decline behavior [30, 40-43]. There exist several relevant experimental and modeling studies that seek to better understand the fouling

behavior during filtration of complex suspensions. Here, a complex suspension is defined as a solution containing multiple types of foulants of different physico-chemical properties (either size or surface characteristics).

2.4.1. Dual component solutions.

The presence of a cake layer on the membrane surface can also create another fouling mechanism that contributes to an increased flux decline when additional solutes, such as salt ions, are present. The diffusive tortuousity caused by the porosity of a cake layer can hinder the back diffusion of the rejected salt ions, enhancing the concentration polarization of the ions and (through Equation 2.2) decreasing the permeate flux [44, 45]. This effect is called cake-enhanced concentration polarization (CECP) or cake-enhanced osmotic pressure (CEOP) and is observable during filtration by a decrease in salt rejection over time as salt concentration at the membrane surface increases. CECP is verified elsewhere [28] yet is only a significant mechanism when the salt rejection of the membrane is relatively high ($\cong 80\%$) [44].

2.4.2. Triple component solutions.

2.4.2.1. Experimental studies.

Experimental studies observing the combined fouling effect of colloids and organic macromolecules on NF and RO membranes are limited in number and scope. Additionally, conflicting results have been observed. In Lee *et al.* (2005) [28], a combined solution of silica colloids and natural organic matter (NOM) was filtered under different salt conditions on a high salt-rejecting NF membrane. Flux declines of the combined fouling experiments were compared to the additive sums of the individual (either colloid or NOM in solution alone) flux. Combined flux is termed "synergistic" if it is greater than the predicted sum and "reduced" if it is less than the predicted sum. Under several salt conditions – including differing concentrations of NaCl and the presence and absence of $CaCl_2$ – combined fouling experiments show a faster flux decline initially, but a lower flux decline in the latter stages of fouling compared to that predicted by the sum of the individual components. This reduced fouling during combined filtration compared to the additive sum was determined to be from a diminished effect of cake-enhanced concentration polarization (CECP). In combined solutions containing Ca^{2+}, the reduction is attributed to reduced NOM-calcium complexation due to competition between colloidal particles and NOM molecules for calcium ions.

In a similar study done by Li *et al.* (2006) [46], solutions containing both silica colloids and Suwannee River humic acid (SRHA) were filtered using a low salt-

rejecting NF membrane. Using the same comparison described earlier, the combined fouling experiments this time revealed a synergistic fouling effect present during the entire length of the fouling experiments. Because these experiments were performed on a low salt-rejecting membrane, the effect of CECP was not significant and could not be credited as the combined fouling mechanism. Instead, the synergistic behavior was attributed to the hindered back diffusion of the foulants caused by the interaction between the organic and colloid, resulting in a more substantial deposition on the membrane surface. Common to both studies is the observation that combined fouling cannot be predicted from fouling by individual foulants alone.

2.4.2.2. Modeling studies.

Several mathematical models have attempted to predict the flux decline of poly-disperse solutions. A semi-empirical model developed by Dharmappa *et al.* (1992) [43] predicts the fouling of MF and UF membranes during filtration of a poly-dispersed colloidal suspension by assuming that particle accumulation on the membrane surface is governed by deposition and re-suspension of the particles and using mass transport and mass balance equations. Limitations of this model which would prevent its use in modeling NF and RO processes include assumptions of a completely mixed layer (which is likely not the case for all of filtration), incomplete incorporation of back transport mechanisms, omission of the concentration

polarization effect, and the necessity of fitting data due to the empirical nature of the model

A more advanced approach combines the classical filtration theory with the concept of a particle cut-off diameter (under which particles deposit on the membrane) to predict filter cake thickness as a function of time [41]. This approach assumes an incompressible cake of discrete layers, stratified horizontally by average particle size, with the layer consisting of the greatest particle size adjacent to the membrane and the lowest in the outermost layer. The model predicts that as trans-membrane pressure is increased, the deposition of smaller particles increases average specific cake resistance. An analytical method by Kim and Ng (2007) verifies this phenomena by showing that a normal distribution of particle sizes will always exhibit a fouling layer with greater cake resistance (as compared to that of a log-normal distribution) due to the larger number of smaller particles in the normal distribution [47].

A predictive model by Baruah *et al.* [48] anticipates that in a poly-dispersed suspension of colloids and macromolecules flux will be limited by the particle size causing the lowest permeate flux. Using this determined flux, the concentration of each species in the filter cake is back-calculated out to determine the equilibrium concentrations at the membrane surface. Packing densities are explored based on known particle sizes until packing constraints are satisfied and then flux is evaluated. Experimental results show that despite not incorporating particle

interactions, microfiltration of a poly-dispersed solution of macromolecules was accurately predicted [48].

2.5. Organic Adsorption

Organic adsorption has been studied both in the context of membrane filtration as well as other chemical, biological, and medical applications [12, 14, 49-54]. In membrane systems, both specific and non-specific interactions of organic macromolecules with the membrane surface can cause organic adsorption which contributes to flux decline. This is particularly detrimental in nanofiltration and reverse osmosis systems since not only can organic adsorption contribute to a major part of irreversible fouling through strong chemical interactions with the membrane surface, but in the presence of highly concentrated retentate once adhered to the membrane surface some organic matter, such as extracellular polymeric substances (EPS), will further propagate irreversible bio-fouling. In addition to adsorption on the membrane surface, in ultrafiltration and microfiltration organic adsorption into the membrane pores can contribute to pore-constriction and pore-blockage, also resulting in flux decline.

There is evidence that suggests that highly monopolar materials such as polysulfone (PS) and polyethersulfone (PES) favor solute adsorption [55]. Hydrophilic non-interacting membranes are thought to decrease protein

adsorption, even though hydrophobic interaction is not the only interaction involved in adsorption [55]. In a study of nanofiltration membranes, wetting with ethanol and water increased the hydrophilicity of the surface (according to captive bubble technique) [56]. Increased surface roughness has also been found to correlate with increased flux loss due to protein adsorption for ultrafiltration membranes [57].

2.5.1. Theory of organic adsorption.

Organic adsorption is a complicated process that involves van der Waals forces, hydrophobic and electrostatic interactions, and hydrogen bonding. Although nonspecific organic adsorption is complex and not well understood several chemical and physical approaches can be applied to explain these complicated interactions.

Of the various organic macromolecules present in natural and wastewaters, protein adsorption has been the most heavily studied. Extensive work has shown that adsorption of proteins onto solid surfaces is entropically driven [58-66]. Norde *et al.* [66] has shown that upon adsorption, there is an increase in entropy (ΔS_{ads}) that dominates the enthalpic change, resulting in a negative free energy change of adsorption ($\Delta G_{ads} = \Delta H_{ads} - T \Delta S_{ads}$). Expectedly, electrostatic interactions strongly influence not only protein adsorption [58-64, 66], but also protein configuration upon adsorption [67]. "Flat" configurations of proteins were found to occur by adsorbing highly charged polyelectrolyte onto highly charged positive or negative

surfaces [67]. The affinity of a protein to adhere to a surface increases with the hydrophobicity of the surface [54, 68-70] and the concept of using hydrophobicity of membranes to assess their propensity to foul has also been established [55, 56, 71, 72]. This increased fouling propensity is attributed to the fact that hydrophobic membranes prefer to be covered with colloids than water [55].

Protein adsorption can be controlled by changing the bulk solution conditions, including pH and ionic strength. Norde *et. al* has shown that protein adsorption is a strong function of pH, with the highest amount of adsorption occurring near the isoelectric point (IEP) of the protein [58-64, 66]. They claim that adsorption behavior is determined mainly by the structural changes of the molecule at the IEP.

DLVO theory, named for the Dutch and Russian scientists Derjaguin, Landau, Vervey, and Overbeek that simultaneously studied this phenomena, incorporates attractive (van der Waals) and repulsive (electrostatic double layer) interactions to describe the overall stability of hydrophobic colloids [73, 74]. However, too often these two interactions cannot accurately describe the interactions that lead to colloidal membrane fouling [75]. Among a variety of other reasons that the discrepancies may be ascribed to, including chemical and morphological hetereogeneity of the membrane surface [22, 76], additional interactions between the membrane and foulant induced by the polarity of the solvent has also be observed, which lead to the school of thought that proposes an extended DLVO (or xDLVO) approach [77, 78]. The extended DLVO theory includes the additional

short-range acid-base interaction between two surfaces immersed in a polar solvent such as water, quantified by the measurement of surface tensions of various substances. Several studies have shown that polymeric surfaces have a substantial acid-base contribution [55, 71, 78-80]. A few studies have recently shown that extended DLVO theory can be applied to account for organic adsorption during membrane filtration [71, 80].

2.5.2. Experimental methods of measuring adsorption.

The role of organic adsorption in membrane fouling is difficult to determine during cross-flow filtration experiments since it is usually accompanied by gel or cake layer formation, which also causes flux decline. Gravimetric, spectroscopic, and direct protein assays have been used to quantify the thickness or amount of organic adsorption for various applications.

Ellipsometry is an optical method that records the changes in polarization of elliptically polarized light when it reflects on a sample surface [81]. When sampling adsorbed layers, the change in refractive index will cause a change in polarization and the optical thickness of the film can be deduced. One study created gradients of wettability on glass slides via diffusion of dichlorodimethylsilane vapor and then measured the amount of proteins and detergents adsorbed through ellipsometry [54, 82]. This study found that the amount of negatively charged proteins adsorbed

increased with increasing contact angle of the surface, whereas non-ionic and negatively charged detergents did not adsorb to hydrophilic surfaces.

Surface plasmon resonance spectroscopy (SPR) is an optical technique that measures changes in the refractive index of the medium near a metal surface to quantify adsorption. Monochromatic polarized light is reflected from the backside of the glass-gold interface and for thin organic films (<100 nm), the reflected intensity of this light versus the angle of incidence is approximately proportional to the thickness of the film. The major limitation of SPR is that because it measures within a certain boundary of the surface (~200 nm), it is sensitive to both the adsorbed molecules, the dissolved molecules in the bulk medium, and the bulk medium itself [83]. Several studies have successfully compared the adsorption of various organics onto engineered surfaces using SPR [83-86].

Atomic force microscopy (AFM) can measure inter-molecular adhesion forces involved in adsorption at small and precise ranges. In order to consider the effects that protein orientation has on the quantification of protein adsorption, Sethuraman *et al.* sought to quantify the adhesion or pull-off forces between a chosen protein immobilized onto a probe and a self-assembled monolayer coated solid substrate through AFM [68]. Lee *et al.* also used AFM to quantify the intermolecular adhesion forces between model organic foulant and reverse osmosis membranes, correlating increased fouling behavior to high adhesion forces [87].

The quartz crystal microbalance with dissipation (QCM-D) has recently proven to be a sensitive and fundamental tool for measuring macromolecule adsorption in liquid-phase research [88-90]. In this technique, a quartz-crystal sensor with piezoelectric properties is subjected to an electric field, under which it vibrates at a resonant frequency. As a solution containing macromolecules flows past and adsorbs to the surface of the sensor, the frequency of the sensor vibration changes. For thin, rigid, and evenly distributed adsorbed layers, the adsorbed mass of the layer, Δm, can be deduced from the change in resonant frequency, Δf, using the Sauerbrey equation [81]:

$$\Delta m_{s-QCM} = \left(C_{QCM}/n \right) \Delta f \hspace{3cm} \text{Equation 2.6}$$

where C_{QCM} is a mass sensitivity constant based on sensor properties (per overtone number) and n (= 1, 3, 5,...) is the overtone number. The simultaneous dissipation measurement records energy dissipated through the adsorbed layer, which can give insight into the structure of the adsorbed layer.

For two reasons, a non-rigid adsorbed layer is not appropriately modeled using the Sauerbrey equation. Firstly, while a rigid layer acts as a dead mass on the oscillator, a viscoelastic film couples the shear acoustic wave, making Δf not directly proportional to Δm_s. Additionally, a non-rigid layer will include water (or another liquid/solvent) entrapped in the spaces of the adsorbed film, increasing the perceived mass. To analyze a non-rigid adsorbed layer, a Voight-based viscoelastic

model is more appropriate [91-93]. Using this approach, an adsorbed film is represented on the sensor surface using four unknown parameters: ρ_f – film density, d_f – film thickness, μ_f – film elastic modulus, and η_f – film viscosity (Figure 2.5).

Figure 2.5 - Schematic of the geometry and the parameters used to simulate the quartz crystal covered with a viscoelastic protein film with thickness d_f between the sensor surface and a semi-infinite Newtonian liquid. Retrieved from [81].
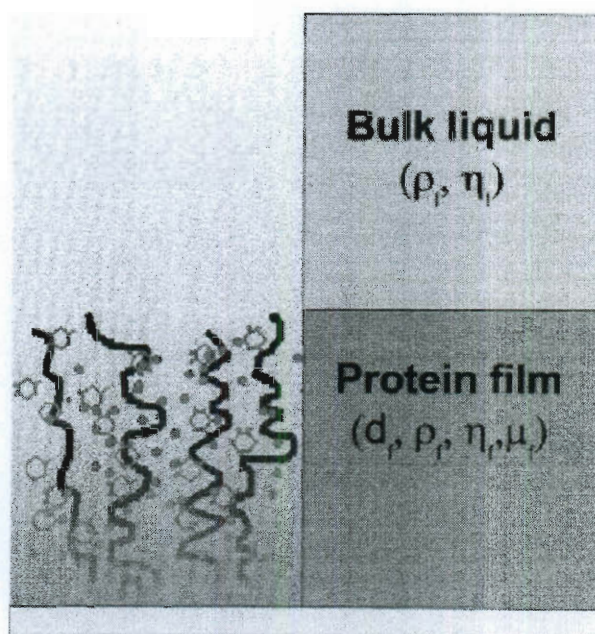
These four unknown parameters cannot be uniquely determined using only two independently measured quantities (Δf and ΔD). However, under the

assumption that the adsorbed film and bulk liquid system exhibits no other frequency dependence (apart from the complex shear modulus introduced via the model), it is possible to obtain a unique combination of these four parameters by using 2 or more harmonics [81]. Comparing the results of the Sauerbrey model to the Voight-model allows for an in-depth analysis of the mass and structure of the adsorbed layer. Several studies have used QCM-D successfully to study adsorption of polymers, surfactants, and organic macromolecules onto gold and modified polymer surfaces [88-90].

Although not capable of quantifying adsorbed organic layers, other techniques have been found to be helpful in analyzing the characteristics of adsorbed films. XPS and FTIR provide information on the chemical composition of the adsorbed layer. Contact angle measurement is usually used to quantify the hydrophobicity of the surface, with measurements above 90° indicating hydrophobic surfaces and below 90° indicating hydrophilic surfaces.

2.5.3. SAMs as model surfaces for organic adsorption.

Organic adsorption studies are limited by the heterogeneity of surfaces upon which adsorption takes place. This is especially challenging with water filtration membranes, whose surfaces are both physically and chemically heterogeneous. Previous studies have examined adsorption on glass and silicon dioxide surfaces, but remain limited by surface flaws that skew adsorption phenomena at the

molecular level [54, 82]. Self-assembled monolayers (SAMs) of long-chain ω-functionalized alkanethiolates prepared on gold films have been established as excellent model systems for studying the interactions of proteins with organic surfaces [94, 95]. Extensive work has been focused on protein adsorption onto monolayers of hydrophobic (methyl-terminated) and hydrophilic (hydroxyl- and hexa(ethylene glycol) terminated) alkanethiols and how to tailor surfaces to create desired degrees of adsorption [84, 86, 94-96]

A common method to form SAMs is through immersion of a clean gold surface into a solution of thiol (see Figure 2.6). Many extensive studies have shown that ω-functionalized alkanethiolates assemble into well-oriented, slightly canted, and closely packed formation, making them good surfaces for adsorption studies due to their consistent coverage. SAMs as model surfaces have been used in the previously discussed measurement techniques, including ellipsometry and SPR, with helpful conclusions [85, 86, 94]. Limited use of SAMs with QCM-D has been reported, although the studies that do exist show that conformational information about the adsorbed layer can be interpreted [97].

Figure 2.6 - Schematic of the synthesis of *n*-alkane-thiol SAMs on gold [98].
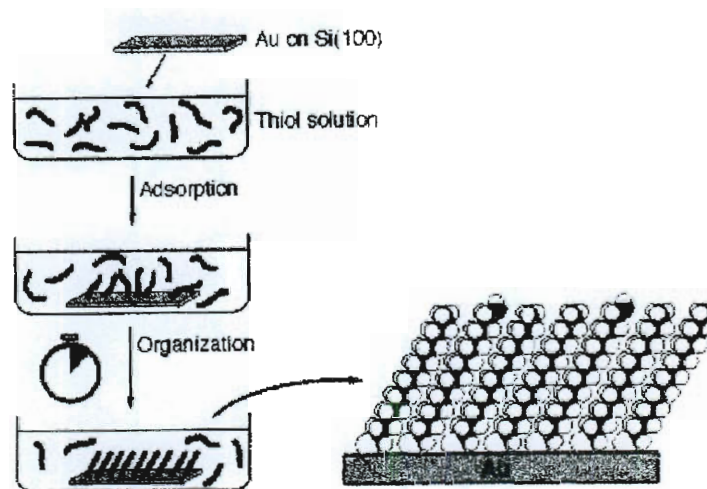
2.6. Membrane Cleaning

A common method of recovering water flux caused by membrane fouling is through membrane cleaning. Backwashing is one method of cleaning ultrafiltration and microfiltration membranes that involves reversing the water flow [99]. In water treatment plants, one membrane module or treatment train will be periodically shut-down for a short amount of time (anywhere from 15 min. to 1 hour [100, 101]) during cleaning while the other trains continue to operate. Foulant is removed through turbulent hydrodynamic forces at the membrane surface that loosens the fouling layer.

Chemical cleaning is a common method of cleaning nanofiltration and reverse osmosis membranes, where backwashing is not physically possible due to membrane asymmetry and tighter pore structures. Cleaning with chemicals works by creating solution conditions favorable for foulant dissolution as opposed to deposition on the membrane surface [102]. Generally, increased temperatures will increase dissolution, however most membrane materials are sensitive to degradation at high temperatures [103]. Cleaning agents accomplish this by changing the morphology of the foulants, the relative activity of the foulant in solution or the interaction between foulants within the fouling layer [29]. Typical cleaning agents include surfactants such as sodium dodecyl sulfate (SDS) and Tween 20, alkaline agents such as sodium hydroxide (NaOH), acidic agents such as hydrochloric acid (HCl), sulphuric acid, citric acid, and oxalic acid, chelating agents such as ethylenediaminetetraacetic acid (EDTA), and enzymes [29, 101, 104-107].

Choosing the most effective chemical cleaning agent is dependent upon a combination of the foulants present in the water and the membrane material. Surfactants are effective at cleaning protein adsorption if the concentration is above a critical micelle concentration [29]. Alkaline chelating agents are efficient at chemical cleaning nanofiltration membranes when fouled by a combination of NOM-metal complexes, however, they can also permanently reduce membrane ion rejection [105]. EDTA is particularly effective at cleaning Ca-organic complexed fouling layers when used at a high enough concentration [29, 102] Inorganic

foulants, however, may not be removed by alkaline agents and may require periodic acidic cleaning [105].

Chapter 3

Combined Fouling of Nanofiltration Membranes: Mechanisms and Effect of Organic Matter[1]

3.1. Introduction

Nanofiltration (NF) is an attractive technology for producing clean water from non-traditional sources, i.e. brackish water and wastewater, since it can provide high multivalent ion and organic contaminant rejection at a much lower operating pressure than reverse osmosis. Unfortunately, as with all membrane

filtration processes, an inherent problem of NF is decreased productivity due to fouling of the membrane by colloidal materials, dissolved organics, inorganic precipitates, and microorganisms. While fouling can be controlled by using low fouling membrane materials [22, 108-110], pre-treatment of the feed stream [111-114], and optimizing the system configuration and operation [26, 44], proper use of these control strategies still requires a deeper understanding of the responsible fouling mechanisms.

Most previous studies on membrane fouling have focused only on a single, well characterized foulant of homogenous physico-chemical properties (referred to in this paper as individual fouling). One marked limitation in applying the theoretical and experimental results obtained from these studies to water and wastewater filtration systems is that fouling in these systems is almost always caused by more than one type of foulant with various particle sizes and surface characteristics, most commonly both colloidal materials and dissolved organic macromolecules, e.g., natural organic matter (NOM) and soluble microbial products. Several studies have identified that poly-dispersed suspensions form cake layer structures with resistances different than mono-dispersed solutions and that interactions that occur between foulants be correlated to flux decline behavior [41-43, 87].

A limited number of studies on combined fouling (i.e., fouling with multiple types of foulants) by both inorganic colloids and dissolved organic matter have shown that fouling behavior differs under varying solution conditions and with

different membrane types [28, 46, 115]. Li *et al.* [46] performed combined fouling experiments with a low salt-rejection NF membrane in the presence of silica colloids and NOM. Flux decline measurements revealed significantly faster membrane fouling in combined fouling experiments than what might be predicted by summing the contributions from each foulant based on the individual fouling experiments. The aggravated membrane fouling or enhanced flux decline, referred to as a synergistic effect, was attributed to the hindered back diffusion of each foulant. In another study performed on a high salt-rejection NF membrane, Lee *et al.* [28] found that flux decline during filtration of a mixture of NOM and silica colloids was initially greater than the sum of the flux declines caused by each foulant individually, but was reduced in the latter filtration stages. It was hypothesized that an "active salt rejecting layer" formed during combined fouling negated the effect of cake-enhanced concentration polarization (CECP), which increases the salt concentration and consequently the osmotic pressure in the concentration polarization (CP) layer of salt ions [44, 45]. It is important to note that although fouling behavior differed according to the experimental conditions of each study, common throughout these studies is the observation that combined fouling cannot be predicted from fouling by individual foulants alone.

The objective of this study was to understand the effects of different organic foulants found in water and wastewater on combined fouling during the nanofiltration of complex solutions containing both colloidal materials and dissolved organic matter. Interactions of four model organic macromolecules with

colloidal silica foulants and the membrane surface were thoroughly characterized and related to membrane flux behavior observed in cross-flow filtration experiments to reveal the different combined fouling mechanisms involved. Results of the study clearly demonstrated the significance of interactions among different foulant types, which has been largely neglected in previous mechanistic studies.

3.2. Theory

Three potential mechanisms have been identified as contributing to the combined fouling flux decline observed during previous combined fouling studies [28, 46, 115]. The weighted effect of each mechanism is anticipated to be different for interacting vs. non-interacting foulants.

3.2.1. Increased cake layer resistance.

Dissolved organic compounds in water and wastewater are much smaller in size compared to colloidal foulants such as silica. It has been shown that poly-dispersity in particle size distribution is likely to affect fouling layer resistance by altering the   structure of the cake/gel layer formed at the surface of the membrane [41, 47, 116].

In the presence of either organics or colloids alone, fouling layer formation is governed by the resistance in series model,

$$v = \frac{\Delta P - \Delta \pi_m}{\mu(R_m + R_c)}$$

Equation 3.1

where v is the permeate flux, ΔP is the applied pressure, $\Delta \pi_m$ is the trans-membrane osmotic pressure, μ is the dynamic viscosity of the solution, R_m is the resistance of the membrane and R_c is the resistance of the cake/gel layer. R_c is determined by the specific resistance of the fouling layer or the fouling layer mass per membrane unit area. For mono-dispersed, spherical colloids, the specific cake resistance is usually estimated using the Carman-Kozeny equation,

$$\hat{R}_c = \frac{180\mu(1 - \varepsilon_c)}{\rho_p d_p^2 \varepsilon_c^3}$$

Equation 3.2

where ε_c is cake layer porosity, ρ_p is solid density of the particle, and d_p is particle diameter. The Carmen-Kozeny equation predicts that decreases in cake porosity and particle diameter result in an increase in the specific cake layer resistance. Although this equation is only applicable for rigid, nearly touching particles, one can imagine that as the porosity of the layer decreases due to the presence of smaller particles filling interstitial pore spaces, as shown in Figure 3.1, for the mixed fouling layer adjacent to the membrane the same relation would be true. Fouling layer

resistance would consequently increase, resulting in increased flux decline. A recent analytical study verified this theory by showing that a cake layer composed of normally distributed particle sizes will always create a higher specific resistance compared to a log-normal distribution with the same mean particle size due to the presence of more small particles in the normal distribution [47].

3.2.2. Hindered back diffusion.

The back diffusion of one foulant type may be hindered by the presence of the concentration polarization of fouling layer of other types of foulants. During filtration, permeate flow brings the solute towards the membrane surface, convective flow transports the solute along the membrane surface tangentially and Brownian diffusion and shear-induced diffusion simultaneously transport the solute back to the bulk fluid. Recently, the Brownian and shear-induced diffusion phenomena were unified using irreversible thermodynamics [117]. For small particles (<< 1 μm), such as the colloidal particles used in this study, shear-induced diffusion is negligible [1]. Accumulation of the solute within the concentration polarization layer can be described by the convective-diffusion equation,

$$\frac{\partial C}{\partial t} + \vec{v}_{w'} \cdot \nabla C - \nabla(D\nabla C) = 0$$

Equation 3.3

where D is the back diffusion coefficient, v_w is the flow velocity, and C is the concentration of the solute. A schematic description is available in Figure 3.1.

The Stokes-Einstein equation (Equation 3.4) can be used to estimate the diffusion coefficient of small, spherical solutes in free solution

$$D_o = \frac{k_B T}{3\pi\mu d_p} \qquad \text{Equation 3.4}$$

where k_B is the Boltzmann constant and T is absolute temperature. When there is significant accumulation of colloids at the membrane surface, i.e. formation of a cake layer, back diffusion of smaller solutes, e.g., dissolved organic foulants, is hindered by the presence of the cake-layer due to the tortuous pathway of transport. The hindered diffusion coefficient is related to the porosity (ε) and tortuousity (τ) of the cake layer [45].

$$D^* = \frac{D_o \varepsilon}{\tau^2} \qquad \text{Equation 3.5}$$

The slower back diffusion leads to faster accumulation of the smaller solutes and hence a higher concentration in the CP layer. This phenomenon has been demonstrated with salt ions - termed cake-enhanced concentration polarization (CECP) - and has been identified as a significant contributor to membrane flux

decline observed in colloidal fouling of NF and RO membranes [44, 45]. CECP is observed by a decrease in the observed salt rejection over time as the concentration of salt at the membrane surface increases.

CECP may also occur for dissolved organic compounds that are small enough to penetrate the colloidal cake layer. As a result, the concentration of dissolved organic foulants in the CP layer is increased and formation of the organic gel layer is accelerated. Meanwhile, the higher organic concentration in the CP layer increases local fluid viscosity. Although only valid at dilute concentrations, the Stokes-Einstein equation predicts that the diffusivity of colloids will be reduced as the local fluid viscosity increases, further accelerating colloidal foulant accumulation at the membrane surface. In reality, higher concentrations at the membrane surface will make colloid-colloid interactions and volume exclusion more important.

3.2.3. Alteration of colloid surface properties due to adsorption of dissolved organic macromolecules.

Adsorption of dissolved macromolecules on colloidal surfaces can disturb electric double layer interactions and alter van der Waals forces among colloids and between colloids and membranes, as well as cause steric hindrance effects. A number of studies on colloidal transport in porous media have shown that NOM can play an important role in facilitating the transport of natural and model colloids [118-120] and their aggregation kinetics [121]. Additionally, interactions between

the organic foulant and the membrane surface can modify membrane surface properties, including membrane surface roughness, hydrophobicity and charge, and has been shown to affect flux behavior [24, 27, 122, 123]. These changes can significantly modify the fouling behavior of colloidal particles by either increasing or decreasing (depending on the molecular characteristics of the organic foulant) colloidal aggregation in the CP layer and their deposition on the membrane surface.

3.3. Materials and Methods

3.3.1. NF membrane.

A low-salt-rejection thin-film composite nanofiltration membrane (NF 270 by Dow-FilmTec, Minneapolis, MN) was used in all filtration experiments. Precut membrane samples were stored in de-ionized water at 4 ºC. The storage water was replaced weekly. The hydraulic resistance of the NF 270 membrane, determined from clean water flux measurements, was 1.98 (± 0.09) $\times$ 10^{13} m^{-1} at 20 ± 0.3 ºC. Observed salt rejection with 10 mM NaCl ranged from 40.2% – 58.8% at 20 ± 0.3 ºC, consistent with the manufacturer's specified salt rejection of 40-60%. Membrane surface zeta potential was characterized using a streaming potential analyzer (Zeta CAD, CAD Instrumentation, Les Essarts le Roi, France). Measurements were performed under the various solution conditions used in the filtration experiments. Before each measurement, the membrane coupons were soaked in 10 mM NaCl (the

background electrolyte solution used in filtration experiments) for 24 hr at 4 ºC. Membranes were then allowed to equilibrate with the test solution for 30 min before the measurement was started.

3.3.2. Model foulants.

Commercial colloidal silica, Snowtex-XL (ST-XL, Nissan Chemical America Corp., Houston, TX) was used as the model colloidal foulant. Manufacturer supplied data specified that particle size ranged from 40 to 60nm.

Humic substances, proteins and polysaccharides have been identified as the major organic foulants in water and wastewater [124-129] For this reason, four organic compounds were used in this study: Suwannee River humic acid (HA), dextran, sodium alginate, and bovine serum albumin (BSA). In addition to the other commonly studied organic foulants, dextran was chosen because it is known to have minimum interaction with most surfaces and can serve as a good model for "non-interacting" macromolecules.

HA (standard II) was obtained from International Humic Substances Society (St. Paul, MN) and was not purified any further. Dextran from *Leuconostoc mesenteroides*, sodium alginate derived from brown algae, and BSA were purchased from Sigma-Aldrich (St. Louis, MO). The molecular weights reported by the manufacturers are 1 – 5, 9 – 11, 10 – 60, and ~ 66 kDa for humic acid, dextran, sodium alginate, and BSA, respectively. All stock solutions and feed waters were

prepared using ultrapure water produced by a Millipore system (RiOS System, Billerica, MA). Because HA has low solubility under acidic conditions, pH was raised to 8.2 with NaOH and the solution was filtered using a vacuum filter (Whatman Grade No. 1 filter paper, England) and stored in an amber glass bottle. The concentration of the stock solution was then verified by total organic carbon (TOC) measurements with a TOC analyzer (Shimadzu Scientific Instruments, Japan). All stock solutions were stored in the dark at 4°C.

Surface zeta potential and hydrodynamic diameter of the model foulants were characterized by electrophoretic mobility and dynamic light scattering (DLS) measurements using a Zetasizer Nano ZS (Malvern Instruments, Westborough, MA).

3.3.3. Measurement of organic foulant adsorption on silica.

Adsorption of organic foulants on the silica colloidal particle surface determines their impact on colloid-colloid and colloid-membrane interactions. Adsorption of the model organic foulants on a silica surface was investigated using a quartz crystal microbalance with dissipation monitoring (QCM-D) technique (Q-Sense E4, Q-Sense, Glen Burnie, MD). Principles and applications of the QCM-D technique can be found elsewhere [130].

Silica-coated quartz crystals (QSX303, Q-Sense, Glen Burnie, MD) were used to simulate the surface of the model silica colloidal foulant. QCM-D measurements employed the same background solution (10 mM NaCl) and organic concentration

(20 mg/L) used in the cross-flow filtration experiments. Before each experiment, the crystal sensors and the flow modules were cleaned with 2% sodium dodecyl sulfate (SDS) solution followed by de-ionized water and dried with ultrapure N_2 gas. The crystals were further cleaned in a UV/Ozone ProCleaner (BioForce Nanosciences, Ames, IA) for 20 min. In each experiment, fundamental frequencies of each crystal were first verified under dry air conditions. Then, a baseline was established by running the background solution (10 mM NaCl) for 10 min. This was followed by the adsorption phase using the organic foulant solution. After adsorption equilibrium was established, the influent was switched to the buffer solution again to remove the residual foulant solution in the cell channel.

3.3.4. Membrane filtration experiments.

Nanofiltration experiments were carried out in a laboratory scale cross-flow membrane filtration system consisting of two membrane-cells in parallel [131]. A pulsation dampener (Model H1020V, Blacoh Fluid Control, Inc, Riverside, CA) situated at the outlet of the hydra-cell pump was charged at 80% operating pressure to dampen pressure irregularities. Feed water temperature was kept constant at 20ºC using a re-circulating water chiller (VWR, West Chester, PA).

Filtration experiments included three main phases: membrane compaction, conditioning, and fouling. The membranes were first compacted at 100 psi (689.5 kPa), a pressure higher than the designed experimental pressure, using ultrapure

water for a minimum of 5 hours to obtain a stable clean water flux. During the conditioning phase, background electrolyte solution, i.e. 10 mM NaCl was filtered through the membranes for at least 9 hours. Pressure was adjusted to yield a stable permeate flux of 2 x 10^{-5} m/s in all experiments, corresponding to an applied pressure range of 65 -70 psi (448 – 483 kPa). This ensured the same initial permeate flux for the fouling stage of all experiments. Conductivity of both permeate and feed waters was monitored during the conditioning phase to check membrane integrity and establish initial observed salt rejection. After a stable permeate flux of $2x10^{-5}$ m/s and appropriate salt rejection had been achieved, the fouling phase was started by addition of the corresponding foulant or foulants. The pump was stopped while the foulant was introduced to the feed tank and allowed to mix thoroughly for 5 min before pumping was resumed. A sample was taken from the feed reservoir immediately before filtration was resumed for confirmation of foulant concentration. Concentrations of colloidal and organic foulants used were 100 mg/L and 20 mg/L, respectively, in both individual fouling and combined fouling experiments. Pressure, permeate flux, and feed water temperature were continuously monitored during the experiments. Samples were taken from both the feed and permeate at predetermined times during both the conditioning and fouling stages for analysis of pH, conductivity (Oakton pH/CON 510 Benchtop Meter, Oakton Instruments, Vernon Hills, IL) and foulant concentrations. Concentrations of organic foulants were determined by TOC measurements. Colloidal foulant concentrations in the feed were determined by turbidity measurements using a

turbidity meter (Hach Company, Loveless, CO). The cross-flow system was thoroughly cleaned after each experiment with 6 L of 5 mM NaOH re-circulated for 1 hr followed by three rinses with 6 L of de-ionized water for at least 1 hr each. All experiments were repeated at least twice.

3.4. Results and Discussion

3.4.1. Characteristics of model foulants.

The model foulants were characterized for their size and surface zeta potential under the solution conditions used in the filtration experiments. Table 3.1 summarizes the results of the characterization. The mean hydrodynamic diameter was derived from an average number-based-distribution based on at least 5 measurements. BSA has a negative surface zeta potential of -20.7 ± 0.9 mV under the experimental conditions used whereas that of dextran was close to neutral at -7.2 ± 1.5 mV. Alginate and HA had a much more negative zeta potential, measuring -45.0 ± 1.2 and -37.9 ± 1.2 mV, respectively, under the same solution conditions.

The model inorganic foulant (ST-XL) measured 60.7 ± 1.2 nm in hydrodynamic diameter and had a high negative surface zeta potential (ζ = -37.9 ± 0.4 mV) under experimental conditions. These results agree with the manufacturer's specifications of size (between 40-60nm) and previously published zeta potential measurements [28]. The measured particle sizes of dextran, BSA and

sodium alginate were all one order of magnitude smaller than that of ST-XL indicating that they can penetrate the ST-XL colloidal cake layer during filtration. Particle size is not reported for HA because it's extremely small size (~1 nm) is beyond the detection range for DLS measurement.

3.4.2. Adsorption of organic foulants on silica surface.

QCM-D experiments were performed using silica-coated crystal sensors to investigate adsorption of the model organic foulants on the silica surface. Adsorption is indicated by changes in the vibration frequency of the piezoelectric quart-crystal sensor, and the amount of organic molecules adsorbed can be calculated from the frequency change using the Sauerbrey equation [132] (Equation 3.6) provided that the adsorbed layer is rigid (i.e., experiences low energy dissipation):

$$\Delta f = -\frac{2f_0^2}{A\sqrt{\rho_q \mu_q}} \Delta m \qquad\qquad \text{Equation 3.6}$$

where Δf is change in frequency (Hz), f_0 is the resonant frequency (Hz) of the crystal sensor, Δm is change in mass adsorbed (kg), A is the piezoelectrically active crystal area (m^2), ρ_q is the density of quartz (kg/m^3), and μ_q is the shear modulus of quartz (Pa).

Experiments using dextran, HA, and sodium alginate showed negligible change in the vibration frequency of the silica-coated crystal sensor, indicating no adsorption of these compounds on the silica surface. This is consistent with the very high negative zeta potentials of humic acid and alginate (Figure 3.3) and consequently strong electrostatic repulsion between these molecules and the negative silica surface.

Significant adsorption of BSA on silica surface was observed. Figure 3.2 presents the areal mass of BSA adsorbed as well as the thickness of the adsorbed layer, calculated from the Sauerbrey equation. A comparison of the Sauerbrey model fit to that by a visco-elastic model [130] indicates that a rigid layer is adsorbed and that the Sauerbrey equation is valid. The calculated thickness of the adsorbed layer indicates a monolayer of BSA adsorbed on the surface of the silica coated crystal, suggesting that the presence of BSA may change the surface properties of the silica colloids and hence their interactions with the membrane and other silica colloids.

3.4.3. Impact of the organic foulants on the physicochemical properties of silica colloids.

Adsorption of dissolved organic compounds on the surface of ST-XL may alter its surface properties, e.g., zeta potential and particle size, and consequently impact the interactions among ST-XL colloids. Surface zeta potential and

hydrodynamic diameter of ST-XL were measured in the presence and absence of the model organic foulants, and the influence of the model organics under relevant solution conditions is demonstrated in Figure 3.3 and Figure 3.4.

It is worth noting that although electrophoretic mobility measurement using phase analysis light scattering provides an average zeta potential of all particles in a suspension, the size and concentration (1 or 20 mg/L) of dissolved organic compounds in the mixed suspensions were so small that the free organic molecules in the mixture had negligible impact on the zeta potential of the suspension. Zeta potential measurements of the organic foulants alone at these concentrations yielded non-detectable signals. The zeta potential and size of the organic foulants reported in Table 3.1 were achieved using much higher concentrations: at least 100 mg/L for HA and 1 g/L for dextran, alginate and BSA. Therefore, it is safe to consider that the measured zeta potential or mean particle size of the mixed suspensions represents that of the ST-XL with or without the model organic foulants adsorbed on the surface.

As shown in Figure 3.3, the zeta potential of the ST-XL was not affected by dextran or HA despite the zeta potentials of both dextran and HA being very different from that of the silica colloids. Meanwhile, no significant changes in particle size were observed in the presence of these two organic compounds (Figure 3.4), indicating no adsorption of HA dextran on the ST-XL colloidal surface. No significant change in zeta potential of particle size of the ST-XL colloids is again observed in the presence of alginate. This is consistent with the QCM-D

measurements that showed no adsorption of these compounds on silica-coated quartz crystal sensors.

In the presence of the model protein BSA, however, the magnitude of the zeta potential of the silica colloids decreased notably and the reduction increased with increasing BSA concentration (Figure 3.3). In addition, a careful examination of the particle size of ST-XL suggests the presence of an adsorbed BSA layer under these conditions (Figure 3.4). In the presence of 20 mg/L of BSA, the diameter of ST-XL increased by approximately 7 nm. The reduced zeta potential and increase particle size are consistent with the adsorption of a monolayer BSA on the silica surface observed in the QCM-D experiments. Data in Figure 3.3 and Figure 3.4 also indicate that surface coverage of BSA increases with BSA concentration.

3.4.4. Impact of the organic foulants on membrane surface zeta potential.

The zeta potential of the NF 270 membrane in 10mM NaCl solution at pH = 5.0 is -23.6 ± 1.5 mV. Membrane surface zeta potential measurements in the presence of each model foulant were performed immediately after those without organic foulants using the same membrane coupon. Figure 3.5 illustrates the effect of the four model organic foulants on the membrane surface zeta potential. Changes in membrane surface zeta potential upon exposure to the organic foulants are presented. Negative values indicate reduction in the negative zeta potential, while positive values represent increases.

All model organic foulants except dextran caused notable changes in membrane surface zeta potential, indicating significant adsorption of BSA, alginate and HA on the membrane surface. While adsorption of the highly negatively charged HA and alginate led to an increase in the magnitude of the negative membrane surface zeta potential, BSA significantly reduced its magnitude due to its lower charge density. These changes suggest that HA and alginate will increase the electrostatic repulsion between the membrane and the ST-XL colloids, while BSA will have an opposite effect.

3.4.5. Cross-flow filtration results.

Fouling experiments were performed with feed waters containing ST-XL alone, an organic foulant alone and both the ST-XL and an organic foulant. Concentrations of ST-XL and the organic foulants were 100 mg/L and 20 mg/L, respectively, in all experiments. Figure 3.6 shows the membrane flux decline results of all four sets of experiments, each with a different model organic foulant.

In order to examine the three proposed combined fouling mechanisms, the combined fouling layer resistance was compared to that predicted from the individual foulant resistance using a resistance in series model. The predicted value, calculated by summing the resistances of the individual colloidal and organic fouling layer, is referred as "the sum" in the discussion hereafter.

The resistance of the fouling layer was calculated using a rearrangement of Darcy's Law (Equation 3.1), where the trans-membrane osmotic pressure ($\Delta\pi_m$) was calculated following a previously published method [44, 45]. Rearranging the film-theory equation produces the following expression [44],

$$\Delta\pi_m = f_{os}\left(C_m - C_p\right) = f_{os}C_b R_o \exp\left(\frac{v}{k}\right)$$ Equation 3.7

which relates the trans-membrane osmotic pressure to the bulk molar salt concentration (C_b), the observed salt rejection ($R_o = 1 - C_p/C_b$), and the mass-transfer coefficient (k) through the osmotic coefficient f_{os} [133]. Since low salt concentrations were used in this study, van't Hoff's equation was used to determine f_{os} [45].

As the experiments were performed under laminar conditions, the initial mass-transfer coefficient, k_0, was calculated during the conditioning phase using Equation 3.8:

$$k_0 = 0.808\left(\frac{6QD_\infty^2}{WH^2L}\right)^{1/3}$$ Equation 3.8

Here, D_∞ is the bulk diffusion coefficient of the solute, Q is the volumetric feed flow rate, W is the channel width, H is the channel height, and L is the channel length. Plugging values of the initial permeate flux v_0, k_0 and the observed salt

rejection R_o during the conditioning stage into the second half of Equation 3.7 allows calculation of the intrinsic salt rejection R_i ($R_i = 1 - C_p/C_m$). $\Delta\pi_m$ during the fouling experiment was then calculated using the first half of Equation 3.7 from the measured C_p assuming a constant R_i.

Observed salt rejection during colloidal fouling alone decreased slightly from 55.0 to 52.1% (Figure 3.8), which agrees well with the modeling results of calculated CECP for the NF270 membrane [44, 45]. These results show that silica colloid cake-enhanced concentration polarization has negligible contribution to the flux decline of the NF270 membrane due to its low salt rejection. Therefore, contrary to other studies [28], CECP as a combined fouling mechanism will not be discussed here.

Figure 3.7 compares the calculated cake/gel layer resistances for each set of fouling experiments. The resistances are plotted as a function of cumulative permeate volume. This normalizes the plots, as the amount of colloidal or organic foulant transported to the membrane surface at a given permeate volume during the combined fouling experiment should be the same as that during colloidal fouling or organic fouling experiment if there are no organic-silica interactions.

The flux decline rates during the initial stage of fouling for all experiments are summarized in Table 3.2. Salt rejections during selected experiments are presented in Figure 3.8. The effect of each organic foulant is discussed below.

3.4.5.1. Combined fouling with dextran.

Figure 3.6a compares the membrane flux during filtration of the dextran solution, the ST-XL suspension and the mixture of dextran and ST-XL. The corresponding fouling layer resistances for these experiments are plotted in Figure 3.7a.

Dextran alone did not foul the membrane, as evidenced by the stable membrane flux throughout the organic fouling experiment. The ST-XL colloids caused significant decline of the membrane flux. Up until the latter stages of fouling, combined fouling with dextran creates a similar fouling layer resistance as that with silica alone. Towards the end of the experiment, however, the combined cake layer resistance begins to rapidly increase compared to the sum term, indicating a synergistic effect. Since dextran does not adsorb on ST-XL, the observed synergy indicates that both hindered back diffusion and a change in cake layer structure are present. Because this change in resistance is seen in the latter stages of fouling after significant accumulation of foulants has occurred, it is likely that the increase in resistance is caused by a change in cake layer structure as dextran fills in the interstitial pore space of the cake layer and that hindered back diffusion remains a small but contributive effect during combined fouling with dextran.

3.4.5.2. Combined fouling with HA.

As shown in Figure 3.6b, fouling by HA alone caused only slight flux decline. The combined fouling experiment with HA and ST-XL showed no synergistic effect in the beginning stage. In fact, a closer look at the initial flux decline rates (Table 3.2) during filtration of the ST-XL suspension and the mixture of HA and ST-XL (0.77 and 0.39 L^{-1}, respectively) shows that the presence of HA reduced the initial flux decline rate. This is attributed to HA adsorption onto the membrane surface, which increases the electrostatic repulsion between the foulants and the membrane. In the latter fouling stages, however, the membrane flux during combined fouling deviated from the calculated sum and showed a synergistic effect that continued to increase with filtration time. As HA does not adsorb to ST-XL, this increase is either due to the hindered back diffusion effect or to the increased resistance caused by a mixed fouling layer with HA interspersed in the ST-XL cake layer.

3.4.5.3. Combined fouling with sodium alginate.

Initial flux decline in the presence of sodium alginate alone was the most substantial of all the organic foulants (Figure 3.6c). The alginate fouling layer also displayed active salt rejecting characteristics, as evidenced by the steady increase in observed salt rejection over the length of the experiment (Figure 3.8). Strong

synergism was observed during the filtration of the ST-XL-alginate mixture (Figure 3.7c). The fouling layer resistance calculated during combined fouling is significantly higher than the calculated sum of individual fouling layers in spite of the slightly reduced initial fouling rate (Table 3.2, 0.77 vs. 0.44 L^{-1}) caused by the increased repulsion between ST-XL and the membrane. Salt rejection during the combined fouling experiment remained stable over time, indicating either the impact of CECP and salt rejection by the fouling layer were negligible, or the two effects cancelled each other out. The same combined fouling mechanisms for HA (hindered back diffusion and cake layer structure) are expected to apply to alginate. However, the synergistic effect caused by sodium alginate is greater in the initial stages of filtration compared to that by HA. It is postulated that this is due to a more significant effect of the hindered back diffusion mechanism. Since sodium alginate solution is much more viscous than the other model foulants, the back diffusion of the ST-XL colloids in the CP layer may be more severely hindered, causing faster accumulation of ST-XL and therefore a greater flux decline rate.

3.4.5.4. Combined fouling with BSA.

Flux decline in the presence of BSA alone appears to be caused by a compressible fouling layer that increases in resistance over time (Figure 3.6d). The mixture of BSA and ST-XL caused much greater flux decline than the sum of the contribution from each foulant (Figure 3.7d). The greater initial flux decline rate

can be explained by the faster deposition of ST-XL due to the reduced electrostatic repulsion between ST-XL and the membrane as well as that between ST-XL colloids, a result of the lower negative surface zeta potential upon adsorption of BSA (Figure 3.3 and Figure 3.5). Analysis of the feed water showed an increase, instead of the expected decrease, in turbidity with filtration time, resulting from the formation of ST-XL aggregates (Figure 3.9). Storage of the same feed solution over time did not show similar increase in particle size, indicating that these aggregates likely formed in the CP or fouling layer. This observation suggests that the cake layer formed was dynamic and some ST-XL aggregates were washed off from the membrane surface during cross-flow filtration. This is consistent with the large fluctuation of salt rejection observed during the combined fouling experiment (Figure 3.8). While it is unclear if the decrease in salt rejection is due to CECP or a disturbance in the fouling layer, calculations show that the increase in trans-membrane osmotic pressure over the course of the experiment has a negligible contribution to flux decline.

The synergism during the combined fouling experiment continued throughout the experiment. Because BSA adsorbs on silica surfaces, the observed synergism results from the interplay of all the three combined fouling mechanisms discussed in the Theory. In addition, the observed aggregation of foulants in the cake layer as well as the change in the growth rate of the combined fouling layer resistance at permeate volume of about 2.5 L (Figure 3.7d) suggests a shift in the combined fouling layer structure towards the latter stages of filtration. These

results with BSA show that the effects of organic foulant adsorption on silica surface are complex and can have important implications on membrane flux decline.

3.5. Conclusions

The flux decline behavior of a nanofiltration membrane in the presence of four model organic macromolecules and one model silica colloidal foulant was investigated to examine mechanisms responsible for the synergism observed in combined fouling. All model organic foulants tested exhibited a synergistic effect when in combination with the model silica colloids. The extent of the synergy, however, strongly depends on the molecular characteristics of the organic foulant. The three hypothesized mechanisms: increased resistance of the mixed fouling layer, hindered back diffusion, and organic foulant adsorption were shown to have varying effects on combined fouling, depending on the specific organic foulant. The greatest synergism was observed in the presence of an interacting organic foulant, BSA, which can adsorb onto silica colloids as well as the membrane surface to reduce repulsive interaction between foulants and the membrane as well as that among foulants. Adsorption of the organic foulant to the clean membrane surface only impacts the very beginning fouling stage and does not have a lasting effect on the overall flux decline behavior. The study also showed that the interplay of the various mechanisms in combined fouling can be very complex, calling for further

investigation of the combined fouling process. More comprehensive models that incorporate the combined fouling mechanisms suggested here are needed to properly predict the fouling of complex solutions.

Table 3.1 - Characteristics of model foulants. Reported values are the average of five measurements with standard deviation. The solution condition used was 10 mM NaCl and pH 5.9 ± 0.3.

Model foulant	Zeta potential (mV)	Diameter (nm)
Dextran	−7.2 ± 1.5	4.3 ± 0.2
BSA	−20.7 ± 0.9	6.9 ± 0.2
Humic acid	−37.9 ± 1.2	n/a
Sodium alginate	−45.0 ± 1.2	5.12 ± 2.2
Silica (ST-XL)	−37.9 ± 0.4	60.7 ± 1.2

Table 3.2 - Initial flux decline rates of all fouling experiments.

Foulant(s)	Initial flux decline rate[a] (L^{-1})
ST-XL	0.77
Dextran	0.02
Dextran + ST-XL	0.81
Humic acid	0.04
Humic acid + ST-XL	0.39
Sodium alginate	0.25
Alginate + ST-XL	0.44
BSA	0.16
BSA + ST-XL	1.07

[a] The initial flux decline rate is calculated by fitting data collected during the first 100 min by a linear function assuming $J//J_o = 1$.

Figure 3.1 - Schematic description of the cake/gel and CP layers of colloids and macromolecules after cake/gel layer formation. C_s: concentration at the membrane surface; C_b: bulk concentration; D: back diffusion coefficient. Subscript: c = colloids, m = macromolecules.
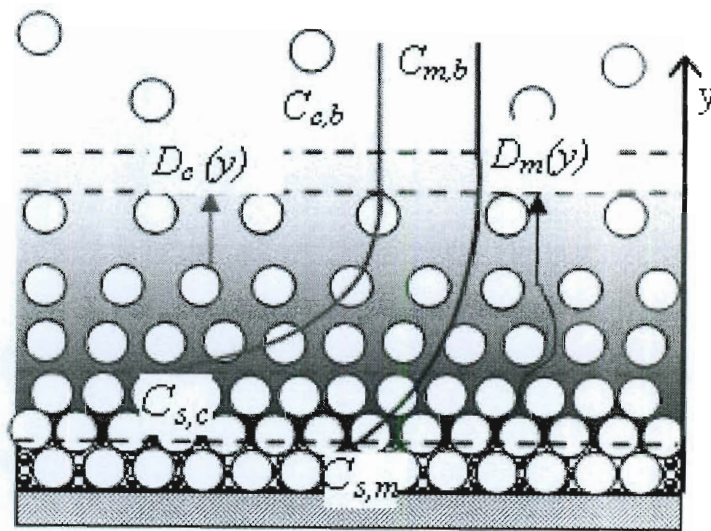
Figure 3.2 - Areal mass and thickness of the adsorbed BSA layer on the silica surface.

Phase 1: 10 mM NaCl; phase 2: 20 mg/L BSA in 10 mM NaCl; phase 3: 10 mM NaCl.
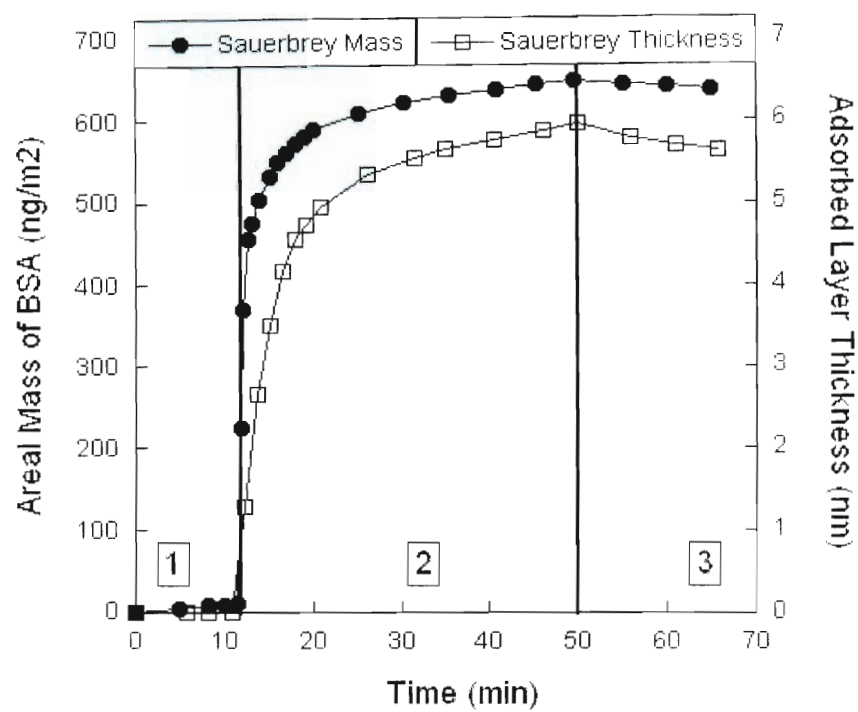
Figure 3.3 - Surface zeta potential of ST-XL in the presence of varying concentrations

of model organic foulants. Horizontal black line with striped halo represents the

average and standard deviation of ST-XL surface zeta potential in the absence of

model organic foulants. All test solutions contained 10 mM NaCl and the pH was

5.9 ± 0.3.
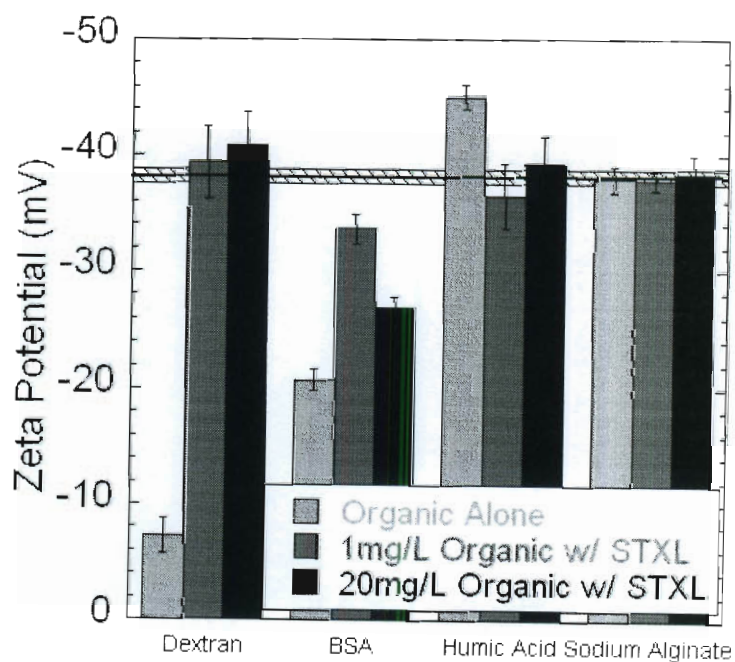
Figure 3.4 - Particle size of ST-XL in the presence of varying concentrations of model organic foulants. Black line with striped halo represents the average and standard deviation of the measured particle size of ST-XL in the absence of model organic foulants. All test solutions contained 10 mM NaCl, and the pH was 5.9 ± 0.3.
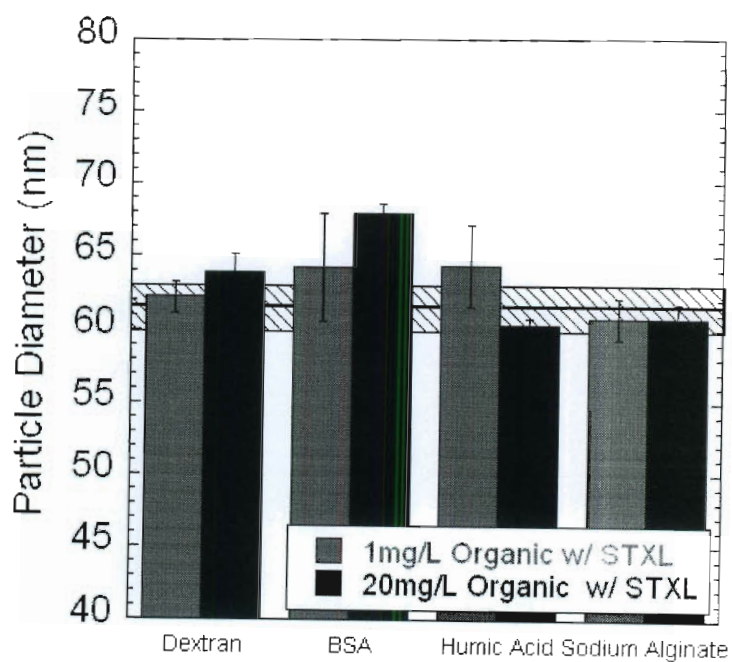
Figure 3.5 - Effect of organic foulants on membrane surface zeta potential (10 mM NaCl, pH 5.2 ± 5.5). Values represent the change from the original membrane zeta potential of −23.6 ± 1.5 mV.
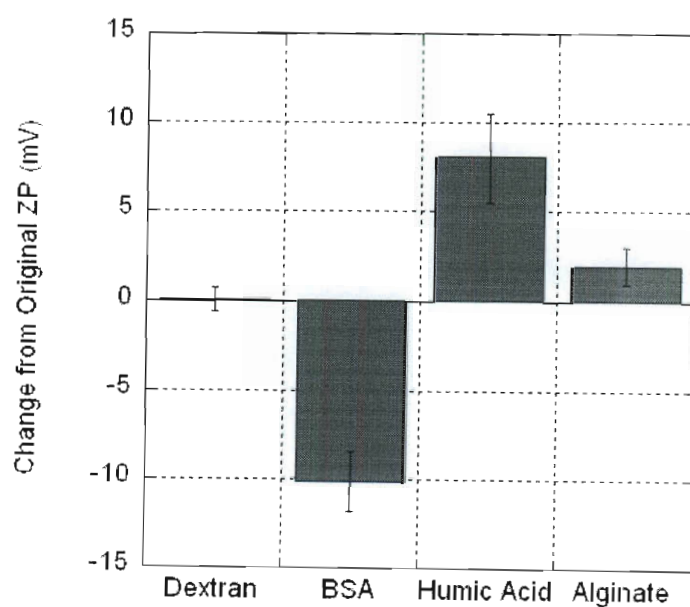
Figure 3.6 - Normalized flux of the individual organic and colloidal fouling and the combined fouling experiments for, (a) dextran; (b) humic acid; (c) sodium alginate; and (d) BSA.
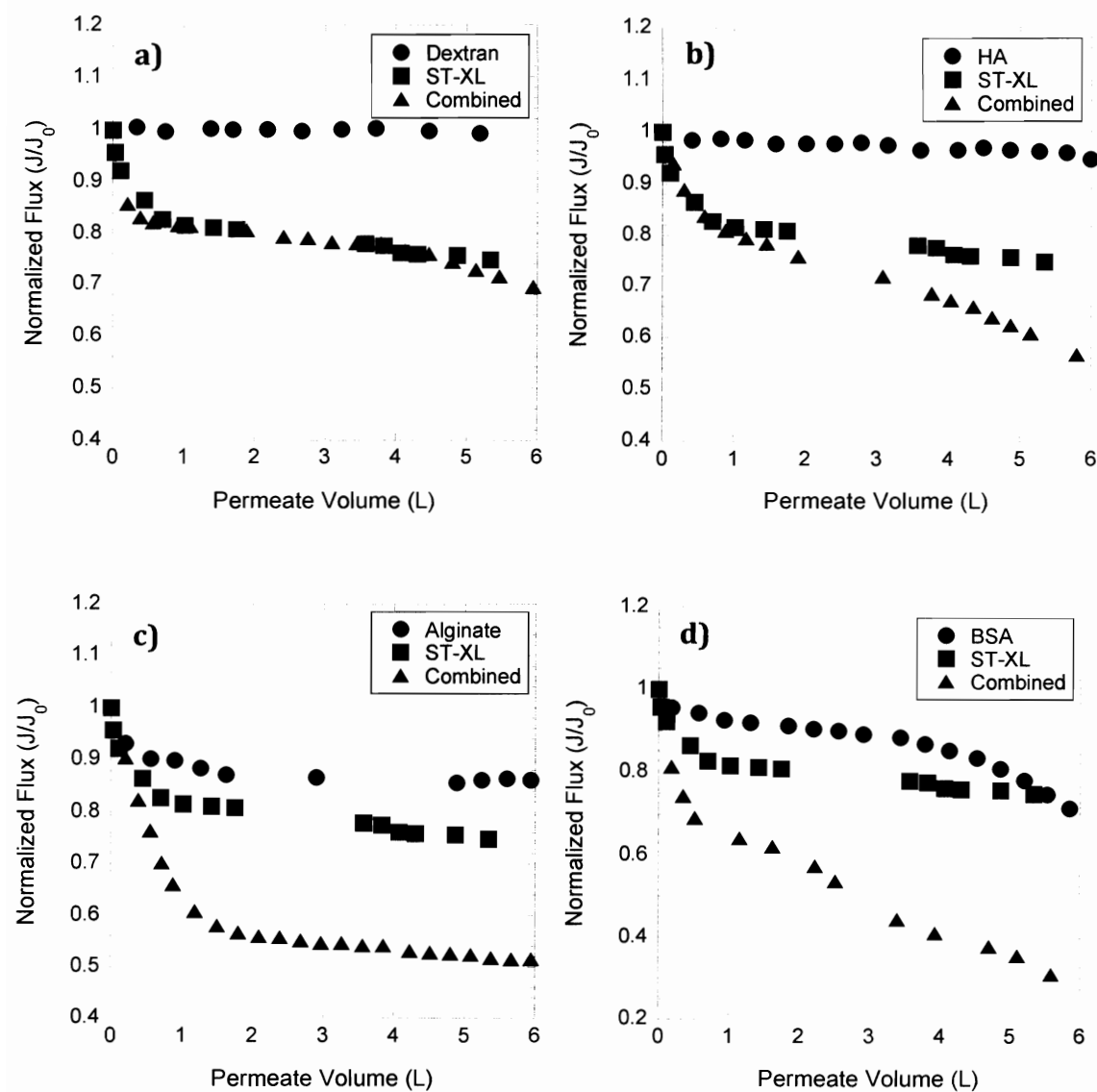
Figure 3.7 - Calculated cake/gel layer resistances (R_c) of each fouling experiment compared to the sum of individual foulant contribution for (a) dextran; (b) humic acid; (c) sodium alginate; and (d) BSA.
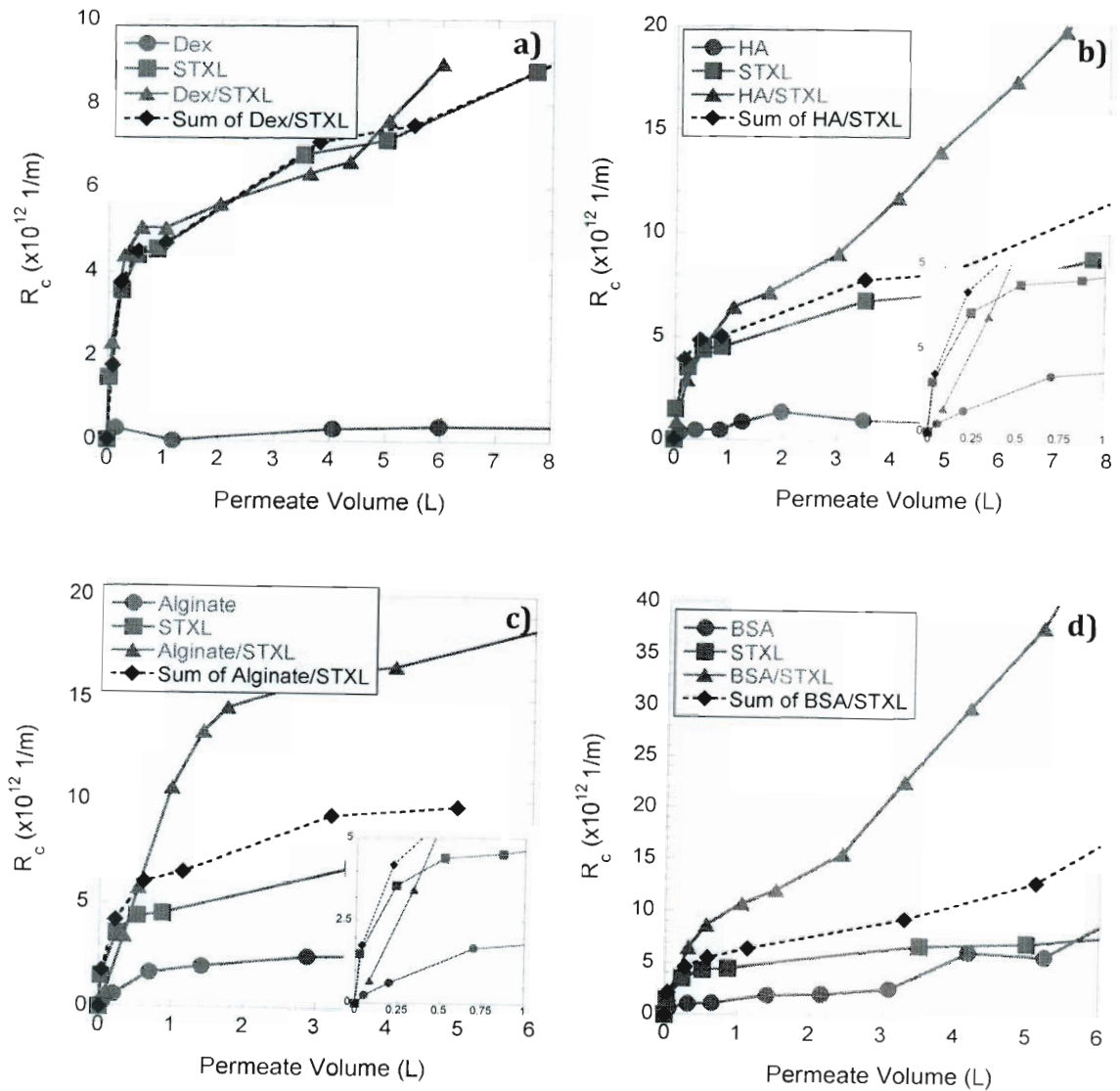
Figure 3.8 - Salt rejections observed during selected filtration experiments.
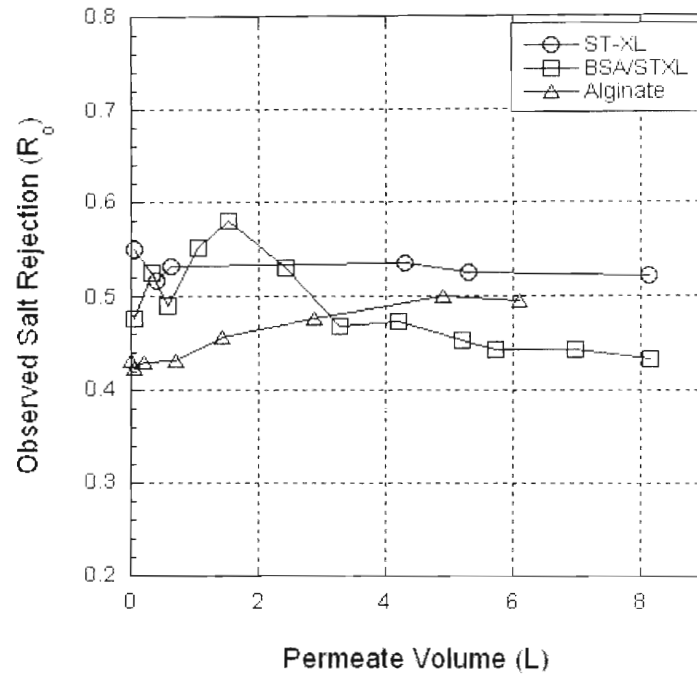
Figure 3.9 - Feed solution turbidity measurements of selected filtration experiments.
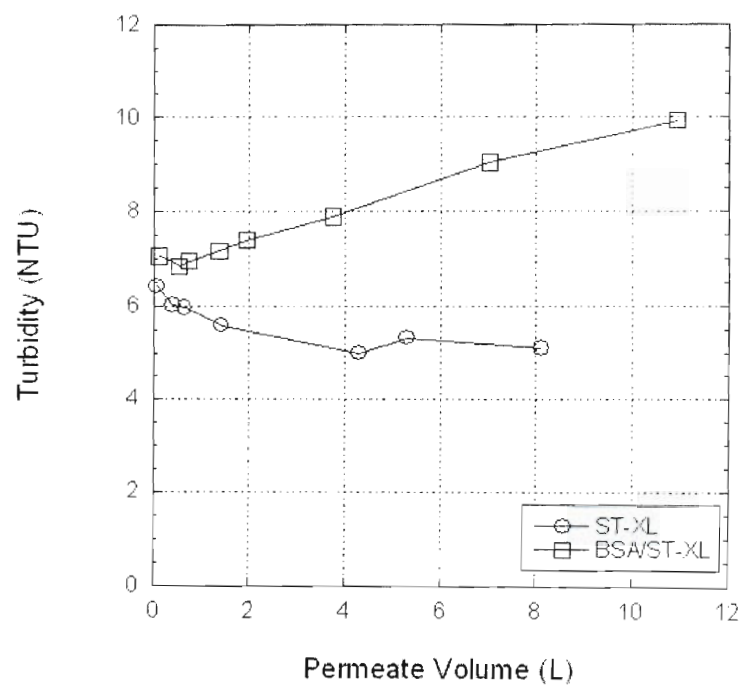
Chapter 4

Comparing Structure and Resistance of Combined Organic and Colloidal Fouling Layers Formed During Nanofiltration and Reverse Osmosis[2]

4.1. Introduction

Membrane fouling is an inherent obstacle to the advancement and widespread use of membrane technologies in water and wastewater treatment. Prediction of membrane fouling is complicated by the multiple types of foulants present in water and waste-water, including colloids, dissolved organic matter, mineral precipitates, and bio-foulants [29, 134, 135]. Each foulant contributes to

_____

[2] Manuscript in preparation for submission to *Water Research*.

the overall membrane flux decline through a variety of mechanisms. Most previous mechanistic studies on membrane fouling focused only on a single, well characterized foulant of homogenous physicochemical properties (referred to in this paper as singlet fouling) [1, 2]. One marked limitation in applying the theoretical and experimental results obtained from these studies to water and wastewater filtration systems is that fouling in these systems is almost always caused by more than one type of foulant, each with various particle/molecular sizes and surface characteristics.

One difficulty that arises when considering filtration of a solution containing foulants of different particle sizes and/or surface characteristics (referred to in this paper as combined fouling) is understanding if and how these differences affect foulant-foulant interactions and fouling layer formation. A limited number of studies on combined fouling by both inorganic colloids and dissolved organic matter have shown that fouling behavior differs under varying solution conditions and with different membrane types [28, 46, 136]. Although all studies observed that combined fouling cannot be predicted from fouling by individual foulants alone, fouling mechanisms specific to combined fouling have been identified to explain the complex behavior. Li *et al.* [46] performed combined fouling experiments with a low salt-rejection NF membrane in the presence of silica colloids and NOM. Flux decline measurements revealed significantly faster membrane fouling in combined fouling experiments than what might be predicted by summing the contributions from each foulant based on the individual fouling experiments. The aggravated

membrane fouling or enhanced flux decline (referred to in this paper as a *synergistic effect*) was attributed to the hindered back diffusion of each foulant. Hindered back diffusion, where two foulants indirectly affect each other to change the way they deposit onto the membrane surface by reducing effective diffusivity due to increased concentration and changes to solution viscosity, may be caused by other relatively small suspended foulants such as organics. Similar synergistic effects were reported by Contreras *et al.* using the same low salt rejecting NF membrane [136]. In another study performed on a high salt-rejection NF membrane, Lee *et al.* [28] found that flux decline during filtration of a mixture of NOM and silica colloids was initially enhanced compared to the sum of the flux declines caused by each foulant individually, but was reduced in the latter filtration stages. It was hypothesized that an "active salt rejecting layer" formed during combined fouling negated the effect of cake-enhanced osmotic pressure (CEOP), in which the colloidal cake layer increases the salt concentration in the concentration polarization layer and consequently the osmotic pressure at the membrane surface [44, 45]. Contreras *et al.* investigated the mechanisms of combined fouling using four different organic foulants: dextran, BSA, alginate and Suwannee River humic acid. It was found that both organic-colloid and organic-membrane interactions played important roles in combined fouling. The impact of these interactions on membrane flux strongly depended on the molecular properties of the dissolved organic foulant. For example, BSA adsorbs on SiO_2 particles and aggregation in the fouling layer; on the

other hand, dextran, alginate and humic acid indirectly contribute to synergistic flux decline due to hindered back diffusion [136].

Another important factor that determines membrane flux during combined fouling is the structure of the fouling layer [136]. The specific resistance of a fouling layer formed by polydispersed foulants strongly depends on its physical structure [137-139]. Several studies have shown that models assuming poly-dispersed suspensions form stratified layers or completely mixed layers results in different resistances and permeabilities, with layers foulants with small diameter expected to deposit first due to decreased drag and to form layer of higher resistance due to increased layer specific resistance [41, 43].

In all reported experimental studies on combined fouling, flux decline or fouling layer resistance during combined fouling was compared to that predicted from the simple additive sum of the flux decline or hydraulic resistance caused by individual foulants. Kim *et al.* illustrated that summing individual foulant resistance, i.e., the resistance in series model, implicitly assumes horizontally stratified layers of individual foulants in the fouling layer; summing flux decline due to each individual foulants, however, assumes resistance in parallel or a horizontally stratified structure i.e., different types of foulants exists in the fouling layer in a segregated manner and occupy different areas of the membrane surface. This study developed a mathematical model that determines the hydraulic resistance of a combined fouling layer assuming that colloidal and dissolved organic foulants are completely mixed in the fouling layer. Comparison between experimental

measurements and model calculations revealed that the combined fouling layer of BSA and SiO_2 colloids formed during dead-end filtration with no stirring actually had a resistance between those predicted for a completely mixed and a horizontally stratified fouling layer [138], suggesting that the actual structure of the combined fouling layer may be a combination of the two.

In this study, two ways of calculating combined fouling layer resistance based on individual foulants separately were compared to actual combined fouling layer resistance in order to elucidate fouling mechanisms unique to combined fouling: additive resistance and equivalent resistance. We use direct observation to determine the structure of combined fouling layers formed during filtration of complex suspensions and investigate the impact of foulant-foulant interaction on fouling layer structure, thickness and thus hydraulic resistance. We show that the combined fouling layer structure depends on salt rejection of the membrane, the particular dissolved organic foulant involved, and the type of foulant-foulant interactions present. Multiple combined fouling layer structures were identified that impacted layer resistance differently: completely mixed layers, aggregated layers, and stratified layer structure.

4.2. Methods

4.2.1. Membranes.

A nanofiltration membrane NF 270 (Dow-FilmTec, Minneapolis, MN) and a reverse osmosis membrane LFC 1 (Hydranautics, Nitto Denko, Oceanside, CA) were used in this study. Precut membrane samples were stored in de-ionized water at 4 °C. The storage water was replaced weekly. Both retentate and permeate water were continuously recycled back into the feed water and the crossflow velocity was 1 LPM (laminar range). The average hydraulic resistance and permeability of the NF 270 membrane, determined from clean water flux measurements, was 1.96 (± 0.09) $\times 10^{13}$ m^{-1} and 5.11 (± 0.26) x 10^{-11} m^{2}s/kg, respectively, at 20 ± 0.3 °C. Observed NaCl rejection at a feed concentration of 10 mM ranged from 40.2% - 58.8% at 20 ± 0.3 °C, consistent with the manufacturer's specified salt rejection of 40-60%. The average hydraulic resistance and permeability of the LFC 1 membrane under the same conditions was 1.19 (± 0.14) x 10^{14} m^{-1} and 8.54 (± 1.17) x 10^{-12} m^{2}s/kg. The LFC1 rejection of NaCl ranged from 96.6% - 98.2%, slightly lower than the manufacturer's specified salt rejection of 99.0%

4.2.2. Model foulants.

Humic substances, proteins and polysaccharides have been identified as the major organic foulants in water and wastewater [124-129]. In order to study the

different effect of each organic foulant type, four organic compounds from these classifications were used in this study: Suwannee River humic acid (SRHA), dextran (DEX), sodium alginate (ALG), and bovine serum albumin (BSA). Dextran, a neutral polysaccharide, was chosen because it is known to have minimum interaction with most surfaces and serves as a good model for "non-interacting" macromolecules.

SRHA (standard II) was obtained from International Humic Substances Society (St. Paul, MN) and used as received. Dextran from *Leuconostoc mesenteroides*, sodium alginate derived from brown algae, and BSA were purchased from Sigma-Aldrich (St. Louis, MO). The molecular weights reported by the manufacturers are $1 - 5$, $9 - 11$, $10 - 60$, and ~ 66 kDa for SRHA, dextran, sodium alginate, and BSA, respectively. All stock solutions and feed waters were prepared using ultrapure water produced by a Millipore system ($18.1 \, \Omega$ - RiOS System, Billerica, MA). SRHA stock solution was prepared by dissolving the SRHA powder at pH 8.2 (adjusted using 1 M NaOH) followed by vacuum filtration (Whatman Grade No. 1 filter paper, England). The concentrations of the stock solutions were determined by total organic carbon (TOC) measurements with a high sensitivity TOC analyzer (TOC-Vcsh, Shimadzu Scientific Instruments, Japan). All stock solutions were stored in the dark at 4°C.

Commercial colloidal silica, Snowtex-XL (ST-XL, Nissan Chemical America Corp., Houston, TX) was used as the model colloidal foulant. Manufacturer supplied data specified that the particle size ranged from 40 to 60 nm, which agreed with the measured particle size of 60.7 ± 1.2 nm.

Surface zeta potential and hydrodynamic diameter of the model foulants were characterized by electrophoretic mobility and dynamic light scattering (DLS) measurements using a Zetasizer Nano ZS (Malvern Instruments, Westborough, MA). Details of the characterization were reported elsewhere [136].

4.2.3. Membrane filtration experiments.

Membrane filtration experiments were carried out in a laboratory scale cross-flow filtration system consisting of two plate-and-frame membrane filtration cells in parallel [136]. Filtration experiments included three phases: membrane compaction, conditioning, and fouling. The membranes were first compacted at 100 psi for NF 270 membrane and 400 psi for the LFC 1 membrane, using ultrapure water for a minimum of 5 hours to obtain a stable clean water flux. During the conditioning phase, background electrolyte solution, was filtered through the membranes for at least 9 hours. Pressure was adjusted to yield a stable permeate flux of 2×10^{-5} m/s in all experiments, corresponding to an applied pressure range of 65 -70 psi and 380 – 420 psi for the NF 270 and LFC 1 membranes, respectively. This ensured the same initial permeate flux for the fouling stage of all experiments. Conductivity of both permeate and feed waters was monitored during the conditioning phase to check membrane integrity and establish initial observed salt rejection.

Fouling experiments were performed with feed waters containing ST-XL alone, an organic foulant alone and both the ST-XL and an organic foulant. Concentrations of ST-XL and the organic foulants were 100 mg/L and 20 mg/L, respectively, in all experiments. Two background electrolyte solutions of the same ionic strength were studied, 10 mM NaCl and 7 mM NaCl/1 mM $CaCl_2$). NF 270 experiments were performed in 10 mM NaCl only while LFC 1 experiments were performed under both solution conditions. Pressure, permeate flux, and feed water temperature were continuously monitored during the experiments. Samples were taken from both the feed and permeate lines at predetermined times during both the conditioning and fouling stages for analysis of pH, conductivity, and foulant concentration.

4.2.4. Autopsying membranes using Transmission Electron Microscopy (TEM).

At the end of each filtration experiment, fouled membranes were carefully removed from the filtration cells, stored in dark at 4 °C and kept moist in sealed containers until autopsy could take place. A resin embedding protocol was adapted [140] to prepare fouled membrane samples for TEM analysis. The skin layers of the fouled membrane samples were first carefully separated from the support layer using tweezers and were then dehydrated by soaking in a series of ethanol/DI water solutions (of 70%, 90%, 100%, 100% ethanol, each step for 15 min). Next, a series

of resin exchanges with a low viscosity resin (LR white resin, SPI Supplies, West Chester, PA) were used to insure full infiltration of both the fouled layer and the membrane. Samples were then sealed from air using flat embedding molds (Ted Pella, Inc., Redding, CA) and heated in an oven at 60°C for 3 days to dry. This dehydration protocol may decrease the overall dimensions of the sample slightly (up to 10%), which is well within an acceptable amount given the large degree foulant layer thickness can vary from sample location to location [141].

Thin sections (120 nm) of the resin embedded samples were cut first using an Leica ultramicrotome followed by a Leica diamond knife and then transferred onto formvar/carbon coated copper TEM grids (Ted Pella, Inc. Redding, CA). No staining was necessary to image the fouling layer. TEM images were obtained for both virgin and fouled membranes with a JEOL 1230 transmission electron microscope (TEM) (tungsten filament) at an acceleration voltage of 80 kV (JEOL USA, Peabody, MA).

4.2.5. Calculation of combined fouling layer resistance.

During filtration of foulant-free water, the resistance of the clean membrane ($R_m - m^{-1}$) can be calculated using Darcy's law with the knowledge of experimentally measured permeate flux ($v - m/s$), applied pressure ($\Delta P - Pa$), and solution viscosity ($\mu - N/m^2 s$).

$$v_{w_0} = \frac{\Delta P}{\mu(R_m)}$$
  Equation 4.1

When a foulant is present, the additional resistance caused due to accumulation of this foulant at the membrane surface can be included in terms of an effective decrease in pressure, such as an osmotic pressure difference that occurs as a result of concentration polarization when salt ions are present ($\Delta\pi_m$), or an additional resistance, such as the resistance caused by a fouling layer (R_f).

$$v = \frac{\Delta P - \Delta\pi_m}{\mu(R_m + R_f)}$$
  Equation 4.2

R_f is determined by the specific resistance of the fouling layer or the fouling layer mass per unit membrane area. For mono-dispersed, spherical colloids, the specific cake resistance can be estimated using the Carman-Kozeny equation,

$$\hat{R}_c = \frac{180\mu(1 - \varepsilon_c)}{\rho_p d_p^2 \varepsilon_c^3}$$
  Equation 4.3

Although several models have been proposed to predict and/or explain the filtration of complex solutions consisting of multiple foulant types, the calculation of fouling layer resistance must assume a certain fouling layer structures that may or may not represent the actual fouling layer structure. Determinations must be made on whether the fouling layer structure is completely mixed or completely stratified. Assuming a completely mixed fouling layer, Kim *et al.* [138] developed a model calculation of combined fouling layer specific resistance using a composite cell model approach based on volume fraction of the colloid (ϕ_c) and the organic (φ_g)

$$\hat{R}_{cg}(\phi_c, \varphi_g) = \frac{9\Omega_{KY}(\alpha, \beta)}{2b^2}$$ Equation 4.4

where Ω_{KY} is Happel's correction factor [36], α and β are factors corresponding to the permeability of the composite layer [138], and b is the diameter of the composite sphere.

4.2.6. Equivalent resistance calculation.

Previous studies on combined fouling (fouling with a combination of salt ions, organic macromolecules, and colloid particles) have calculated the flux decline due to multiple foulants via two different equivalent flux methods, a strong form and a weak form [138]. Originally proposed by Lee *et al.* and Li and Elimelech [28,

46], the strong form of the equivalent flux (v_{eq}^s) assumes that the flux decline of a combined solution(v_{com}) is equivalent to the sum of the flux declines of the individual components (where v_c – flux due to inorganic colloids alone and v_g is the flux due to organic alone). It is effectively an additive flux decline calculation:

$$v_{eq}^s = v_{w0} - (v_{w0} - v_c) - (v_{w0} - v_g) = v_c + v_g - v_{w0} \equiv v_{com} \qquad \text{Equation 4.5}$$

Normalized and in terms of membrane resistance, the same equation can be rearranged to be:

$$\frac{R'_m}{R_m + R'_{com}} \equiv \frac{R'_m}{R_m + R'_g} + \frac{R'_m}{R_m + R'_c} - 1 \qquad \text{Equation 4.6}$$

where R'_m is the resistance attributed to the membrane and the concentration polarization layer at the end of the conditioning phase (m^{-1}). R'_g and R'_c are the resistances due to organic and colloid accumulation at the membrane surface, respectively, and include the resistance due to osmotic pressure. This calculation assumes vertically stratified fouling layers of each foulant, and is essentially a resistance in parallel model.

4.2.7. Additive resistance calculation.

In this study, the additive resistance calculation, or weak form of the equivalent flux, is used to calculate the combined fouling layer resistance (R_{com}) during the experiment. The additive resistance calculation assumes that the total resistance (R_{com}) of a fouling layer consisting of organics and colloids can be calculated from additive contributions of each foulant:

$$R_{com} \equiv R_m + R_c + R_g \qquad\qquad \text{Equation 4.7}$$

where R_m, R_c, and R_g, are the resistances due to the membrane, colloid cake layer, and organic gel layer, respectively, in series. These resistances differ from R'_m, R'_g and R'_c in that they do not include the resistance due to osmotic pressure. Osmotic pressure contribution is calculated separately by rearranging the film-theory equation to produce the following expression [44],

$$\Delta\pi_m = f_{os}\left(C_m - C_p\right) = f_{os}C_b R_o \exp\left(\frac{v}{k}\right) \qquad\qquad \text{Equation 4.8}$$

which relates the trans-membrane osmotic pressure ($\Delta\pi_m$) to the bulk, membrane surface, and permeate molar salt concentrations (C_b, C_m, and C_p), the observed salt rejection ($R_o = 1 - C_p/C_b$), and the mass-transfer coefficient (k) through the osmotic coefficient f_{os} [133]. Salt concentrations are calculated based on feed and permeate

conductivity measurements. Since low salt concentrations were used in this study, van't Hoff's equation was used to determine f_{os} [45]. Details for calculating k can be found in our previous work [136].

This method includes the ability to examine the effect of cake enhanced osmotic pressure (CEOP) in $\Delta\pi_m$, when the presence of a cake layer increases concentration polarization of salt ions within the tortuous pores of the cake layer and increases the osmotic pressure at the membrane surface [45]. In our calculation, membrane intrinsic rejection was assumed constant for a given membrane. Therefore CEOP is assumed when the osmotic pressure differences ($\Delta\pi_m$) increases over the course of the experiment. Analyzing the change in osmotic pressure over the course of the experiment reveals insight into the fouling layer structure mechanisms contributing to the combined fouling flux decline.

4.3. Results and Discussion

4.3.1. Cross-flow filtration experimental results.

In order to examine combined fouling mechanisms, the measured combined fouling layer resistance (R_{com}) was compared to that predicted from individual fouling resistances using an equivalent resistance (ER) calculation and the additive resistance (AR) calculation at similar volume of permeate collected.

Normalized equivalent resistance of the fouling layers are presented in Figure 4.1 and Figure 4.2a, for NF 270 and LFC 1 membranes in 10 mM NaCl. LFC1 membrane in 7 mM NaCl and 1 mM $CaCl_2$ is also presented in Figure 4.2b. Normalized additive resistances of the fouling layer are presented in Figure 4.3 and Figure 4.4a for NF 270 and LFC 1 membranes in 10 mM NaCl, respectively, after 5 L of permeate was collected. Additionally, experiments performed on LFC 1 membrane in 7 mM NaCl and 1 mM $CaCl_2$ are shown in Figure 4.4b. Model silica colloids alone caused significant decline of the membrane flux (Figure 4.1 – 4.4). With ST-XL-only experiments with each membrane, increases in osmotic pressure are observed after 5L of permeate is filtered (Table 4.1). This increase is greater for the LFC1 membrane as salt rejection is also greater. Increase in osmotic pressure during filtration of colloids-only is known fouling mechanism called cake enhanced osmotic pressure (CEOP) or cake enhanced concentration polarization (CECP) [45] and is caused due to an increased salt concentration gradient within the pores of the colloid cake layer. This increase in osmotic pressure acts as an increase in resistance causing further flux decline in a similar manner as hindered back diffusion. Each combined fouling case will be examined in order to determine if osmotic pressure increases are greater or less than the colloid-only counterpart, revealing additional information about the combined fouling layer structure.

Resistances will be analyzed alongside TEM images of the layer itself to identify combined fouling mechanisms related to structure and to determine if the assumptions made during combined resistance calculation are valid. Combined

fouling layers are directly inspected through TEM images of autopsied membranes. For reference, virgin membranes NF270 and LFC1 are shown in Figure 4.5a and b, respectively. A ST-XL-only fouling layer (Figure 4.5c) and an organic layer of BSA-only (Figure 4.5d) formed on the NF270 membrane are also shown for comparison.

4.3.1.1. Combined fouling with dextran.

Dextran alone did not significantly foul either membrane, as evidenced by the low normalized fouling layer resistances presented in Figures 4.1 to 4.4. There appears to be little to no synergistic effect during the latter stages (after 5.0 L permeate collected) of combined fouling with dextran on the NF270 as compared to either the additive or equivalent resistance. The combined fouling layer formed on the LFC1 membrane has a higher resistance than either the calculated additive or equivalent resistance, indicating slight synergism. Because dextran and silica do not directly interact [136], the synergism observed cannot be due to modified silica properties that enhance deposition and membrane fouling.

TEM imaging of the combined fouling layer on the NF270 membrane shows a closely packed layer, similar in structure to the silica-alone fouling layer (Figure 4.6a). These layers appear to have dextran evenly mixed within the layer. No significant variation is seen between the additive and equivalent calculations because the individual resistance of dextran-alone is so small. The fouling layer created with the LFC1 membrane with and without the presence of $CaCl_2$ had

similar structures (Figure 4.6c and Figure 4.8a), with dextran evenly mixed, yet exhibited a greater synergistic effect. Because LFC1 is a more selective membrane, the effect of hindered back diffusion as well as the increased resistance due to a completely mixed layer both contributes to the slight synergistic flux decline.

After 5.0L of permeate during combined filtration with dextran and ST-XL there is slight increased osmotic pressure with the NF270 membrane (Table 4.1). Although there is significantly decreased osmotic pressure with the tighter LFC1 membrane under both salt conditions, the total increase in osmotic pressure is less than experiments performed with ST-XL alone. From the TEM images in Figure 4.7c and Figure 4.8a, interstitial dextran was observed. Analyzing the osmotic pressure change over the experiments in conjunction with the TEM images reveals that osmotic pressure decreases as the void space previously occupied by salt ions is replaced by dextran. For layers created on the LFC1 membrane, the presence of dextran within the layer makes the layer less permeable to convective flow and forms a "salt-rejecting layer," thus osmotic pressure decreases over time (Table 4.1).

4.3.1.2. Combined fouling with BSA.

During the filtration of the BSA solution with both membranes, the fouling layer appears to be compressible as the resistance remains steady in the beginning (after 0.5 L permeate collected) and then increases drastically in the later stages of fouling (after 5.0 L permeate collected) (Figure 4.3 and 4.4). BSA layer

compressibility is seen more clearly when considering the flux decline curves (for NF270 membrane, see [136]. Data for LFC1 membrane is similar but not shown). This is consistent with the study by Kim *et al.* which reported an increase in the volume fraction of the BSA gel layer formed during dead-end filtration [138]. Significant synergism is observed throughout the combined fouling of both membranes when compared to both the additive and the equivalent resistances, despite different salt rejections of the two membranes (Figures 4.2 to 4.4). In addition to the hindered foulant back diffusion, greater combined fouling resistance as compared with the calculated resistances during initial fouling is also attributed to the faster deposition of ST-XL, a result of the lower negative surface zeta potential of ST-XL and membrane upon adsorption of BSA [136]. For the LFC1 membrane in the presence of Ca^{2+}, the resistance created by the combined fouling layer is significantly greater than that created in NaCl alone (Figure 4.4).

Inspection of the BSA-ST-XL fouling layer shows a hybrid structure of unevenly spaced particles and organic, possibly the result of aggregation with the CP or fouling layer (Figure 4.6b, Figure 4.6d and Figure 4.8b). Analysis of the feed water over the course of these experiments showed an increase, instead of the expected decrease, in turbidity with filtration time, resulting from the formation of BSA-ST-XL aggregates. Storage of the same feed solution over time did not show similar increase in particle size, indicating that these aggregates likely formed in the CP or fouling layer above the membrane. Because BSA adsorbs on silica surfaces, the observed synergism results from the interplay of all the three combined fouling

mechanisms introduced earlier and further discussed in [136]. As permeate volume increases, the calculated combined resistance is likely higher due to increased gel volume concentration within the fouling layer. The results of combined fouling with BSA show that the effects of organic foulant adsorption on silica surface are complex and can have important implications on membrane flux decline. Additionally, the aggregated structure creates a much more resistant layer than is predicted by calculations based on the individual components.

On NF270 and LFC1 in the presence of NaCl-only, the osmotic pressure of combined fouling layers created with BSA remains constant, while it increases slightly for LFC1 with Ca^{2+} present (Table 4.1). These changes are still less than ST-XL-only experiments, indicating that the BSA/ST-XL aggregate structure does not promote CEOP as a pure colloid cake layer does in NaCl alone. In the presence of Ca^{2+}, BSA zeta potential decreases, increasing its likelihood to aggregate (Chapter 5, Table 5.2). These larger aggregates result in slight CEOP as salt is concentrated within the spaces, which are not present with smaller aggregates.

4.3.1.3. Combined fouling with humic acid.

Fouling layer resistance resulting from fouling due to SRHA-alone was very small for both membranes (Figure 4.1 to Figure 4.4). SRHA was previously shown to have contradicting effects on combined fouling depending on the salt rejection of the membrane used [28, 46]. The results presented here agree with the previously

published results and are consistent throughout the experiments: for the low salt-rejecting NF 270 membrane, a synergistic effect was observed during the combined fouling experiment; with the high salt-rejecting LFC 1 membrane, a reduced fouling effect was observed during combined fouling compared to what would be anticipated from the results of the individual components. In a study using a high salt rejection NF membrane, Lee *et al.* suggested enhanced colloidal stability in the presence of the NOM decreased colloid deposition and decreased the CEOP effect [28]. While our previous results show that ST-XL properties remain unchanged in the bulk concentration and at best slightly stabilized in the presence of Ca^{2+} (Appendix A), it is possible that at higher concentrations SRHA would enhance ST-XL stability, as would be seen at the membrane surface [136].

TEM imaging of the combined SRHA-ST-XL fouling layer shows a notable difference between the fouling layer structures on NF 270 and LFC 1 (Figure 4.7a vs. Figure 4.7c and Figure 4.8c). As humic acid does not adsorb to ST-XL [136], the synergism observed with the NF 270 membrane is attributed to the hindered back diffusion of the foulants as well as the greater specific resistance of a completely mixed fouling layer with humic acid interspersed in the ST-XL cake layer. Direct observation of the fouling layer during filtration with NF270 shows a thinner, well mixed layer (Figure 4.7a) as opposed to the thicker, stratified layers formed during filtration with LFC1 (Figure 4.7c and Figure 4.8c) where immediately adjacent to the membrane surface is a dense, dark layer of humic acid and much looser layer with both colloids and larger pockets of humic acid towards the feed side. The

completely mixed layer during low-salt rejection filtration exhibits more resistance than what would be expected by summing individual components, which is supported by literature which showed that foulant polydispersity increases resistance and thus specific resistance through the addition of smaller particles [41]. However, during high-salt rejection filtration, the stratified fouling layer formation produces a total resistance that is less than the sum of the individual components. Based on the osmotic pressure data, the dense layer at the surface seen in the images is salt rejecting, while the looser, predominately ST-XL layer has a lower specific resistance, so the combined total is still less than the either calculated resistance.

Similar to the dextran combined fouling cases, combined fouling for humic acid and ST-XL had no observable change in osmotic pressure using the NF270 membrane and decreased osmotic pressure using the LFC1 membrane (Table 4.1). With the LFC1 membrane, the combined fouling layer created at the membrane surface decreases osmotic pressure by becoming less permeable to salt ions than the membrane itself. This phenomena of an "active rejecting fouling layer" is consistent with an earlier study on combined fouling using high salt rejecting membranes [28].

4.3.1.4. Combined fouling with alginate.

Sodium alginate fouling resistance created on both membranes in the presence of NaCl-only was comparable to that of the resistance created by the other organic foulants. In the presence of Ca^{2+}, however, the alginate layer increases resistance greatly by forming a strong cross-linked gel layer which creates substantial resistance (Figure 4.5). Strong synergism was observed during the filtration of the ST-XL-alginate mixture in NaCl for both membranes as the fouling layer resistance calculated during combined fouling is significantly higher than the calculated sum of individual fouling layers (80% and 48% higher for NF270 and LFC1, respectively). However, although the absolute resistance of the layer in the presence of Ca^{2+} is much greater than all the other experiments, synergism is not observed during combined fouling in the presence of calcium (Figure 4.4).

TEM images of the alginate combined fouling layer formed on N270 and LFC1 in NaCl-only show a very dense, compact fouling layer of closely packed colloids (Figure 4.7b and Figure 4.7d). The alginate combined fouling layer formed on LFC1 in the presence of Ca^{2+} consists of ST-XL suspended within a gel-like alginate structure (Figure 4.8d). The same combined fouling mechanisms for SRHA (hindered back diffusion and cake layer structure) are expected to apply to alginate combined fouling based on individual and combined fouling characterization since alginate did not modify the ST-XL surface [136]. It is postulated the stronger synergism is due to a more significant effect of the hindered back diffusion mechanism. Since sodium alginate solution is much more viscous than the other

model foulants, the back diffusion of the silica colloids in the CP layer may be more severely hindered, causing faster accumulation of silica and therefore a greater flux decline rate. In the presence of Ca^{2+}, the additional resistance caused by the presence of ST-XL is cancelled out by the loss of resistance due to interrupting the cross-linking of a continuous alginate gel layer. Therefore, the calculated resistances overestimate the combined fouling layer resistance and a reduced fouling effect is observed.

Combined fouling for alginate and silica had no observable change in osmotic pressure using the NF270 membrane yet different osmotic pressure changes using the LFC1 membrane (Table 4.1). In the presence of only NaCl, the osmotic pressure decreased significantly whereas in the presence of $CaCl_2$ there was significant increase in osmotic pressure. The gelled structure of the alginate-ST-XL-Ca^{2+} fouling layer retains salt ions, increasing the resistance further, while the alginate-ST-XL layer in the presence of NaCl acts as an active rejecting layer. In the presence of Ca^{2+}, alginate particle size nearly doubles and when closely packed, larger pore spaces are present. Salt is able to penetrate this layer, since it is not fully cross-linked like the alginate-only layer in Ca^{2+}, and accumulate in the interstitial pore space and create CEOP.

4.4. Conclusions

Understanding the fouling behavior of complex suspensions and being able to predict fouling based on water characteristics is a formidable research challenge. Most previous studies on combined fouling of organic macromolecules and inorganic colloids have attempted to predict fouling behavior based on knowledge of individual foulant characteristics. In this study, the flux decline behavior of combined suspensions were investigated on a nanofiltration (NF 270) and a reverse osmosis (LFC 1) membrane in order to examine mechanisms responsible for the synergistic and reduced fouling phenomena previously observed in combined fouling. Combined fouling of four model organic macromolecules in combination with one model inorganic foulant was investigated. Actual combined fouling layer resistances formed in the presence of two foulants were compared to two calculated resistances based on individual foulant resistances: an additive resistance (resistances in series) and an equivalent resistance (or additive flux decline). The three hypothesized mechanisms: hindered back diffusion, organic foulant adsorption, and increased resistance of the mixed fouling layer due to interstitial presence of the organic were shown to have varying effects on combined fouling, The extent of the synergistic effects observed during combined fouling strongly depends on the molecular characteristics of the organic foulant and the structure of the fouling layer. Great synergism was observed in the presence of an interacting organic foulant, BSA, which adsorbed to silica colloidal as well as the membrane surface to reduce repulsive interaction between foulants and the membrane as well

as that among foulants. Its aggregate fouling layer structure also led to increased resistance beyond what is predicted by the individual components. Lack of synergism during filtration of SRHA and ST-XL with a high-salt rejecting membrane is related to differences in the cake layer structure and the presence of an active rejecting layer which minimizes the effect of CEOP, which is confirmed with direct imagine by TEM. In the presence of Ca^{2+}, alginate was also shown to form a gel layer of significant resistance but the additional presence of ST-XL during combined fouling acts to break up the cross-linked alginate layer to reduce fouling. Additionally, observing and calculating changes in osmotic pressure during the experiments reveal that combined fouling on high-salt rejecting membranes reduce the CEOP effect by forming a combined layer resistant to convective flow. TEM imaging of the layer directly helps to elucidate which mechanisms contribute to flux behavior regarding foulant positioning within the combined fouling layer.

Table 4.1 – Change in calculated osmotic pressure after 5.0 L of permeate is collected with for NF270 – 10mM NaCl, LFC1 – 10mM NaCl, and LFC1 – CaCl$_2$. Values are calculated from Equation 4.8 using conductivity measurements collected from the permeate and feed waters.

	Change in Osmotic Pressure (psi)		
	NF270	LFC1	
Foulant(s)	10 mM NaCl	10 mM NaCl	7 mM NaCl/1 mM CaCl$_2$
STXL	1.5	7.8	6.1
Dextran + STXL	0.6	-2.6	-7.8
BSA + STXL	0.6	-0.3	1.6
SRHA + STXL	0.0	-10.3	-7.8
ALG + STXL	-0.1	-14.0	8.8

Figure 4.1 – Comparison of the normalized equivalent resistance (ER) calculation (R'_f/R'_m) for the NF 270 membrane after 5.0 L of permeate filtered. Background solution: 10mM NaCl, pH = 6.0 ± 0.2. Experiments run with both colloid and organic present are listed as "ORGANIC + STXL" and are compared to the ER based on the individual components, "ER ORGANIC + STXL" for synergism.
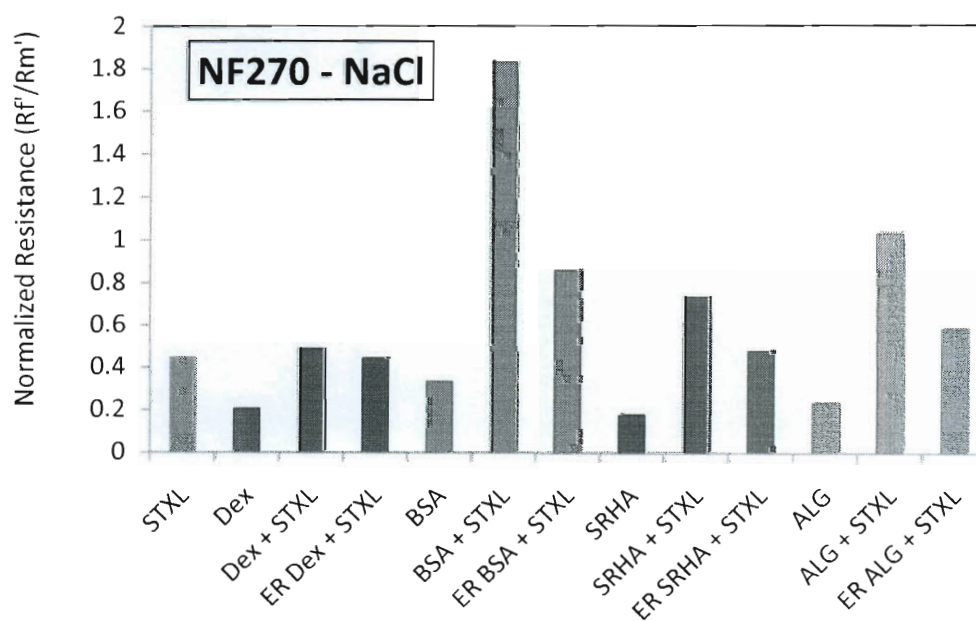
Figure 4.2 – Comparison of the normalized equivalent resistance (ER) calculation (R'_f/R'_m) for the LFC1 membrane after 5.0 L of permeate filtered. Background solution: (a)10mM NaCl, and (b) 7 mM NaCl/1 mM CaCl$_2$, pH = 6.0 ± 0.2. Experiments run with both colloid and organic present are listed as "ORGANIC + STXL" and are compared to the ER based on the individual components, "ER ORGANIC + STXL" for synergism.

b) **LFC1 – CaCl₂**

Normalized Resistance (R'_f/R'_m) (y-axis)

Categories (x-axis): STXL, Dex, Dex + STXL, ER Dex + STXL, BSA, BSA + STXL, ER BSA + STXL, SRHA, SRHA + STXL, ER SRHA + STXL, ALG, ALG + STXL, ER ALG + STXL
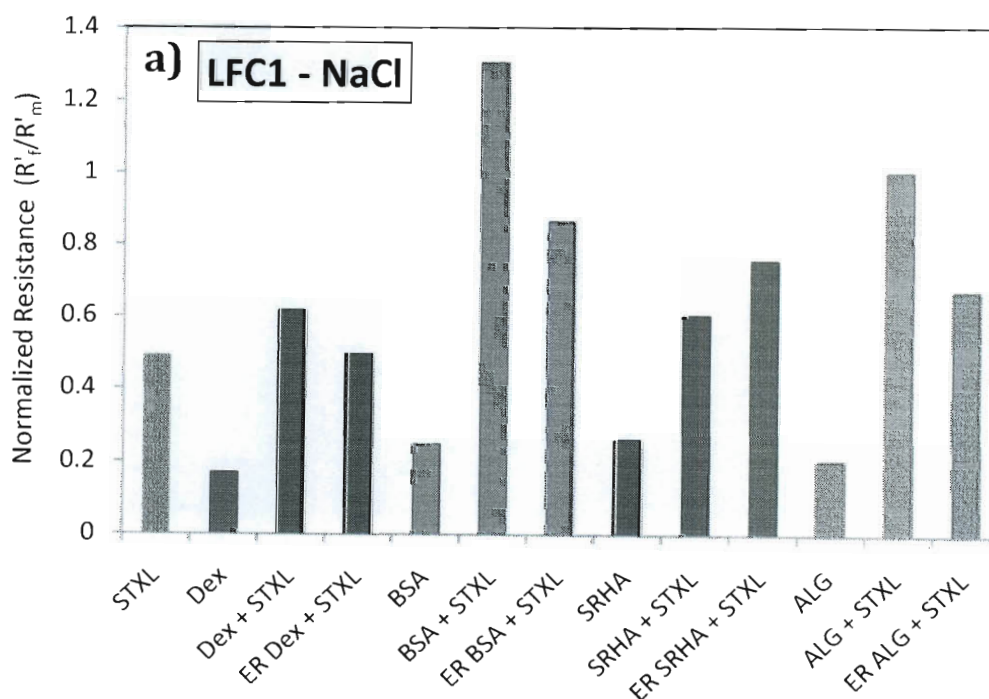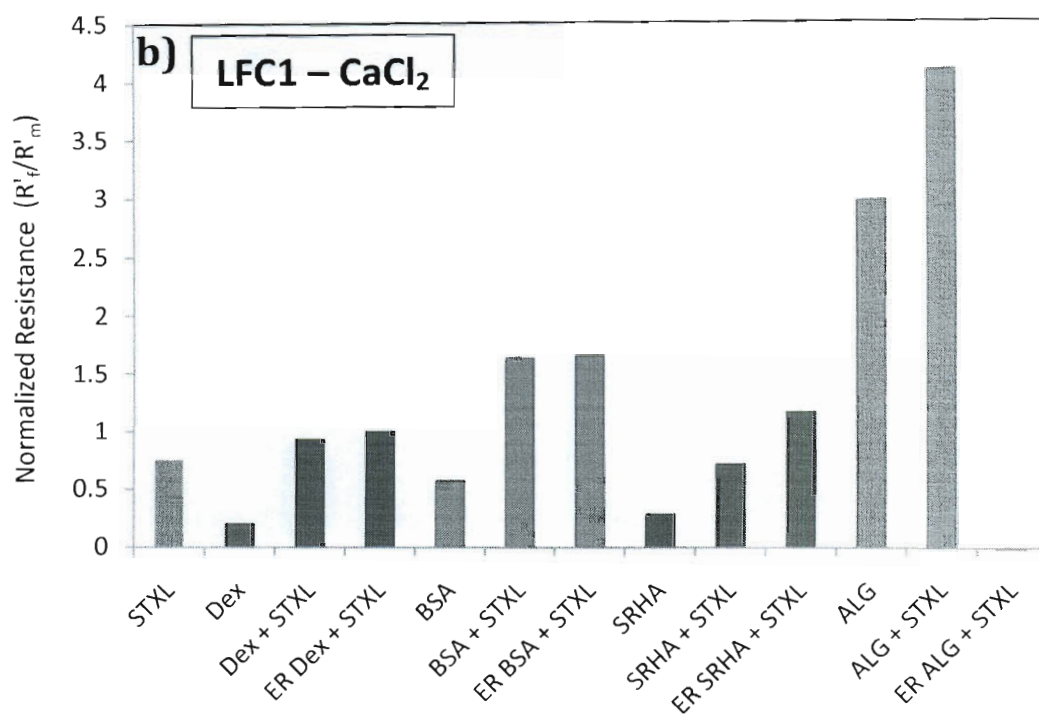
* The calculated ER ALG+STXL value during filtration in the presence of Ca²⁺ is -9.7, exposing a limitation of the calculation.

Figure 4.3 – Comparison of the normalized additive resistance (AR) calculation. Normalized fouling layer resistance (R_f/R_m) for the NF 270 membrane after 5.0 L of permeate filtered. Background solution: 10mM NaCl, pH = 6.0 ± 0.2. Experiments run with both colloid and organic present are listed as "ORGANIC + STXL" and are compared to the sum of the individual components, "SUM ORGANIC + STXL" for synergism.
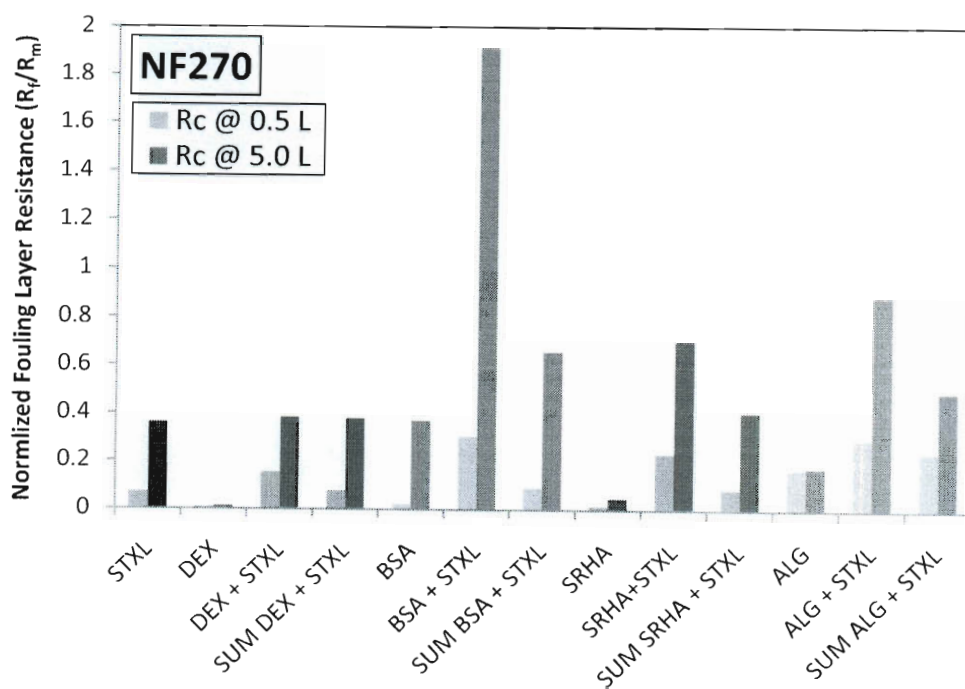
Figure 4.4 - Comparison of the normalized additive resistance (AR) calculation. Normalized fouling layer resistance (R_f/R_m) for the LFC 1 membrane after 5.0 L of permeate filtered, in both background solutions: a) 10mM NaCl and b) 7mM NaCl/1mM $CaCl_2$, pH = 6.0 ± 0.2. Experiments run with both colloid and organic present are listed as "ORGANIC + STXL" and are compared to the sum of the individual components, "SUM ORGANIC + STXL" for synergism.
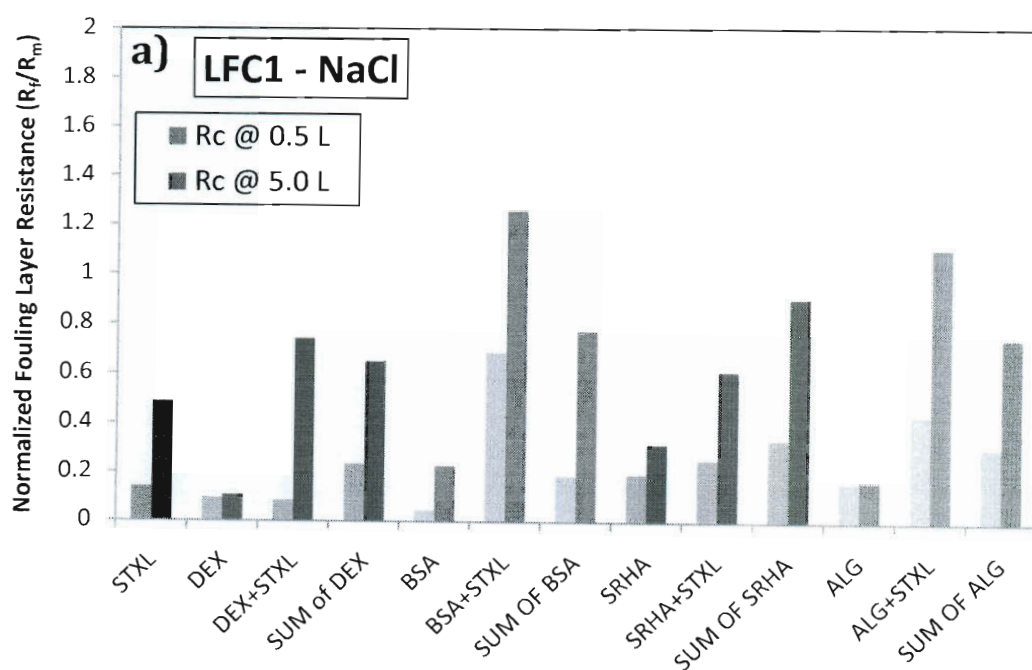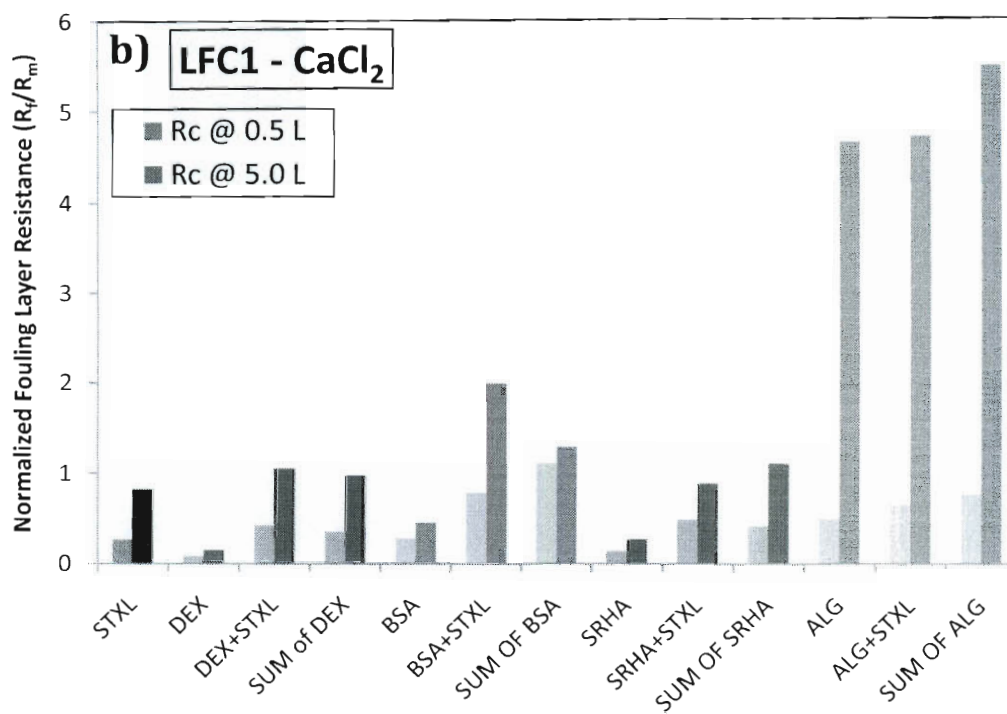
Figure 4.5 - TEM images of autopsied membranes: a) NF270 Virgin; b) LFC1 Virgin;

c) NF270 STXL layer in 10mM NaCl, and; d) NF270 BSA layer in 10 mM NaCl.
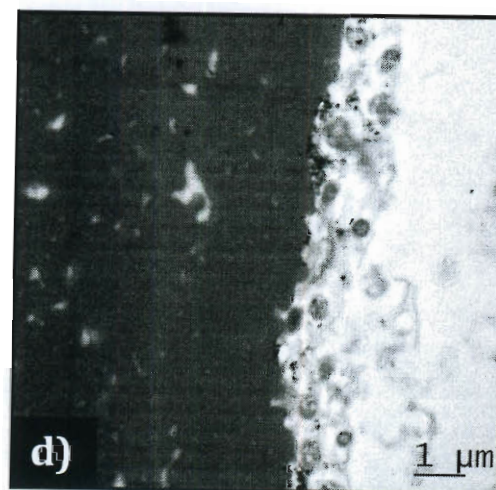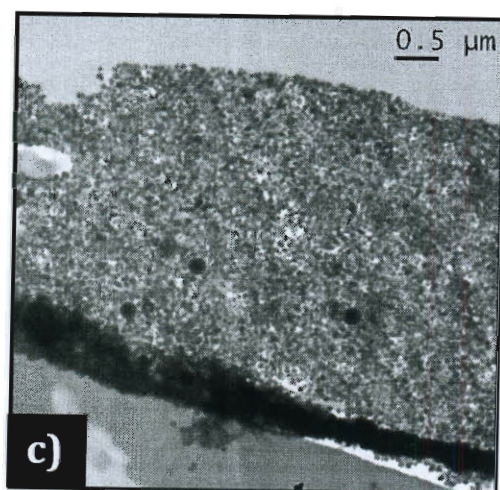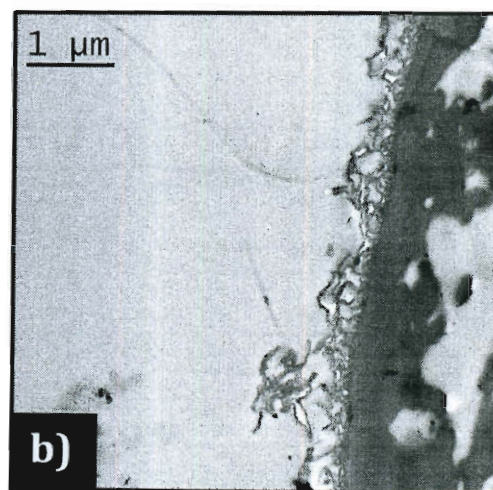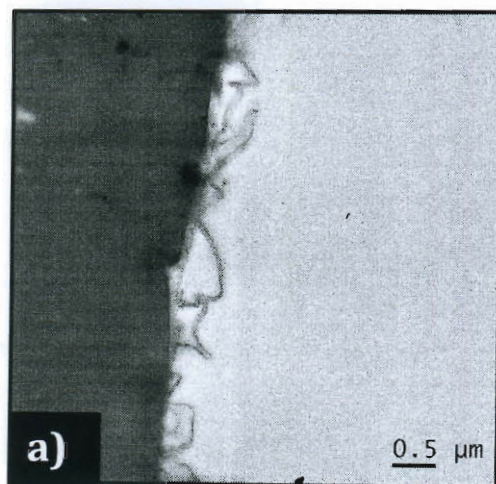
Figure 4.6 - TEM images of autopsied fouling layers a) NF270 STXL/Dex in 10mM NaCl; b) NF270 STXL/BSA layer in 10mM NaCl; c) LFC1 STXL/Dex in NaCl, and; d) LFC1 STXL/BSA in 10mM NaCl.
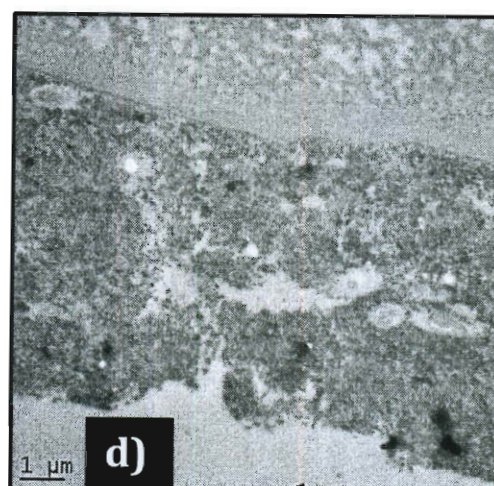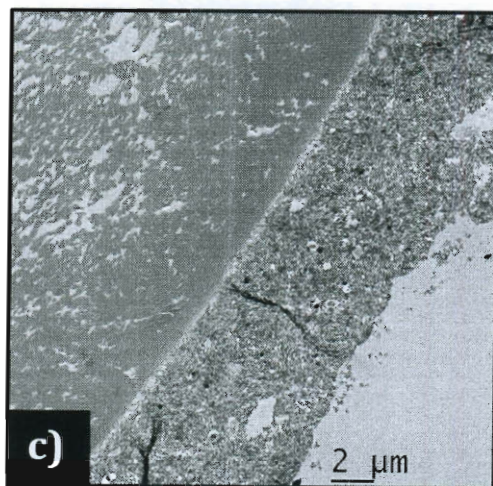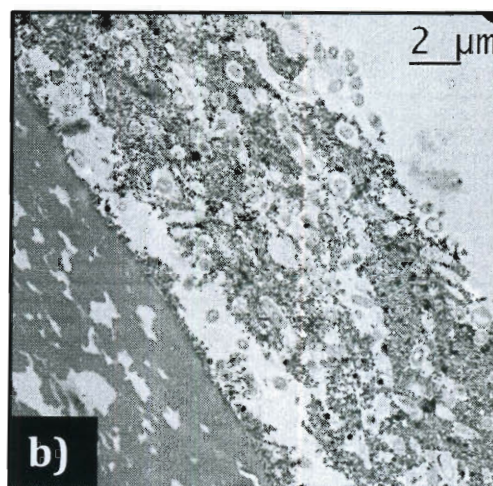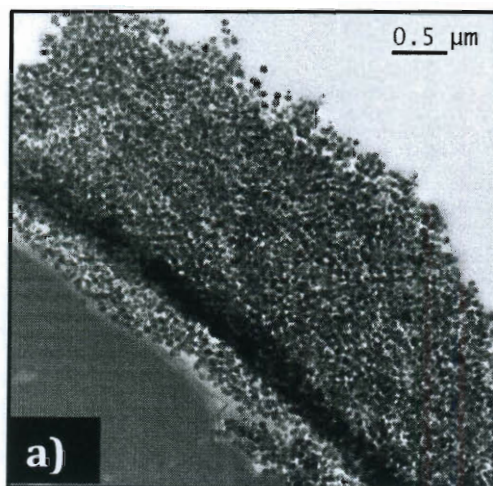
Figure 4.7 - TEM images of autopsied fouling layers a) NF270 STXL/HA in 10mM NaCl; b) NF270 STXL/Alg layer in 10mM NaCl; c) LFC1 STXL/HA in NaCl, and; d) LFC1 STXL/Alg in 10mM NaCl.
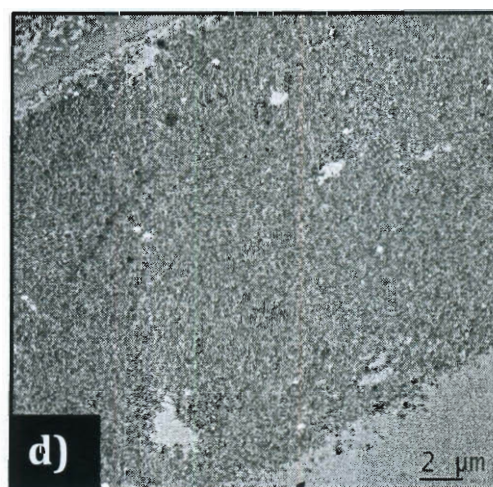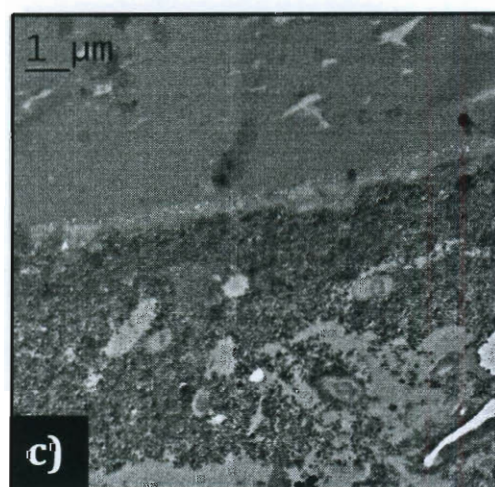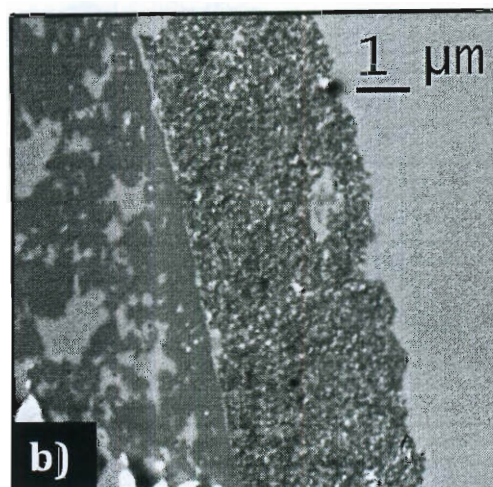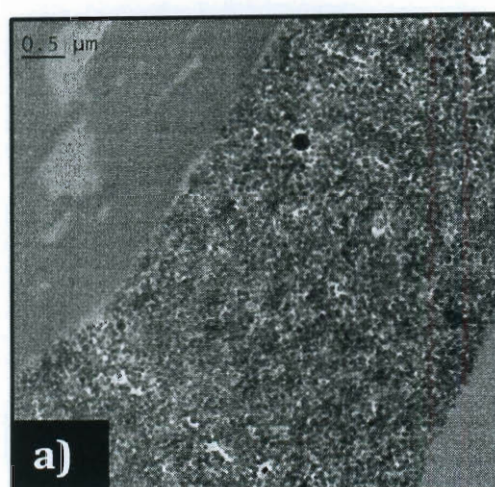
Figure 4.8 - TEM images of autopsied fouling layers formed on LFC1 in 7mM NaCl and 1mM $CaCl_2$, a) STXL/Dex layer; b) STXL/BSA layer; c) STXL/HA layer, and; d) STXL/Alg layer.
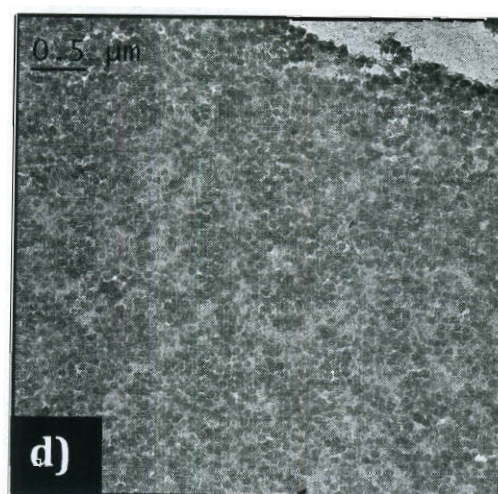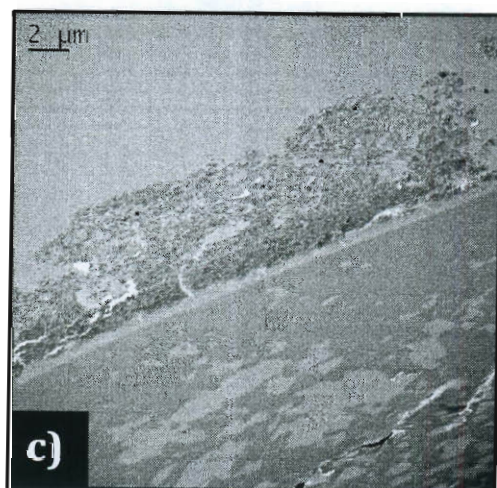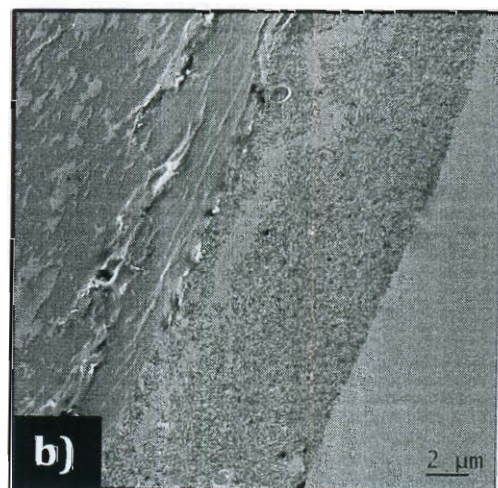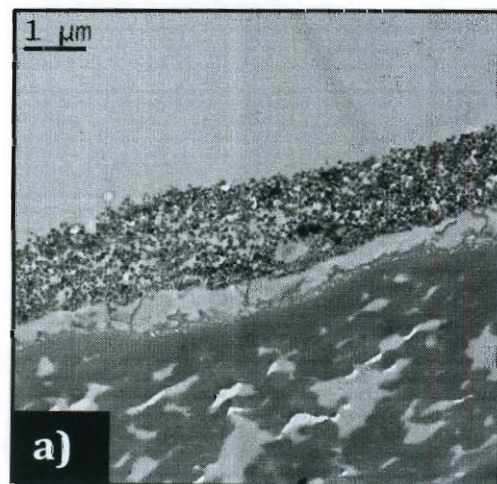
Chapter 5

Studying the Impact of Membrane Surface Chemistry on Adsorption and Cleaning of Organic Foulants using QCM-D[3]

5.1. Introduction

Thin-film composite (TFC) membranes are widely used in reverse osmosis (RO) and nanofiltration (NF) systems for desalination, ultra-pure water production, drinking water purification and wastewater reuse [4]. A major hindrance to wider application of NF and RO for water treatment is fouling of the membrane by mineral precipitation (scaling), colloidal or dissolved organic matter [29, 134, 135], and

---

[3] Manuscript submitted and in review at *Environmental Science and Technology.*

biofilm formation (bio-fouling) [142, 143]. Fine colloidal and dissolved organic compounds, including proteins, polysaccharides, and natural organic matter (NOM), are the most common foulants found in natural and wastewaters [125, 126, 144-146]. They can escape pretreatment and cannot be controlled by anti-scalants. In addition to increasing hydraulic resistance, adsorption of dissolved organic compounds forms the conditioning layer for bacterial adhesion and subsequent biofilm development [126, 127, 143]. The distribution and relative abundance of the adsorbed proteins and polysaccharides has been shown to influence the biofilm structure [147]. However, design of membrane materials resistant to organic fouling is a formidable challenge because our understanding of the main interactions controlling the organic foulant accumulation on RO and NF membranes is limited.

The influence of membrane properties such as hydrophobicity, charge, surface roughness, and porosity on fouling has been investigated in many previous studies [109, 148]. In particular, membrane surface hydrophobicity, usually determined by water contact angle measurement, was commonly related to organic fouling propensity [131, 135], although some recent studies showed that this was not always the case [131, 148]. Membrane surface properties such as hydrophobicity and charge are directly determined by membrane surface chemistry. Unfortunately the roles of specific chemical functionalities on membrane surfaces are largely unknown because of the chemical heterogeneity resulting from the interfacial polymerization that forms the thin active barrier in RO and NF membranes.

One possible route for simplifying the problem is to study the contribution of individual chemical functionalities using well-defined and homogenous surface chemistry. Whitesides and coworkers formed self-assembled monolayers (SAMs) of alkanethiolates with different ending chemical groups on gold surfaces to study the effect of surface wettability on non-specific adsorption of proteins and detergents [83]. Surface wettability of each monolayer , measured by water contact angle in cyclooctane, was correlated to adsorption of proteins and detergents measured by surface plasmon resonance (SPR); in general, adsorption was found to be higher on low-wettability surfaces with the polyethylene glycol monolayer being an exception, to which adsorption was lower than expected. Belfort and coworkers used atomic force microscopy (AFM) to evaluate the adhesion between several proteins, including bovine serum albumin (BSA), immobilized on gold surfaces and a series of SAMs with uncharged ending functionalities formed on AFM cantilevers [68]. They found a 'step-like' dependence of protein adsorption on surface wettability: surfaces with high wettability, i.e., those terminated with hydroxyl, amide and ethylene-glycol showed weak adhesion, while methyl, phenoxy, methoxy, trifluoromethyl and nitrile (low wettability) showed high protein adhesion. In another study, adsorption of BSA on a hydrophilic (-OH) and a hydrophobic ($-CH_3$) surface was studied using a combination of quartz crystal microbalance (QCM) and grazing angle Fourier transform infrared spectroscopy. It was found that BSA adsorption was accompanied by protein conformational changes and was higher on hydrophobic surfaces [97]. Other studies using similar approaches identified a number of

chemical functionalities that resist protein adhesion [84, 149]. In general, chemical moieties that are hydrophilic, include H-bond acceptors but do not include H-bond donors, and are electrically neutral were resistant to protein adherence.

Quartz-crystal microbalance with dissipation monitoring (QCM-D) is capable of measuring minute changes in mass adsorbed on a surface [130, 150]. The additional energy dissipation monitoring feature provides information on structure of the adsorbed layer. Quartz crystal sensors can be easily modified to yield a wide variety of surface chemistries. For example, gold-coated sensors were modified by aromatic polyamide mimetic of RO membranes in our recent study [151].

In this study we used QCM-D to investigate the adsorption equilibrium as well as kinetics of common organic foulants in wastewaters on SAMs of a variety of chemical functionalities. The effectiveness of different cleaning solutions in removing the adsorbed foulants was also evaluated. Our results suggest that membrane surface bulk properties such as hydrophobicity and charge are not reasonable predictors of organic foulant adsorption, especially for proteins. Specific interactions with individual chemical functional groups in many cases control adsorption equilibrium and kinetics as well as the removal of organic foulants by chemical cleaning. Surface modification of NF and RO membranes, therefore, should aim to minimize such specific interactions.

5.2. Experimental Section

5.2.1. Materials.

Alkanethiols (Table 5.1) used to create the SAMs were purchased in either neat form or premade solutions at 1 mM in 200 proof ethanol (Asemblon, Inc., Remond, WA). Sodium alginate (10 – 60 kDa) derived from brown algae and BSA (~ 66 kDa) were purchased from Sigma-Aldrich (St. Louis, MO). Surface zeta potential and hydrodynamic diameter of BSA and sodium alginate (Table 5.2) were characterized by electrophoretic mobility and dynamic light scattering (DLS) measurements using a Zetasizer Nano ZS (Malvern Instruments, Westborough, MA). Reagent grade NaCl, $CaCl_2$, NaOH, HCl and sodium-dodecyl-sulfate (SDS) were purchased from Sigma Aldrich (St. Louis, MO). All solutions were prepared using ultrapure water ($\geq$18.1 megaΩ-cm) produced by an E-Pure system (Barnstead, Batavia, IL).

5.2.2. Methods.

5.2.2.1. SAM preparation and characterization.

Seven SAMs each with a different ending functional group (Table 5.1) were prepared on both gold-coated QCM-D crystals (used for adsorption experiments) and gold-coated silicon wafers (for characterization) according to our previous publication [152] with slight modifications. Silicon wafers were cleaned

sequentially in acetone, methanol, and isopropanol in an ultrasonic bath (Bendeline Sonorex, London, England) followed by oxygen plasma cleaning for 5 min. They were then coated (one side polished, 330-μm thick) with a 10 nm titanium layer followed by a 30 nm gold layer at a pressure of 2×10^{-6} bar using a thermal evaporator (Odem Ltd., Rehovot, Israel).

Prior to self-assembly, gold-coated QCM-D crystals and silicon wafers were cleaned sequentially in toluene, acetone and ethanol twice in each solvent for 10 min each time in an ultrasonic bath. The substrates were then dried with ultrapure N_2 and exposed to UV/ozone in a ProCleaner chamber (Bioforce Nanosciences, Ames, IA) for 30 min. Clean substrates were first immersed in 1 mM alkanethiol solutions in ethanol for 24 h at room temperature. Prior to immersion, the pH of 11-Mercaptoundecanoic acid and 11-Amino-1-undecanethiol hydrochloride solutions was adjusted to 2 and 11, respectively, using 0.2 M HCl and NH_4OH to reduce electrostatic repulsion between thiol chains and create a more ordered, homogeneous surface. After self-assembly, the substrates were transferred to 1 mM dodecanethiol solutions in ethanol for an additional 24 h, dried in ultrapure N_2 and stored under vacuum.

The chemical composition of each SAM was analyzed by x-ray photoelectron spectroscopy (XPS) using ESCALAB 250 (Thermo Fisher Scientific Inc., Waltham, UK) with an Al x-ray source and a monochromator. Since XPS analysis is destructive, measurements were performed on SAMs formed on silicon wafers formed in parallel with SAMs on QCM-D crystals.

Thickness of the SAMs was estimated by Cauchy's equation [153] using an SE800 ellipsometer (Sentech Instruments GmbH, Berlin, Germany) with a light spot size of 0.5 cm^2. The phase difference between the s and p polarized waves and the amplitude attenuation were measured as a function of the wavelength from 380 to 820 nm at incidence angles of 60°, 65° and 70°. The optical constants of the underlying layers were determined based on measurements on a clean Au coated silicon wafer, and the refraction index of the organic layer was assumed to be 1.5 [154], which may introduce slight error in the calculated SAM thickness.

Static contact angle of water in air for the SAMs was measured using the sessile drop method with a CAM 200 contact angle analyzer (KSV Instruments LTD, Helsinki, Finland). Water drop size was approximately 2.0 μL. At least four measurements were taken per sample surface. Measurements were conducted both immediately after preparation of the SAMs and after QCM-D adsorption and cleaning experiments.

5.2.2.2. Adsorption experiments.

Adsorption of the model organic foulants was investigated using QCM-D (Q-Sense E4, Q-Sense, Glen Burnie, MD) on freshly prepared SAM coated quartz crystals. For a rigid adsorbed layer (i.e., negligible energy dissipation, ΔD), the adsorbed mass is proportional to the change in frequency as described by the Sauerbrey equation (Equation 5.1) [132]:

$$\Delta f = -\frac{2f_0^2}{A\sqrt{\rho_q \mu_q}} \Delta m \qquad\qquad \text{Equation 5.1}$$

where Δf is the change in frequency (Hz), Δm is the change in mass adsorbed (kg), f_0 is the resonant frequency (Hz) of the crystal sensor, A is the piezoelectrically active crystal area (m^2), and ρ_q and μ_q are the density (kg/m^3) and shear modulus (Pa) of quartz. For viscoelastic layers that exhibit high energy dissipations (ΔD), the vibrations amplify the shear acoustic wave such that Δf is not directly proportional to Δm. A viscoelastic model was used to fit the Δf and ΔD data simultaneously to determine the density (ρ_l), thickness (d_l), shear elastic modulus (μ_l), and viscosity (η_l) of the adsorbed layer[91-93].

In each experiment, fundamental frequencies of each crystal were first verified in air. A baseline was established by running the background electrolyte solution for 10 min at 50 µL/min (Reynold's number = 1.6×10^{-6}). This was followed by the adsorption step in which the organic foulant in the corresponding background solution was fed to the flow modules. After adsorption equilibrium was established, the influent was replaced with the background solution to remove the residual foulant solution and the subsequent equilibrium data were used for analysis.

After the foulant adsorption experiment, ultrapure water was pumped through the flow modules at 50 μL/min for 10 min to simulate hydraulic rinsing. The amount of foulant remaining was then measured in the background solution used for the adsorption experiment. The cleaning process was repeated with 2% SDS to evaluate the effectiveness of surfactant cleaning. Figure 5.1 shows an example of raw data collected from a typical adsorption and cleaning experiment.

Before each experiment, the crystal sensors and the flow modules were cleaned with 2% SDS followed by rinsing with ultrapure water for at least 1 hr at 100 μL/min and dried with ultrapure N_2.

5.3. Results and Discussion

5.3.1. SAM characterization.

SAMs were characterized by XPS, ellipsometry and water drop contact angle measurements and the results are summarized in Table 5.1. Water contact angles measured in air were similar to data previously reported for similar SAMs [155]. Ellipsometry measurements showed SAMs with thickness of 0.9 – 2.4 nm. XPS elemental analyses support the presence of the desired functional groups. A second immersion step in dodecanethiol solution was found to improve the homogeneity of the SAM surface, as evident by the small standard deviation of the water contact angles. XPS and contact angle measurements made with and without the second

immersion step suggest that the amount of dodecanethiol adsorbed in surfaces of other SAMs was very small.

5.3.2. BSA and alginate adsorption equilibrium on SAM surfaces.

5.3.2.1. Adsorption equilibrium data analysis.

BSA and alginate (at a concentration of 100 mg/L) were chosen as a model protein and polysaccharide, respectively, the predominant organic foulant types in wastewater [125, 126]. Because Ca^{2+} has been shown to play a key role in organic fouling of NF and RO membranes [18, 27, 148, 156, 157], adsorption experiments were performed in two electrolyte solutions: 10 mM NaCl or 7mM NaCl and 1mM $CaCl_2$ at an unadjusted pH of 6.0 ± 0.2.

Adsorption equilibrium occurred in all solution conditions in less than 2 hours, usually within an average of 1 hour. BSA adsorption in all experiments exhibited significant shift in frequency (Δf) but negligible change in dissipation (ΔD), suggesting the formation of a rigid BSA layer on the SAM surface. Therefore, the Sauerbrey equation (Equation 5.1) was applied and the calculated adsorbed mass was converted to layer thickness assuming a layer density of 1100 kg/m³. The calculated adsorbed mass of BSA and alginate is presented in Figure 5.2 as a function of water contact angle on the sensor.

Notable ΔD (greater than 1) was observed in most experiments with alginate. In a few cases when ΔD was smaller than 1 and Δf was extremely low the normalized dissipation ($\Delta D/\Delta f$) was used to determine the applicability of the Sauerbrey equation. All adsorbed alginate layers either had ΔD values greater than 1 or $\Delta D/\Delta f$ values greater than 0.1 (Table 5.3). Therefore, the visco-elastic model (Q-Tools 3.0) was used for all alginate adsorption data. Density of the alginate layer determined using the viscoelastic model ranged from 1075 to 1100 kg/m³. Bulk fluid density was calculated to be 997.1 kg/m³ and fluid viscosity was 0.001 kg/m·s. All experiments were evaluated for the 3rd (n = 3) and 5th (n = 5) harmonics, but only data from the 3rd harmonic is presented in this paper.

5.3.2.2. Relationship between organic adsorption and surface wettability.

Equilibrium adsorption of BSA and alginate was related to the hydrophobicity of the SAMs as measured by the cosine of water contact angle, θ (Figure 5.2). A correlation analysis between $cos(\theta)$ and adsorbed mass was performed using the Pearson product-moment coefficient (PPMC) to evaluate linear correlation and with the Spearman's rank correlation to determine monotonic dependence [30, 158]. BSA adsorption in the presence and absence of calcium did not correlate with water contact angle by either analysis (Figure 5.2a), indicating that hydrophobicity alone is not a strong predictor of BSA adsorption.

Among the uncharged surfaces, the highly hydrophobic surfaces (-CH$_3$ and -OPh) adsorbed significant amounts of BSA (approximately a monolayer according to the calculated thickness), while the hydrophilic -EG$_6$OH and -OH surfaces showed low adsorption, consistent with previous studies [68, 97]. The -EG$_6$OH surface, in particular, was resistant to BSA adsorption due to its hydrophilicity and electrosteric effect [83, 149, 159]. Interestingly, the -CONH$_2$ surface, with a water contact angle similar to that of the -OH surface, adsorbed notably higher amounts of BSA (600 ng/cm^2) in the absence of Ca^{2+}. This can be attributed to hydrogen bonding between the -CONH$_2$ surface and multiple amine groups on BSA. This observation is different from that by Sethuraman *et al.* [68], who measured adhesion forces between four immobilized proteins and a series of chemical groups, and found similar values for -CONH$_2$, -OH and -EG$_6$OH surfaces. In their study immobilization of the proteins may have limited specific interactions including hydrogen bonding with the SAMs. Hydrogen bonding may also have contributed to BSA adsorption on the -OH surface, which was higher than that predicted from its very low contact angle.

The positively charged -NH$_2$ and negatively charged -COOH surfaces adsorbed significantly more BSA than the -EG$_6$OH and -OH surfaces, which had similar contact angles. This is consistent with a previous study on BSA adsorption on SAMs using SPR [160]. BSA adsorption on the -NH$_2$ and -COOH surfaces were similar to that on the highly hydrophobic -CH$_3$ and -OPh surfaces even though the surfaces were much more hydrophilic. Adsorption on the -NH$_2$ surface was the

highest likely due to the strong electrostatic attraction between the negatively charged BSA molecules and the positively charged $-NH_2$ SAM ($pK_a \sim 7.5$) [161]. The high BSA adsorption on the -COOH surface despite its hydrophilicity and negative charge is attributed to the charge heterogeneity of BSA: positively charged amine groups were present even though the net charge was negative. Silin *et al.* [160] also suggested that the presence of positively charged sites on the overall negatively charged BSA led to electrostatic interactions with the negatively charged -COOH SAM.

In summary, BSA adsorption equilibrium data suggest that specific interactions, e.g., between $-CONH_2$ or -OH and BSA, play an important role in BSA adsorption in addition to the non-specific electrostatic and hydrophobic interactions; charge heterogeneity can lead to significant adsorption when the overall electrostatic interaction is repulsive. Therefore, water contact angle measured in air and surface zeta potential are not good indicators for protein adsorption; membranes with higher negative zeta potential due to the presence of -COOH groups may be more prone to protein fouling.

In contrast to BSA, alginate adsorption on all SAMs correlated well with water contact angle, where $-CH_3$ and -OPh showed the highest adsorption (Figure 5.2b). Although $-EG_6OH$ surfaces have been shown to be the most resistant to protein adsorption [83, 149], alginate (polysaccharide) adsorption shows a different pattern, where the most hydrophilic surfaces (-OH and $-CONH_2$) had the lowest alginate adsorption (Figure 5.2b). The mass of alginate adsorbed on the hydrophilic

surfaces was less than that of a monolayer, indicating patched adsorption (Figure 5.4). Although alginate has been reported to foul NF and RO membranes more severely than BSA [71, 136], our measurements show similar adsorption of both, indicating the greater fouling rate of alginate is likely due to faster gel layer formation.

5.3.2.3. Effect of calcium on adsorption.

Calcium showed an intense effect on alginate adsorption, and moderate effect on BSA adsorption. The effect of Ca^{2+} on BSA adsorption depended on the particular surface functionality. In the presence of Ca^{2+}, BSA adsorption on the $-CONH_2$ and $-COOH$ surfaces decreased (Figure 5.2a). This is consistent with the complexation of Ca^{2+} with $-COOH$ groups on both the BSA and the SAM. BSA adsorption increased on the $-OH$ surface and decreased on $-CH_3$. This could be explained by changes in surface interaction energy of BSA and the SAMs, as has been shown for alginate and RO membranes [162].

Addition of Ca^{2+} increased alginate adsorption intensely on all SAMs tested (Figure 5.2b). Alginate has the propensity to aggregate and form cation-stabilized gels due to a high carboxyl content (approximately 61% mannuronic acid and 39% guluronic acid) [121, 162]. Ca^{2+} has also been reported to decrease the cohesive free energy of alginate and decrease the free energy of adhesion between alginate and RO membranes [162]. As a result, both the adsorbed mass (Figure 5.2b) and

adsorbed layer thickness (Figure 5.3) of alginate increased in the presence of Ca^{2+}. The gel formation was also evident in the increased viscosity of all adsorbed alginate layers (Figure 5.4).

5.3.3. Surface chemistry effect on adsorption kinetics.

Adsorption kinetics of organic foulants is important as it is related to the initial fouling rate on a clean membrane as well as changes in membrane surface properties. Mass adsorption kinetics curves of BSA and alginate were obtained from time-resolved Δf and ΔD data, and the initial adsorption rate determined from the linear section of kinetics curve was shown in Figure 5.4.

Despite comparable adsorbed mass at equilibrium (Figure 5.2), initial fouling rates on all SAMs were markedly higher for BSA than alginate (Figure 5.4). This result suggests that proteins could be a dominant component in the initial conditioning layer and consequently play a critical role in membrane bio-fouling even though its quantity in the fouling layer may be low. Adsorption kinetics of both BSA and alginate strongly depended on the type of SAM. In NaCl, BSA initial adsorption rate followed the order of -COOH > -CH$_3$ > -OPh > -NH$_2$ > -OH > -CONH$_2$ > -EG$_6$OH, showing no correlation to water contact angle. The presence of Ca^{2+} increased BSA adsorption rate on most SAMs except for the two most hydrophobic surfaces, -CH$_3$ and -OPh, on which BSA adsorption decreased compared to that in NaCl.

Initial alginate adsorption rates were much lower than those of BSA (Figure 5.4) and were consistently higher in the presence of Ca^{2+} on all SAMs, even though alginate formed large aggregates in solution (Table 5.2) which reduces the diffusive mass transfer. This increase in adsorption rate is attributed to enhanced alginate-alginate attraction and is consistent with increased membrane fouling rates observed with alginate in the presence of Ca^{2+} [163].

The -COOH surface showed the greatest initial adsorption rate for both BSA and alginate. These results suggest higher initial protein and polysaccharide fouling rates on membranes that expose -COOH groups and further support that specific interactions may delineate fouling properties more accurately than non-specific hydrophobic interactions.

5.3.4. Adsorbed layer structure.

In addition to the total mass and thickness, the structure of the organic gel layer plays a critical role in determining the hydraulic resistance of the gel layer. The normalized dissipation, $\Delta D/\Delta f$, provides structural information of the adsorbed layer. Figure 5.5 presents ΔD as a function of Δf at adsorption equilibrium for both BSA and alginate. The BSA or alginate layers formed on different SAMs showed similar normalized dissipation, indicating that surface chemistry did not affect the structure of the adsorbed layer at equilibrium. All alginate layers exhibited much higher $\Delta D/\Delta f$ than the BSA layers, showing that alginate layers are looser and more

elastic than the BSA layers. The rigid structure of the BSA layer was not affected by Ca^{2+}, while the alginate layer in the presence of Ca^{2+} is denser and probably more cross-linked. However, this effect cannot be observed in Figure 5.5 because the increase in $\Delta D/\Delta f$ due to higher viscosity counter balances the effect of higher density. A similar plot of ΔD vs. Δf during the adsorption process illustrates the dynamic change of the adsorbed layer structure (Figure 5.6). BSA adsorption exhibited a two–phase growth with notable faster increase in ΔD in the second phase, suggesting changes in BSA molecular conformation or orientation [97, 160, 164]. Such change in structure strongly depended on the SAM ending functionality. Despite of the overall rigidity, the adsorbed BSA layer on all SAMs exhibited two–phase growth (Figure 5.6a and Figure 5.6b). At the beginning of the experiment, the surface was not fully covered; $\Delta D/\Delta f$ was low. In the later stage of the adsorption, the slope of the curve or $\Delta D/\Delta f$ increased markedly, suggesting changes in BSA molecular conformation or orientation (seen more clearly in Figure 5.6c and Figure 5.6d) [97, 160, 164]. Little structural change was observed during formation of the visco-elastic alginate layers, as shown by the linear relationship between ΔD and Δf throughout the whole adsorption process (Figure 5.6e and Figure 5.6f). Slight compaction was observed on the -NH_2 and -OH SAMs.

These results suggest that membrane surface chemistry does not affect the specific resistance of BSA or alginate fouling layer. However, when other foulants are also present, which is the case for any natural water or wastewater, the impact of surface chemistry on the initial structure of the adsorbed protein layer may play a

role in the subsequent attachment of other foulants (e.g., mineral precipitates and bacterial cells) and consequently the structure of the fouling layer.

5.3.5. Cleaning of adsorbed organic foulants on SAMs.

The effectiveness of cleaning with DI water and 2% SDS was evaluated sequentially by the fraction of mass removed (Figure 5.7). DI water rinsing was not very effective, with -14 to 52% removal (negative values resulted from adsorbed layer swelling). SDS cleaning was more effective, removing 21 to 100% of the adsorbed mass. In general, cleaning efficiency for alginate was much greater than for BSA, indicating that proteins may contribute to irreversible fouling more than polysaccharides. Although the two most hydrophobic SAMs (-CH$_3$ and -OPh) adsorbed a large amount of BSA and alginate, the adsorbed foulants can be removed relatively effectively by SDS cleaning. SAMs of -NH$_2$, -COOH, and -CONH$_2$, however, consistently showed significant residual BSA and/or alginate. Despite the importance of Ca^{2+} in adsorption equilibrium and kinetics, Ca^{2+} did not significantly affect BSA irreversible fouling of any SAMs except the -NH$_2$ and -CONH$_2$ surface, for which irreversible fouling increased greatly in the presence of Ca^{2+}. This phenomena was extended to -NH$_2$ for alginate. These results indicate that -CONH$_2$ and especially -NH$_2$ on membrane surfaces may contribute more to irreversible fouling of NF and RO membranes than other functional groups under typical wastewater solution conditions.

5.3.6. Implications for membrane fouling.

Understanding factors controlling organic foulant adsorption on NF and RO membranes is important for developing fouling resistant membranes and other fouling control strategies such as pretreatment and chemical cleaning. Our study shows direct evidence for the first time that specific interactions, such as hydrogen bonding and electrostatic interaction between specific functionalities, play a more important role than non-specific electrostatic and hydrophobic interactions in adsorption of and irreversible fouling by proteins and polysaccharides. Because the initial adsorption of proteins and polysaccharides (i.e., surface conditioning) has important impacts on the subsequent formation of scales and bio-films, these results suggest that specific surface functionality may be more important than bulk surface properties, such as zeta potential and hydrophobicity, in long term fouling and cleaning of NF and RO membranes. Therefore, surface modifications of NF and RO membranes that minimize the presence of H-bond donor and acceptor (e.g., -COOH, -NH$_2$) as well as charged sites may be an effective approach to develop fouling resistant membranes. We also show for the first time that proteins, although usually found in smaller quantity on fouled membranes [165, 166], adsorb much faster to functional groups typically found on NF and RO membrane surfaces and are more difficult to remove by chemical cleaning than polysaccharides. These results suggest that proteins play an important role in initiating bio-fouling despite their smaller

quantity. Therefore, pretreatment and chemical cleaning methods should also target

protein removal.

Table 5.1 - Characteristics of SAMs on gold prepared in this study.

Terminal Group	Alkanethiol compound	Contact Angle[†] (°)	Thickness (nm)	XPS Elemental Composition (10^{-2})*	
				O/C	N/C
-CH$_3$	1-Dodecanethiol	102.6 ± 3.7	0.91	0.99	—
-OPh	11-Phenoxy undecanethiol	91.2 ± 3.5	0.97	8.95	—
-NH$_2$	11-Amino-1-undecanethiol, hydrochloride	63.3 ± 3.2	1.43	0.16	15.2
-EG$_6$OH	(1-Mercapto-11undecyl) hexa(ethylene glycol)	43.2 ± 4.3	1.62	21.4	—
-COOH	11-Mercaptoundecanoic acid	42.1 ± 6.7	1.25	24.6	—
-CONH$_2$	11-Mercaptoundecaneamide	35.7 ± 4.0	1.25	16.9	9.45
-OH	11-Hydroxy-1-Undecanethiol	34.2 ± 2.5	2.41	19.1	—

[†] Average of 10 surfaces tested. * By Peak Area analysis.

Table 5.2 - Hydrodynamic diameter and zeta potential of foulants (pH 6.0 ± 0.2).

Model Foulant	10 mM NaCl [136]		7 mM NaCl, 1 mM CaCl$_2$	
	Zeta Potential (mV)	Hydrodynamic Diameter (nm)	Zeta Potential (mV)	Hydrodynamic Diameter (nm)
BSA	-20.7 ± 0.9	6.9 ± 0.2	-11.4 ± 0.7	6.8 ± 0.5
Sodium Alginate	-45.0 ± 1.2	5.12 ± 2.2	-37.6 ± 2.3	12.8 ± 2.6

Table 5.3 - Raw Δf (Hz) and ΔD (×10⁻⁶) values for each surface tested under each solution condition tested. $\Delta D/\Delta f$ values for each surface are included in order to determine which model to use.

Organic Foulant		BSA		Alg	
Solution Condition		10mM NaCl	7mM NaCl 1mM CaCl₂	10mM NaCl	7mM NaCl 1mM CaCl₂
-CH₃	Δf	-41.4	-30.7	-17.9*	-26.5
	ΔD	0.92	0.59	6.43	8.93
	$\Delta D/\Delta f$	-0.02	-0.02	-0.36	-0.33
-OPh	Δf	-27.8	-28.0	-11.51	-23.9
	ΔD	0.75	0.59	4.89	8.08
	$\Delta D/\Delta f$	-0.03	-0.02	-0.43	-0.34
-NH₂	Δf	-58.1	-56.8	-5.4	-22.0
	ΔD	1.47	1.32	1.29	5.07
	$\Delta D/\Delta f$	-0.03	-0.02	-0.23	-0.23
-EG₆OH	Δf	-4.2	-8.0	-3.2	-12.5
	ΔD	-0.40	0.71	1.03	4.64
	$\Delta D/\Delta f$	0.09	-0.09	-0.32	-0.37
-COOH	Δf	-44.5	-36.3	-7.2	-19.0
	ΔD	1.57	0.75	3.16	5.99
	$\Delta D/\Delta f$	-0.03	-0.02	-0.44	-0.31
-CONH₂	Δf	-34.3	-21.7	-4.3	-2.9
	ΔD	0.72	0.63	1.45	0.79
	$\Delta D/\Delta f$	-0.02	-0.03	-0.34	-0.17

-OH	Δf	-19.6	-26.9	*-2.2*	*-11.0*
	ΔD	0.86	0.86	*0.98*	*1.71*
	$\Delta D/\Delta f$	-0.03	-0.03	*-0.45*	*-0.15*

* *Italicized* values are modeled using the visco-elastic model, while all others are assumed rigid and modeled using the Sauerbrey equation

Figure 5.1 - Changes in frequency and dissipation during an adsorption and cleaning experiment. Experiment shown is the adsorption of 100 mg/L BSA in 10 mM NaCl on the $-CH_3$ SAM.
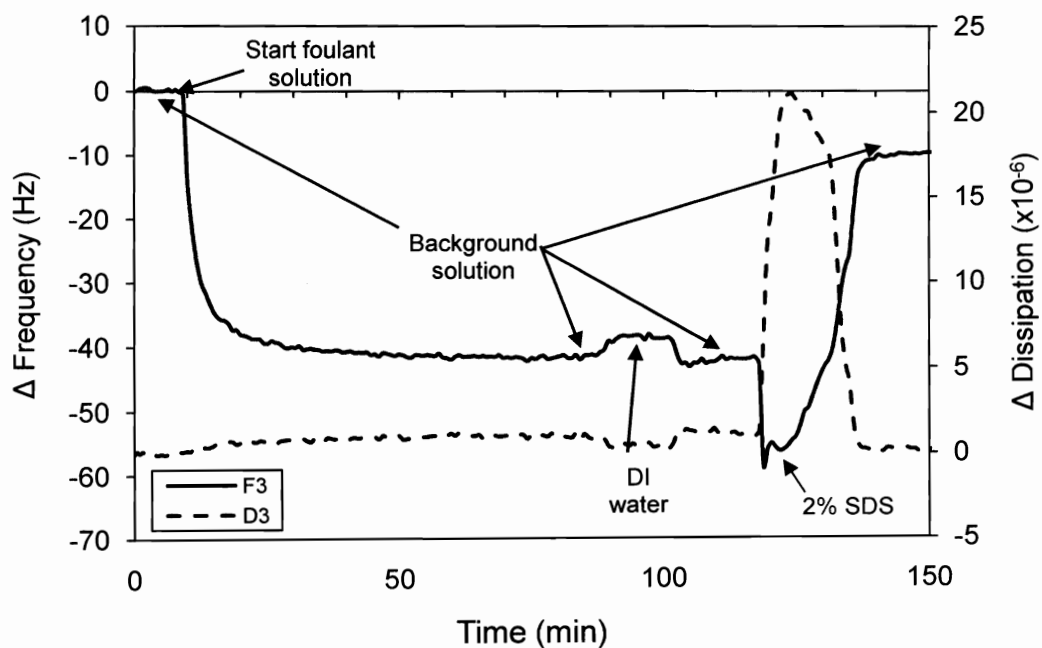
Figure 5.2 - Calculated adsorbed mass a) BSA, and b) sodium alginate on different

SAMs at equilibrium. Adsorption occurred in 10 mM NaCl (solid symbols) and 7 mM

NaCl/1 mM CaCl$_2$ (open symbols).
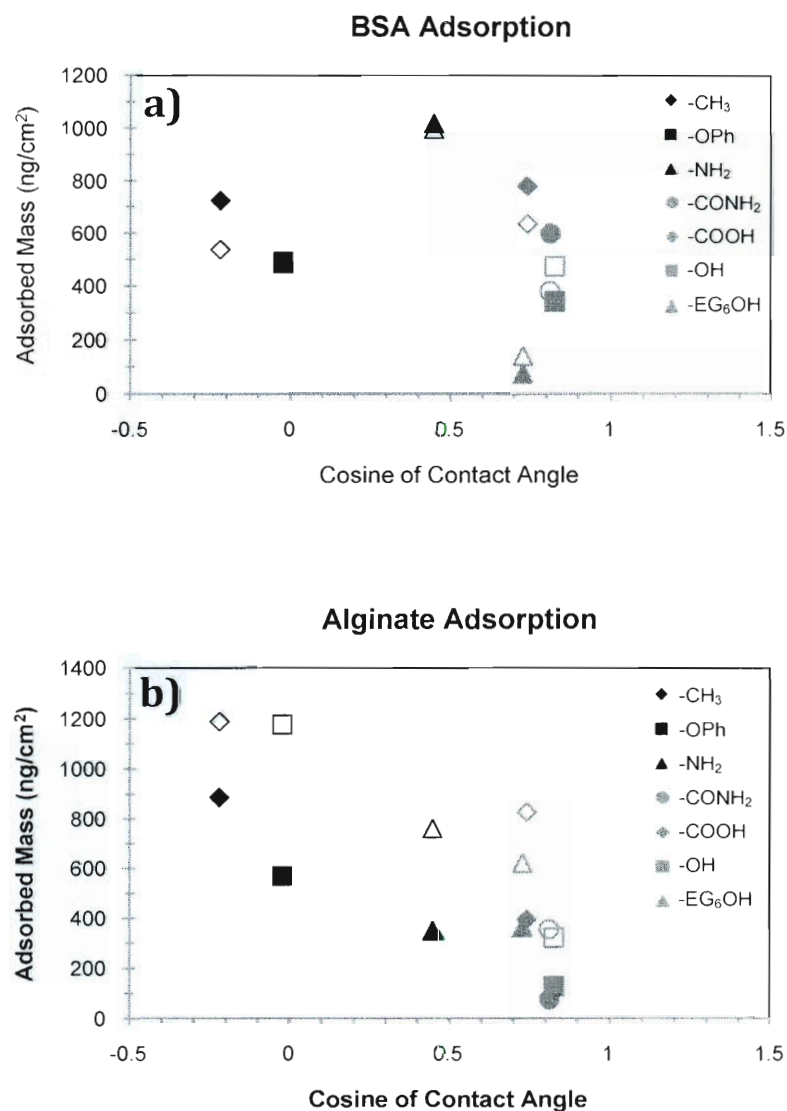
Figure 5.3 - Calculated thickness and viscosity of adsorbed alginate layers in 10 mM

NaCl and 7 mM NaCl with 1 mM $CaCl_2$.
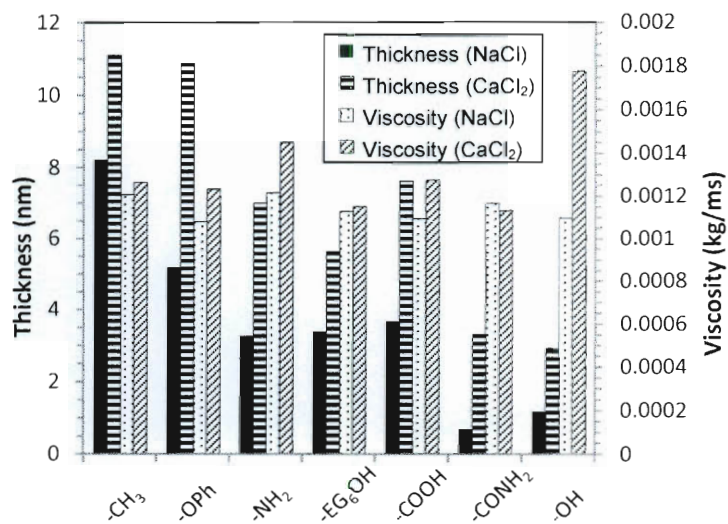
Figure 5.4 - Initial adsorption rate of BSA and alginate.
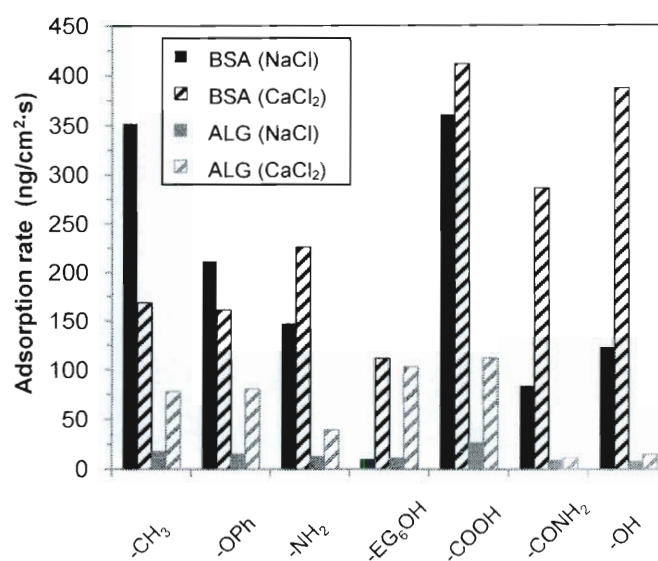
Figure 5.5 - Measured dissipation change (ΔD) and frequency change (Δf) at

adsorption equilibrium.
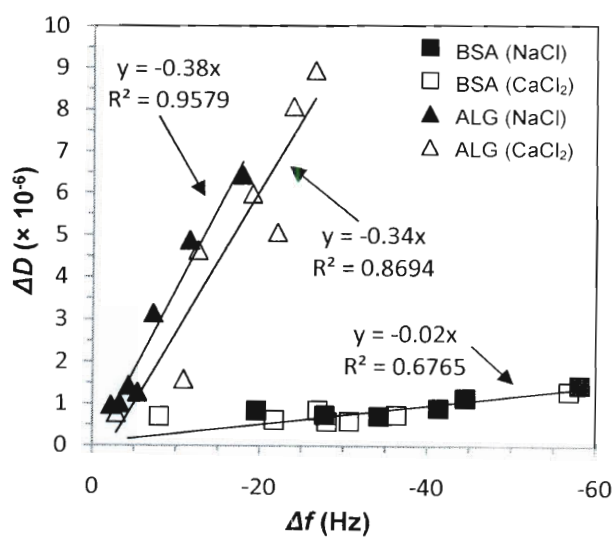
Figure 5.6 - Evolution of BSA and alginate layers illustrated by ΔD vs. ΔF curves.
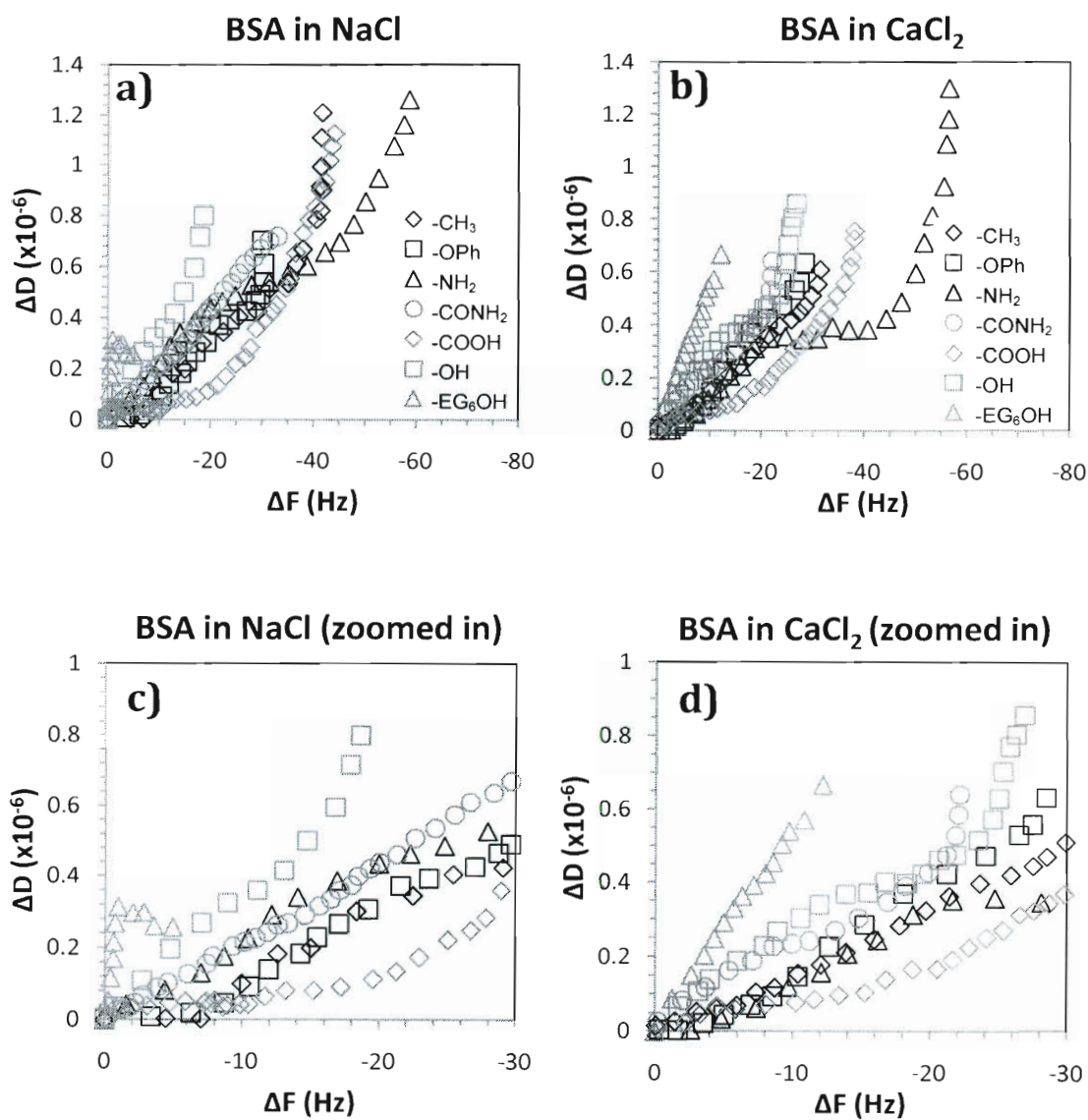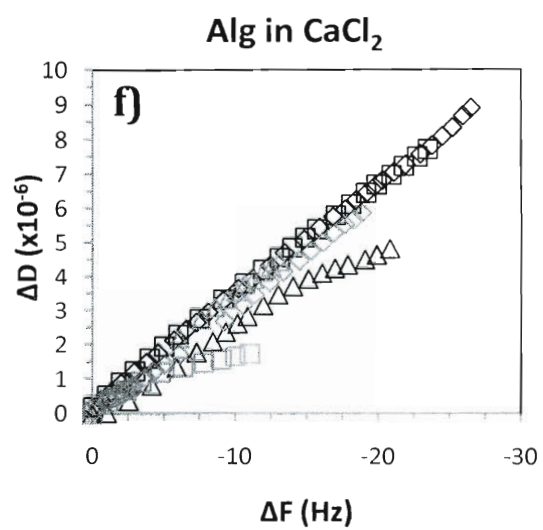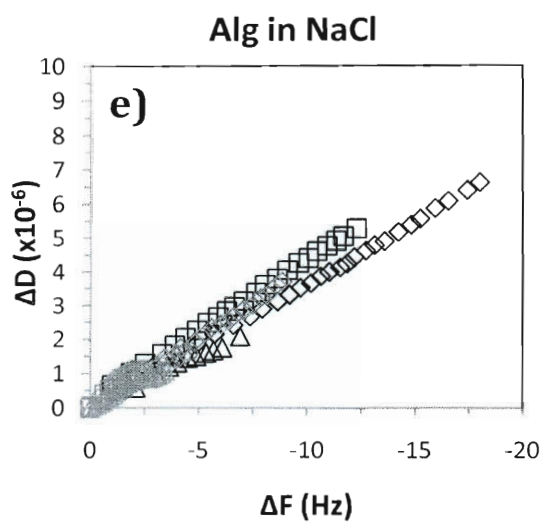
Figure 5.7 - Stacked bar graph indicating % mass of adsorbed layer removed by DI (solid) and 2% SDS cleaning (pattern).
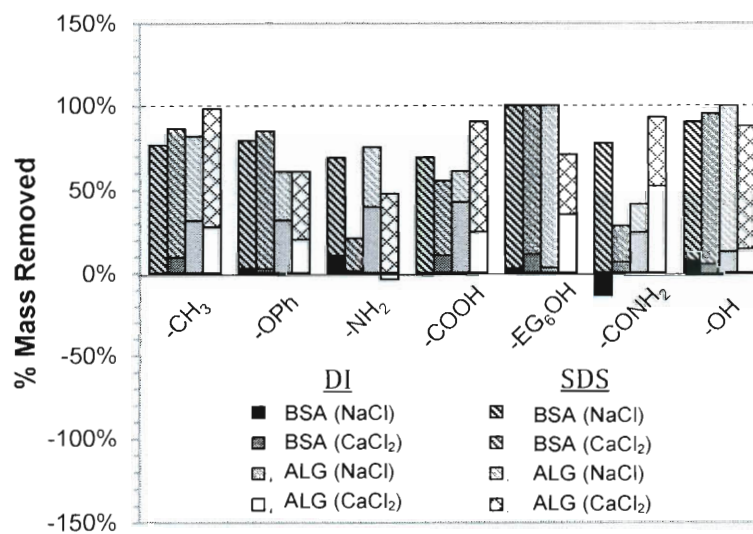
Chapter 6

Surface and Interfacial Free Energy Analysis for Characterizing Organic Foulant Adsorption on Membrane Surface Functionalities [4]

6.1. Introduction

Understanding the role of membrane surface properties in membrane fouling is critical to the development of fouling resistant membranes and other fouling control strategies. Although the impact of membrane surface charge, hydrophobicity and roughness have been studied extensively, little has been done to elucidate the role of membrane surface chemistry due to the highly heterogeneous

---

[4] Manuscript in preparation for submission to *Journal of Membrane Science*.

nature of membrane surfaces. On the other hand, several studies have shown that specific interactions between the foulant and chemical functionalities on the membrane surface play a key role in organic and biological fouling. Unfortunately, traditional approaches to studying membrane adsorption through filtration and flux decline experiments are not sensitive enough to identify the interactions that control initial fouling by adsorption. By developing a better understanding of organic adsorption interactions across a wide range of surface functionality relevant to membrane chemistry, adsorption at the membrane surface can be avoided by developing better anti-fouling membrane coatings and materials.

Our previous research has shown that hydrophobicity as measured through water contact angle alone is not sufficient for determining adsorption and fouling propensity[167]. Although nonspecific organic adsorption is complex and not well understood, several chemical and physical approaches can be applied to explain these complicated interactions. DLVO theory, named for the Dutch and Russian scientists Derjaguin, Landau, Vervey, and Overbeek that simultaneously studied this phenomena, incorporates attractive (van der Waals) and repulsive (electrostatic double layer) interactions to describe the overall picture of stability of hydrophobic colloids [73, 74]. However, too often these two interactions cannot accurately describe the interactions that lead to colloidal membrane fouling [75]. Among a variety of other reasons that the discrepancies may be ascribed to, including chemical and morphological heterogeneity of the membrane surface and interactions [22, 76], additional interactions between the membrane and foulant

induced by the polarity of the solvent has also be observed, which lead to the school of thought that proposes an extended DLVO (or xDLVO) type of approach [77, 78]. The extended DLVO theory includes the additional short-range acid-base interaction between two surfaces immersed in a polar solvent such as water, quantified by the measurement of surface tensions of various substances, to which polymeric surfaces are shown to have a significant acid-base contribution [78]. Several studies have shown that polymeric surfaces have a substantial acid-base contribution [55, 71, 79, 80]. Previous studies have shown that membrane flux decline of both colloids and some organics can be accurately described using an extended DLVO theory that includes acid-base interactions [71, 79, 80, 162]. However, this phenomenon has not been linked to specific membrane chemistry or properties responsible in order to create anti-fouling surfaces.

Of the various organic macromolecules present in natural and wastewaters, protein adsorption has been the most heavily studied. Extensive work has shown that adsorption of proteins onto solid surfaces is entropically driven [58-66]. Expectedly, electrostatic interactions strongly influence not only protein adsorption [58-64, 66], but also protein configuration upon adsorption [67]. "Flat" configurations of proteins were found to occur by adsorbing highly charged polyelectrolyte onto highly charged positive or negative surfaces [67]. The affinity of a protein to adhere to a surface increases with the hydrophobicity of the surface [54, 68-70] and the concept of using hydrophobicity of membranes to assess their

propensity to foul has also been established [55, 56, 71, 72], although it does not fully account for all adsorption phenomena [167].

Organic adsorption studies are limited by the heterogeneity of surface upon which adsorption takes place. Self-assembled monolayers (SAMs) of long-chain ω-functionalized alkanethiolates prepared on gold films have been established as excellent homogeneous model systems for studying the interactions of proteins with organic surfaces [94, 95]. Although SAMs can serve as great models of mono-functionalized surfaces, actual thin-film composite membranes include a combination of several functional groups. To date, instrument limitations have prevented the study of organic adsorption on membrane surfaces directly.

Quartz-crystal microbalance with dissipation monitoring (QCM-D) is capable of measuring minute changes in mass adsorbed on a surface [130, 150]. The additional energy dissipation monitoring feature provides information on structure of the adsorbed layer. Quartz crystal sensors can be easily modified to yield a wide variety of surface chemistries. For example, gold-coated sensors was modified by aromatic polyamide mimetic of RO membranes in a recent study [151].

In this study, we seek to explain organic adsorption onto specific chemical moieties through a thermodynamic analysis of surface tensions and interfacial free energies. Isolating the effect of van der Waals and acid-base components of adsorptive interactions will help reveal a more mechanistic understanding of the

initial adsorption that affects initial fouling layer and subsequent fouling layer formation onto membrane functional groups that represent clean membranes.

6.2. Theory

In this study, surface free energies of different functionalized surfaces are evaluated based on an approach that incorporates the sum of van der Waals and acid-base components. Presence of either specific or electrostatic interactions will be determined from deviating adsorption behavior. Comparing these energetic values to adsorbed mass will enable us to determine if the organic adsorption is being caused by either of these interactions or if unaccounted for interactions, such as electrostatic or hydrogen bonding are present.

Contact angles were converted to interfacial free energies using the DLVO approached outlined by van Oss [78]. Van Oss shows that the acid-base component (γ^{AB}) of the interfacial tension and the Lifshitz-van der Waals (γ^{LW}) component are additive:

$$\gamma^{TOT} = \gamma^{AB} + \gamma^{LW}$$ Equation 6.1

where the acid-base component is comprised of two non-additive parameters [168], the electron acceptor surface tension parameter (γ^+) and the electron-donor surface tension parameter (γ^-), which are related through:

$$\gamma^{AB} = 2\sqrt{\gamma^+ \gamma^-}$$ Equation 6.2

Combining both the Young-Dupré and the Dupré equation yields a force-balance equilibrium equation that comprises both the polar and apolar interactions that depicts the free energy of adhesion between a liquid and a solid [78]:

$$(1+\cos\theta)\gamma_L = 2\left(\sqrt{\gamma_S^{LW}\gamma_L^{LW}} + \sqrt{\gamma_S^+\gamma_L^-} + \sqrt{\gamma_S^-\gamma_L^+}\right)$$ Equation 6.3

The unknown surface tension parameters of the solid surface ($\gamma_S^{LW}, \gamma_S^+, \gamma_S^-$) can be determined using the contact angle measurements of three probe liquids with known surface tension parameters ($\gamma_L^{LW}, \gamma_L^+, \gamma_L^-$). According to van Oss [78], the three liquids should be high energy to produce easily measured contact angles and one of the three probe liquids should be apolar (in order to calculate γ_S^{LW}) and the other two polar liquids.

The Young-Dupré equation [169] also derives the solid-liquid interfacial free energy, ΔG_{SL}, from liquid contact angle:

$$-\Delta G_{SL} = \gamma_L \left(1 + \cos\theta_L\right)$$

Equation 6.4

Classically, "lyophilic" or "wetting" interaction has been defined as the contact angle less than 90° or a ΔG_{SL} value larger than that of the liquid. "Lyophobic" or "non-wetting" materials have contact angles greater than 90° or ΔG_{SL} value smaller than that of the liquid.

Although traditionally used to explain colloid interaction, surface tensions calculated in Equation 6.3 can then be used to evaluate the interfacial free energies per unit area between a surface/membrane and an organic macromolecule [71, 80, 162]. Expressions for the LW (ΔG_{SLO}^{LW}) and AB (ΔG_{SLO}^{AB}) components of interfacial free energy per unit area are given by [78]

$$\Delta G_{SLO.y_0}^{LW} = 2\left(\sqrt{\gamma_L^{LW}} - \sqrt{\gamma_S^{LW}}\right)\left(\sqrt{\gamma_O^{LW}} - \sqrt{\gamma_L^{LW}}\right)$$

Equation 6.5

and

$$\Delta G^{AB}_{SLO,y_0} = 2\sqrt{\gamma_L^+}\left(\sqrt{\gamma_S^-} + \sqrt{\gamma_O^-} - \sqrt{\gamma_L^-}\right) + 2\sqrt{\gamma_L^-}\left(\sqrt{\gamma_S^+} + \sqrt{\gamma_O^+} - \sqrt{\gamma_L^+}\right) - 2\left(\sqrt{\gamma_S^+\gamma_O^-} + \sqrt{\gamma_S^-\gamma_O^+}\right)$$

Equation 6.6

where y_0 is the minimum equilibrium cut-off distance where contact between the two surfaces assumed to occur. This value is usually 0.158 nm ($\pm$ 0.009 nm) and can be considered as the distance between the outer electron shells of adjoining non-covalently interacting molecules [170]. The free energy of adhesion ($\Delta G_{SLO}{}^{TOT}$), describes the attraction or repulsion of a solid material interacting with another solid material, through a liquid media and is defined as the sum of $\Delta G^{LW}_{SLO,y_0}$ and $\Delta G^{AB}_{SLO,y_0}$ (i.e., a solid surface and an organic macromolecule). The free energy of cohesion ($\Delta G_{OLO}{}^{TOT}$), describes the energetic favorability of a solid material to interact with itself in a liquid media and is defined as the sum of $\Delta G^{LW}_{OLO,y_0}$ and $\Delta G^{AB}_{OLO,y_0}$ (i.e., for a given scenario $\gamma_S = \gamma_O$). A negative free energy represents a thermodynamically unstable state (attractive), while a positive free energy represents a stable state (repulsive).

Additionally, surface tension of water with high, salt water type concentrations has been found to deviate significantly from pure water. An empirical formula has been derived by Fleming and Revelle to relate the surface tension of pure water to temperature and salt content:

$$\gamma_L = 75.64 - 0.144(T) + 0.0399(Cl^-)$$

Equation 6.7

where temperature (T) is in degrees Celsius and chloride concentration (Cl⁻) is reported in grams per liter.

6.3. Materials and Methods

6.3.1. Model organic foulants.

Humic acid, sodium alginate and bovine serum albumin (BSA) were chosen as the three natural organic matter, polysaccharide and protein model organic foulants, respectively, for their well-defined characterization and representative presence in natural and wastewaters. Sodium alginate (ALG) derived from brown algae (10 – 60 kDa) and BSA (~ 66 kDa) were purchased from Sigma-Aldrich (St. Louis, MO). Suwannee river humic acid (SRHA - standard II) was obtained from International Humic Substances Society (St. Paul, MN). SRHA stock solution was prepared by dissolving the SRHA powder at pH 8.2 (adjusted using 1 M NaOH) followed by vacuum filtration (Whatman Grade No. 1 filter paper, England). Surface zeta potential and hydrodynamic diameter of BSA, SRHA and sodium alginate were characterized by electrophoretic mobility and dynamic light scattering (DLS) measurements using a Zetasizer Nano ZS (Malvern Instruments, Westborough, MA). Reagent grade NaCl, CaCl₂, NaOH, HCl and sodium-dodecyl-sulfate (SDS) were

purchased from Sigma Aldrich (St. Louis, MO). All solutions were prepared using ultrapure water (≥18.1 megaΩ-cm) produced by an E-Pure system (Barnstead, Batavia, IL).

6.3.2. SAM surfaces.

Seven SAMs each with a different ending functional group (Table 6.1) were prepared on both gold-coated QCM-D crystals (used for adsorption experiments) and gold-coated silicon wafers (for characterization) according to a previous publication [152] with slight modifications. Alkanethiols used to create the self assembled monolayers (SAMs) were purchased in either neat form or premade solutions at 1 mM in 200 proof ethanol (Asemblon, Inc., Remond, WA) [167].

Prior to self-assembly, gold-coated QCM-D crystals were cleaned sequentially in toluene, acetone and ethanol twice in each solvent for 10 min each time in an ultrasonic bath. Silicon wafers were cleaned sequentially in acetone, methanol, and isopropanol in an ultrasonic bath (Bendeline Sonorex, London, England) followed by oxygen plasma cleaning for 5 min. Both substrates were then dried with ultrapure N_2 and exposed to UV/ozone in a ProCleaner chamber (Bioforce Nanosciences, Ames, IA) for 30 min. Clean substrates were first immersed in 1 mM alkanethiol solutions in ethanol for 24 h at room temperature. Prior to immersion, the pH of 11-Mercaptoundecanoic acid and 11-Amino-1-undecanethiol hydrochloride solutions was adjusted to 2 and 11, respectively, using 0.2 M HCl and NH_4OH to reduce

electrostatic repulsion between thiol chains and create a more ordered, homogeneous surface. After self-assembly, the substrates were transferred to 1 mM dodecanethiol solutions in ethanol for an additional 24 h, dried in ultrapure N_2 and stored under vacuum. The chemical composition of each SAM was analyzed by x-ray photoelectron spectroscopy (XPS) using ESCALAB 250 (Thermo Fisher Scientific Inc., Waltham, UK) with an Al x-ray source and a monochromator. Since XPS analysis may contaminate the SAMs, measurements were performed on SAMs formed on silicon wafers formed in parallel with SAMs on QCM-D crystals.

Thickness of the SAMs was estimated by Cauchy's equation [153] using an SE800 ellipsometer (Sentech Instruments GmbH, Berlin, Germany) with a light spot size of 0.5 cm². The phase difference between the s and p polarized waves and the amplitude attenuation were measured as a function of the wavelength from 380 to 820 nm at incidence angles of 60°, 65° and 70°. The optical constants of the underlying layers were determined based on measurements on a clean Au coated silicon wafer, and the refraction index of the organic layer was assumed to be 1.5 [154], which may introduce slight error in the calculated SAM thickness.

6.3.3. Surface thermodynamic analysis.

Static contact angle in air of each SAM was measured using the sessile drop method with a CAM 200 contact angle analyzer (KSV Instruments LTD, Helsinki, Finland). Water drop size was approximately 2.0 µL and at least five measurements

were taken per sample. Contact angles were measured using three probe liquids (deionized water, diiodomethane, and glycerol, Sigma-Aldrich, St. Louis, MO). Surfaces measured include the seven different SAM surfaces as well as filtered organic lawns of the three model foulants (ALG, BSA, and SRHA), prepared as described in [78].

6.3.4. Adsorption experiments.

Adsorption of the model organic foulants was investigated using QCM-D (Q-Sense E4, Q-Sense, Glen Burnie, MD) on freshly prepared SAM coated quartz crystals. All experiments employ background solutions of 10 mM NaCl or 7 mM NaCl and 1 mM $CaCl_2$, an organic foulant concentration of 100 mg/L and a flow-rate of 50 µl/min. In each experiment, fundamental frequencies of the crystal are first verified under dry air conditions, followed by establishing a baseline by running the respective background solution for 10 min. This is followed by the adsorption phase using the organic foulant solution. After adsorption equilibrium is established the buffer is reintroduced in order to remove bulk viscosity effects and adsorbed layer mass was measured at this point. A more detailed experimental protocol was described previously [167].

6.4. Results and Discussion

6.4.1. Organic adsorption equilibrium data analysis.

Adsorption equilibrium data analysis for alginate and BSA adsorbed layers are presented in an earlier section (Adsorption equilibrium data analysis – page 126). Adsorbed layers of SRHA had a dissipation of less than 1 and were modeled using the Sauerbrey equation (Equation 5.1) to calculate adsorbed mass. Thickness of the adsorbed layers was determined assuming a density of 1100 kg/m^3. Figure 6.1 and Figure 6.2 present the adsorption equilibrium vs. water contact angle of SAM surface and thickness of the SRHA adsorbed layers, respectively. SRHA adsorption follows a linear correlation as determined by the Pearson product moment correlation coefficient (PMCC) [30] to the cosine of the water contact angle in solutions of 10 mM NaCl, with more adsorption on higher water contact angle. In the presence of CaCl$_2$, adsorbed mass of SRHA at equilibrium is greater and similar on different SAMs, with the exception of the -EG$_6$OH surface which resists adsorption of SRHA in both solution conditions). Previous studies have indicated that Ca^{2+} complexation occurs in the presence of NOM and humic acid [171], which reduces the humic acid zeta potential and increases adsorption. Additional adsorbed mass in the presence of Ca^{2+} is likely due to increased SRHA-SRHA interaction and not to additional adsorption to the SAM surface itself.

6.4.2. Organic–liquid and SAM–liquid interfacial free energy.

Characterization of the SAMs is presented in Table 6.1. Probe liquid compositions and liquid surface tensions reported from literature are detailed in Table 6.2. Equation 6.7 was used to calculate the adjusted surface tension parameter due to the presence of salt ions in the electrolyte solutions of interest. Due to the low concentration (10 mM ionic strength for both solutions) γ_L for the electrolyte solutions only decreased to 72.77 (from 72.80 for pure water[78]). This adjusted surface tension coupled with electrolyte liquid contact angles (Table 6.3) and the Young-Dupré equation (Equation 6.4) was used to calculate the solid-liquid interfacial free energy between the organic and SAM surfaces (Table 6.4 and Table 6.5). Due to the low salt concentrations, changes in contact angles were very slight as were solid-liquid interfacial energies. Alginate and SRHA had slightly increased solid-liquid interfacial free energies in the presence of Ca^{2+}, while BSA remained the same. These results were much lower in magnitude than has been reported for salt concentrations exceeding 32g/L NaCl[162]. All organics were lyophilic or "wetting" for both electrolyte solutions, given that ΔG_{SL} is more negative than the liquid surface tensions. All SAM layers were also lyophilic, with the exception of -CH$_3$ and –OPh as they had solid-interfacial free energies more positive than the liquids themselves.

6.4.3. Organic-organic free energies of cohesion.

A negative free energy of cohesion describes an organic that is thermodynamically unstable in the liquid, while a positive free energy of cohesion suggests stability. Table 6.4 presents the surface tension parameters (the van der Waals, electron-acceptor, electron-donor, acid-base, and total surface tension) as well as the free energies of cohesion (ΔG_{OLO}) calculated by the protocol described by van Oss [78]. These values agree well with values found on similar organics previously [71, 80]. Additionally, it has been reported that a large portion of materials[168], including proteins[172] and polysaccharides[173], are γ^- monopoles with very low electron accepting capacity, and therefore do not have strong γ^{AB} contributions. With negative free energies of cohesion, alginate and SRHA are considered thermodynamically unstable in water, which is reflected in the solution preparation protocol (6.3.1 Model organic foulants), while BSA would be considered stable. However, stability is also determined kinetically through electric double layer interactions in water. Given the negative charge of all three organics (Table 5.2 and Appendix A) in the measured solution conditions, the presence of carboxylate and other acidic moieties increases the inherent stability of these macromolecules.

6.4.4. SAM surface tensions and organic–SAM free energies of adhesion.

Table 6.5 presents the van der Waals, electron-acceptor, electron donor, acid-base, and total surface tensions as well as the free energies of adhesion with each

organic. $-CH_3$ and $-OPh$ resist oxidation and reduction and therefore have low acid-base surface tension. As non-polar functionalities, the van der Waals component is also low, resulting in lyophobic or "non-wetting" surfaces. The $-NH_2$ surface is formed at a high pH past its pKa [167], ensuring completely reduced NH_2 and a high electron donating surface tension. Amide ($-CONH_2$) surface is a weak base over the solution conditions tested and therefore has more mixed electron-donor/acceptor surface tensions. The polarity of $-COOH$ creates a tendency to "self-associate", so the carboxyl surface has high acid-base and van der Waals surface tension components. Hexa(ethyleneglycol) ($-EG_6OH$) and the hydroxyl functionality both have high concentration of $-OH$ whose polarity increases the surface tension parameters through increased van der Waals and acid-base components.

Organic-membrane interfacial free energies of adhesion give insight into the probability of an organic being attracted and adsorbing to or being repelled from the SAM surface (Table 6.5). For each SAM and organic combination, the relative amounts of the acid-base component of the free energy of cohesion (ΔG_{SLO}^{AB}), the van der Waals component of the free energy of cohesion (ΔG_{SLO}^{LW}), and the total free energy of adhesion (ΔG_{SLO}^{TOT}), are shown in Figure 6.3. The attraction due to van der Waals forces is relatively small, so that the total free energy of each SAM-organic combination is largely dictated by the acid-base contribution. Increasingly positive (or decreasingly negative) values indicate less organic-membrane attraction (or greater organic-membrane repulsion). Values of adsorbed organic mass vs. free energy of that respective organic are illustrated in Figure 6.4 and the PMCC for

correlation analysis is reported in Table 6.6. All three organic macromolecules followed this order of decreasing free energy of adhesion: $-CH_3$ > $-OPh$ > $-NH_2$ > $-EG_6OH$ > $-CONH_2$ > $-OH$ > $-COOH$. Both alginate and SRHA follow the expected trend of increasingly positive free energy of adhesion with decreased adsorbed mass, indicating that van der Waals and Lewis acid-base contributions to adsorptive interactions are sufficient for predicting their relative adsorption, even in the presence of divalent ions, with the exception of $-COOH$. More adsorption was seen on $-COOH$ surface than predicted by the thermodynamic analysis. BSA adsorption does not follow the order suggested by the free energy of adhesion analysis, indicating that other interactions such as electrostatic or hydrogen bonding, which are not fully accounted for in this surface free energy analysis, are responsible for adsorption. As a protein, the structure of BSA is different that the polysaccharide and natural organic matter. Its tendency to create hydrogen bonds with the amine, amide, carboxyl, and hydroxyl surfaces increases the adsorbed mass at equilibrium on those surfaces. $-EG_6OH$ surfaces resist adsorption of both BSA and SRHA beyond what is predicted due to electrosteric interactions.

6.4.5. Correlation of adsorption rate with free energy of adhesion.

The free energy of adhesion is an indicator of the strength of the attractive and repulsive forces between the organic and the membrane and it has been shown to correlate well with the initial rate of flux decline, which is also governed by interfacial interactions between foulants and clean membrane [162]. The free energies of adhesion are plotted vs. the initial adsorption rate, as defined by the

linear portion of the adsorption kinetics curve, in Figure 6.5, however correlation is not significant for any of the SAM-organic pairs (PMCC < 0.3 or > -0.3). For alginate and SRHA, solutions containing Ca^{2+} formed bridges with the carboxyl in the organic and had higher adsorption rates overall. Because this surface free energy analysis is a thermodynamic approach that assumes equilibrium conditions, it does not appear to be a good predictor for adsorption rate kinetics.

6.5. Conclusions

Although membrane flux decline due to organic filtration has been explained using a thermodynamic surface free energy analysis previously, understanding what membrane material or membrane chemistry resists adsorption at a theoretical level has been less clear. Additionally, a thermodynamic approach for organic fouling onto commercial membranes does not account for specific interactions that may occur or for membrane imperfections and heterogeneity. In this study we aim to explain organic adsorption of three model foulants onto specific chemical functionalities relevant to membrane chemistry using surface and interfacial free energies which account for van der Waals and Lewis acid-base interactions. Surface and interfacial free energy analysis revealed that acid-base contributions for all three organics impact total interfacial free energy much more on each SAM than van der Waals interactions. The mass of alginate and SRHA adsorbed layers correlates strongly with the interfacial free energy of adhesion in both electrolyte conditions.

However, for the surfaces tested BSA adsorption does not correlate at all. Because this approach neglects to incorporate electrostatic interactions, which have been shown to be important for protein adsorption, xDVLO theory would likely better represent protein adsorption onto specific charged functional groups and should be explored in the future. Hydrogen bonding is a special polar interaction and is not fully accounted for in this analysis either but likely contributes to adsorption.

Table 6.1 - Characteristics of SAMs on gold prepared in this study.

Terminal Group	Alkanethiol compound	Contact Angle[†] (°)	Thickness (nm)	XPS Elemental Composition (10^{-2})*	
				O/C	N/C
-CH₃	1-Dodecanethiol	102.6 ± 3.7	0.91	0.99	—
-OPh	11-Phenoxy undecanethiol	91.2 ± 3.5	0.97	8.95	—
-NH₂	11-Amino-1-undecanethiol, hydrochloride	63.3 ± 3.2	1.43	0.16	15.2
-EG₆OH	(1-Mercapto-11undecyl) hexa(ethylene glycol)	43.2 ± 4.3	1.62	21.4	—
-COOH	11-Mercaptoundecanoic acid	42.1 ± 6.7	1.25	24.6	—
-CONH₂	11-Mercaptoundecaneamide	35.7 ± 4.0	1.25	16.9	9.45
-OH	11-Hydroxy-1-Undecanethiol	34.2 ± 2.5	2.41	19.1	—

[†] Average of 10 surfaces tested. * By Peak Area analysis.

Table 6.2– Probe liquid surface tension parameters [78].

	γ^L	γ^{LW}	γ^{AB}	γ^+	γ^-	η
Water	72.8	21.8	51	25.5	25.5	0.01
Glycerol	64	34	30	3.92	57.4	14.9
Diiodomethane	50.8	50.8	0	0	0	0.028

Table 6.3 – Contact angles (°) and standard deviations as measured on each created SAM and organic film using solutions of 10mM NaCl and 7mM NaCl/1mM $CaCl_2$ as well as the three probe liquids. Average of at least 6 measurements.

Surface or -R Group	Contact Angles (°) Using Probe Liquid				
	NaCl	*CaCl$_2$*	*Water*	*Glycerol*	*Dioodomethane*
Alginate	59.2 ± 5.2	62.1 ± 2.2	59.5 ± 2.2	57.2 ± 1.5	51.5 ± 3.1
BSA	39.1 ± 1.9	38.3 ± 1.5	37.9 ± 5.5	51.9 ± 0.5	42.1 ± 0.8
SRHA	52.0 ± 0.3	55.0 ± 0.6	53.1 ± 0.3	48.0 ± 4.2	50.9 ± 2.5
-CH$_3$	108.3 ± 0.4	109.2 ± 1.1	108.7 ± 1.1	96.7 ± 2.3	73.6 ± 1.1
-OPh	93.4 ± 1.4	95.0 ± 0.4	90.1 ± 0.9	78.1 ± 1.5	46.0 ± 1.8
-NH$_2$	60.7 ± 3.5	61.2 ± 3.1	57.7 ± 3.1	58.7 ± 1.8	35.0 ± 2.0
-COOH	31.5 ± 2.8	32.4 ± 5.9	33.5 ± 2.9	46.2 ± 1.3	41.1 ± 1.4
-CONH$_2$	42.2 ± 1.3	45.6 ±2.1	41.9 ± 2.2	46.9 ± 0.8	34.5 ± 2.3
-EG$_6$OH	44.5 ± 2.0	47.5 ± 0.9	44.3 ± 2.0	46.2 ± 1.2	36.8 ± 0.4
-OH	29.0 ± 1.4	36.5 ± 2.7	29.4 ± 1.5	38.5 ± 2.5	30.2 ± 1.5

Table 6.4 - Organic surface tensions, organic-liquid interfacial free energies (ΔG_{SL} - mJ/m^2) and cohesive free energies (ΔG_{OLO} - mJ/m^2). NaCl solution is 10 mM NaCl and CaCl$_2$ solution is 7mM NaCl and 1 mM CaCl$_2$.

	Surface Tensions (mJ/m^2)					Solid-Liquid Interfacial Free Energy $-\Delta G_{LS}$ (mJ/m^2)			Free Energy of Cohesion ΔG_{OLO} (mJ/m^2)
Organic	γs^+	γs^-	γs^{LW}	γs^{AB}	γs^{TOT}	DI	NaCl	CaCl$_2$	ΔG_{LOL}
ALG	0.70	21.92	33.43	7.84	41.27	110.0	106.9	109.7	-8.67
BSA	0.06	47.72	38.54	3.41	41.95	130.2	129.2	129.9	30.96
SRHA	1.72	23.51	33.78	12.70	46.48	117.6	114.5	116.5	-5.62

Table 6.5 - SAM surface tension, SAM-liquid interfacial free energies (ΔG_{SL} - mJ/m^2) and organic-membrane adhesive free energies (ΔG_{SLO}^{TOT} - mJ/m^2). NaCl solution is 10 mM NaCl and CaCl$_2$ solution is 7mM NaCl and 1 mM CaCl$_2$.

	Surface Tensions (mJ/m^2)					Solid-Liquid Interfacial Free Energy $-\Delta G_{SL}$ (mJ/m^2)			Free Energy of Adhesion ΔG_{SLO}^{TOT} (mJ/m^2)		
SAM	γs^+	γs^-	γs^{LW}	γs^{AB}	γs^{TOT}	DI	NaCl	CaCl$_2$	Alginate	BSA	SRHA
-CH$_3$	0.00	0.39	20.86	0.06	20.92	49.9	48.8	49.4	-40.75	-23.63	-34.89
-OPh	0.00	2.49	36.49	0.10	36.59	68.5	66.4	72.6	-35.99	-18.92	-31.11
-NH$_2$	0.02	24.30	42.01	1.38	43.39	108.4	107.8	111.7	-8.66	11.51	-7.02
-COOH	0.28	47.70	39.07	7.37	46.44	134.8	134.2	133.5	8.81	29.75	8.46
-CONH$_2$	0.28	36.43	42.28	6.38	48.66	126.7	123.7	126.9	0.91	20.64	1.37
-EG$_6$OH	0.51	32.71	41.19	8.15	49.35	124.7	121.9	124.9	-1.44	17.16	-0.73
-OH	0.45	44.53	44.12	8.97	53.09	136.4	131.3	136.2	6.07	25.79	5.87

Table 6.6 – Pearson product moment correlation coefficients (PMCCs) between different surface and interfacial free energy parameters and calculated mass of adsorbed organic in electrolyte solutions (NaCl = 10mM NaCl, CaCl₂ = 7 mM NaCl/1 mM CaCl₂). Variables have high negative correlation if more negative than -0.5 and a high positive correlation if greater than 0.5.

Organic Foulant	Electrolyte Solution	Interfacial Free Energy of SAMs (mJ/m^2)		
		ΔG_{SLO}^{TOT}	ΔG_{AB}	ΔG_{LW}
ALG	NaCl	-0.72	-0.74	0.78
	CaCl₂	-0.72	-0.70	0.63
BSA	NaCl	-0.11	-0.12	0.20
	CaCl₂	-0.04	-0.04	0.02
SRHA	NaCl	-0.80	-0.80	0.66
	CaCl₂	-0.37	-0.29	0.18

Figure 6.1 - Calculated adsorbed mass of SRHA on different SAMs at equilibrium.

Adsorption occurred in 10 mM NaCl (solid symbols) and 7 mM NaCl/1 mM CaCl$_2$

(open symbols).
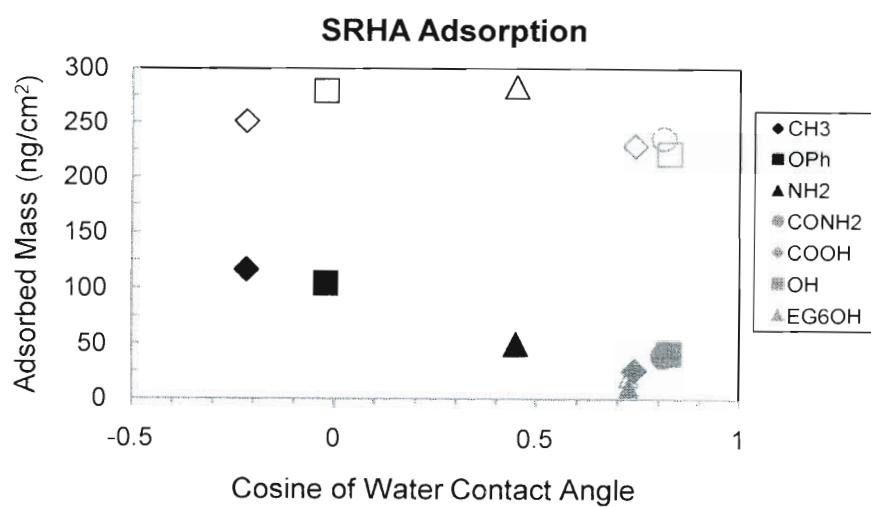
Figure 6.2 – Calculated thickness of the SRHA adsorped layers at equilibrium.

Adsorption occurred in 10 mM NaCl (solid) and 7 mM NaCl/1 mM $CaCl_2$ (stripes).
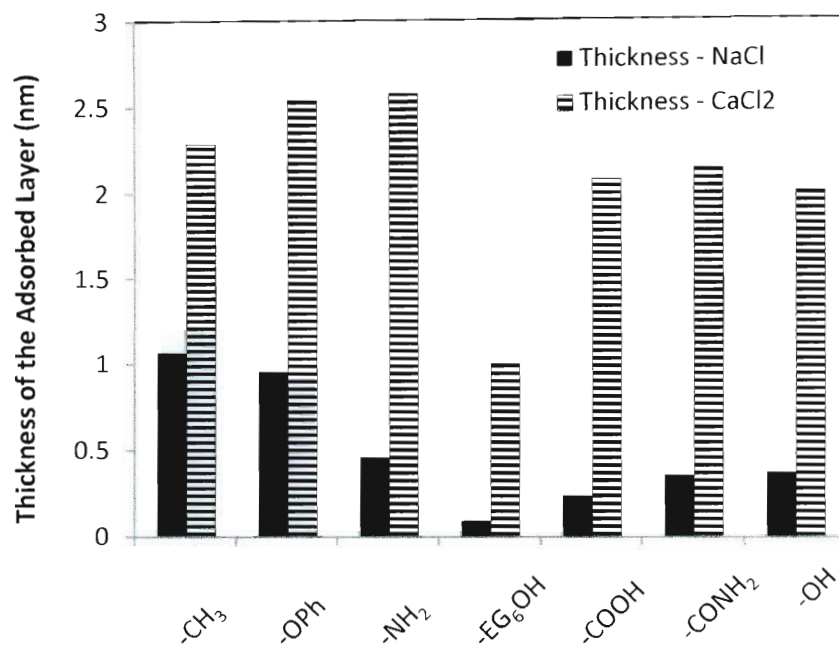
Figure 6.3 – Comparison of free energies of adhesion (ΔG_{SLO}^{TOT}), as well as the AB and LW components, of each SAM to (a) alginate, (b) BSA, and (c) SRHA.
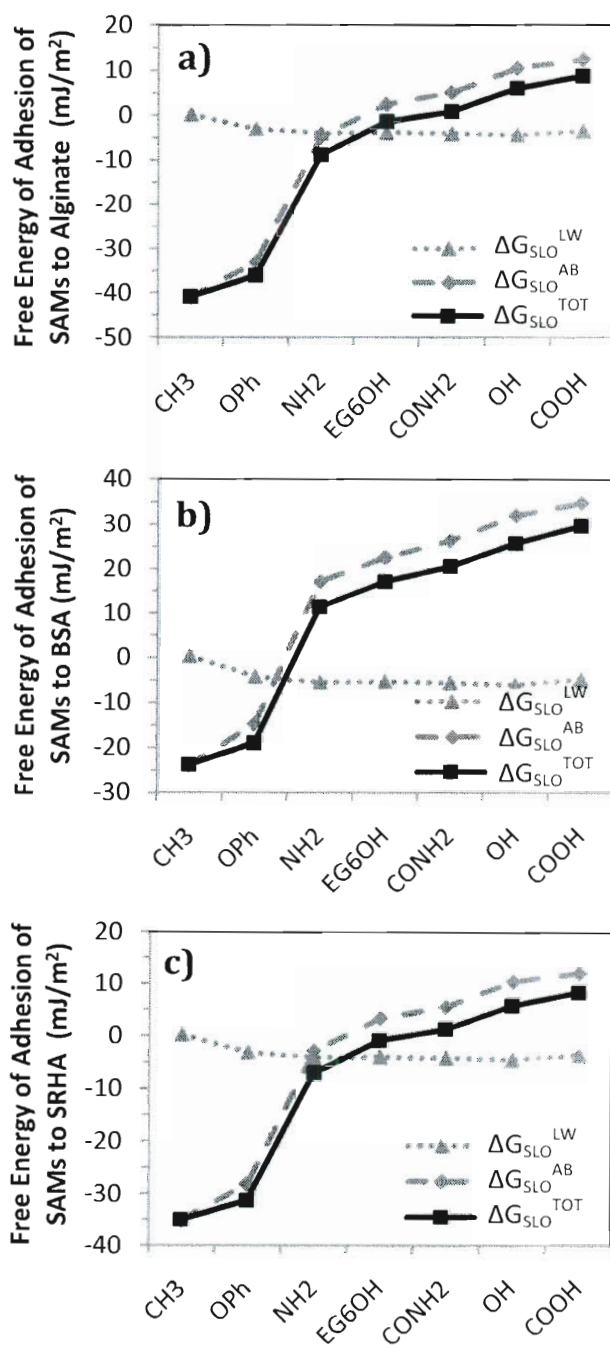
Figure 6.4 – Correlation between adsorbed organic mass and free energy of adhesion – ($\Delta G_{SLO}{}^{TOT}$) for (a)ALG, (b) BSA, and (c) SRHA. Solid markers are for solutions in 10mM NaCl. Open markers are for solutions in 7mM NaCl and 1mM CaCl$_2$.
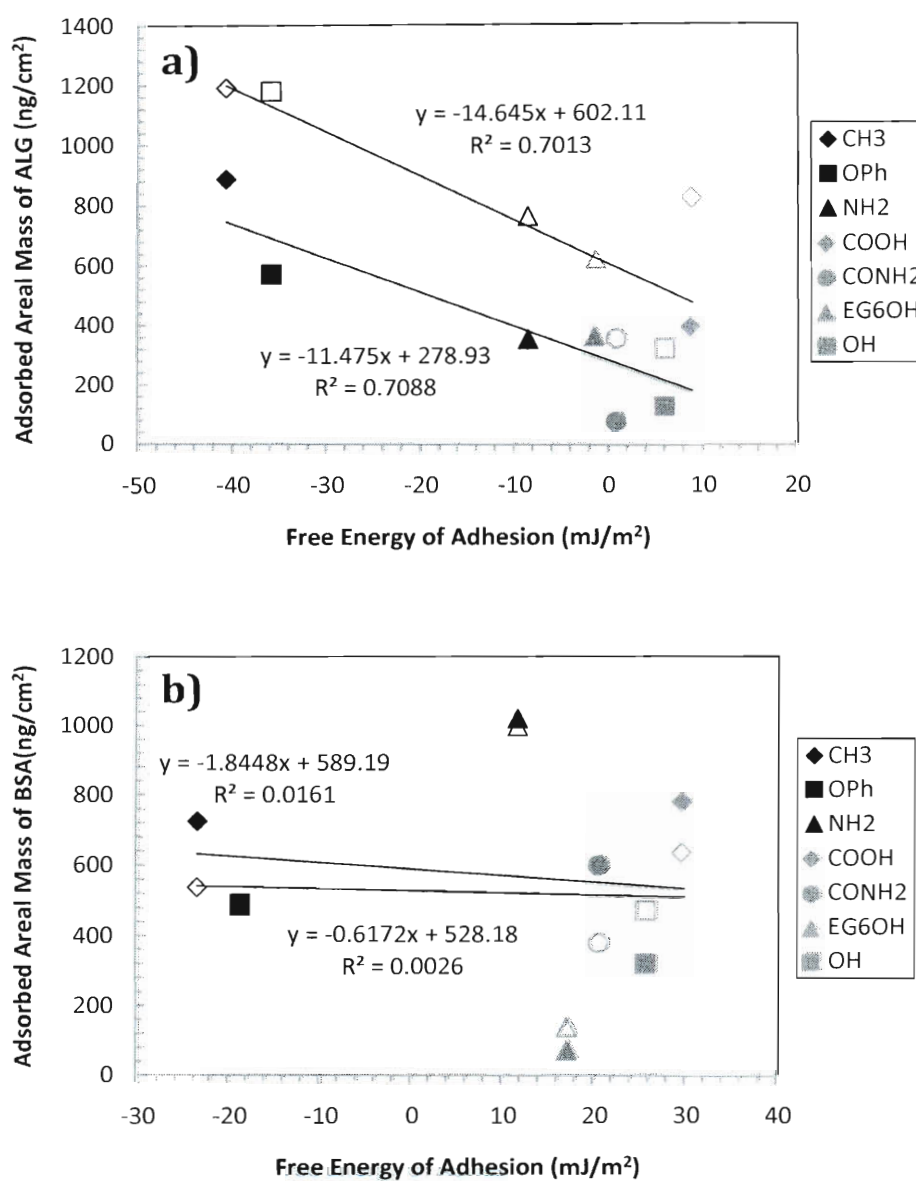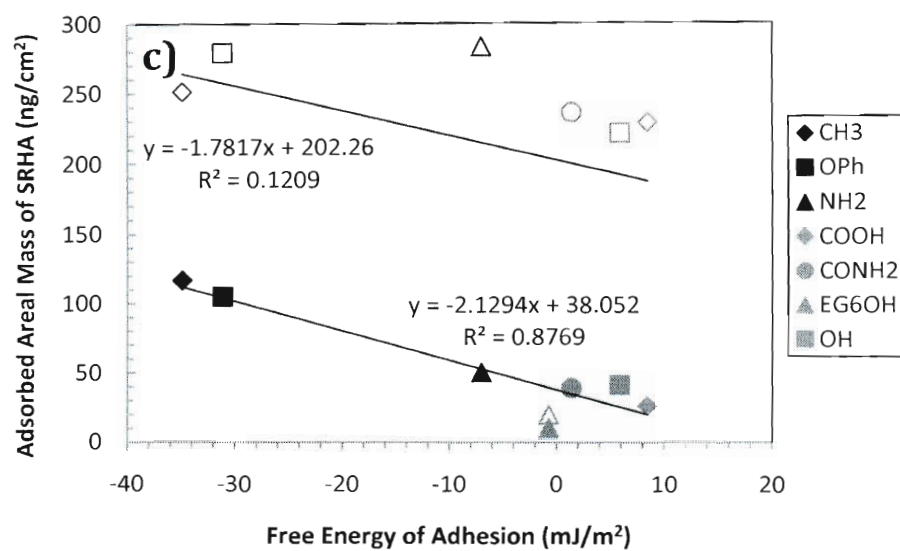
Figure 6.5 - Correlation between adsorption rate and free energy of adhesion for (a)ALG, (b) BSA, and (c) SRHA. Solid markers are for solutions in 10mM NaCl. Open markers are for solutions in 7mM NaCl and 1mM CaCl$_2$.
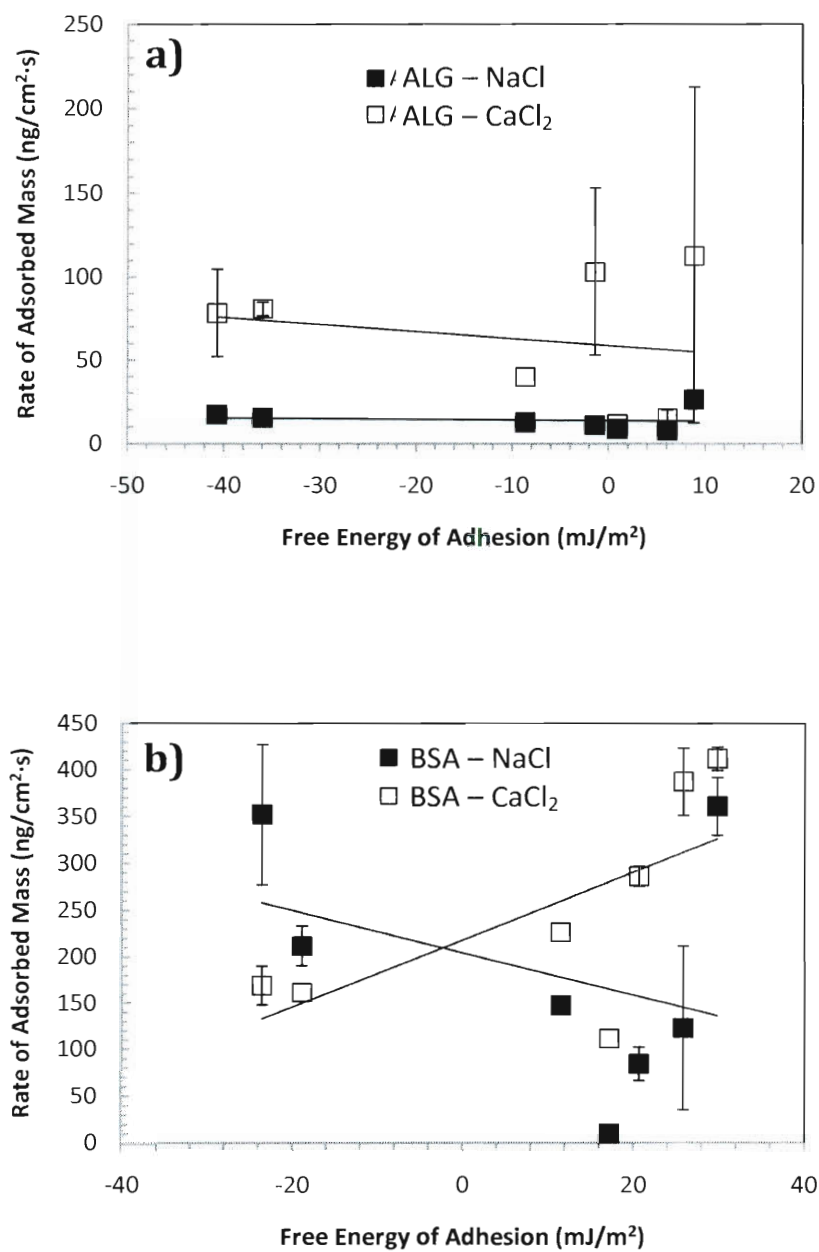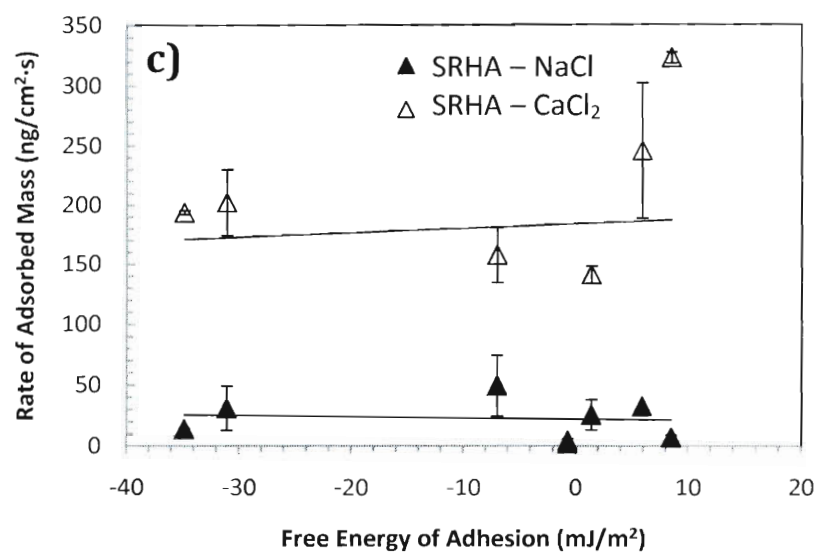
Chapter 7

Interfacial Polymerization of a Polyamide Layer on a Solid Substrate

7.1. Introduction

Membrane fouling propensity is usually directly measured through flux decline experiments at laboratory or bench-scale level. While this traditional approach to investigating membrane fouling is reasonable for a basic understanding of long term fouling of specific waters, there are several limitations to this method that prohibit a more mechanistic understanding of membrane fouling. First of all, the flux decline from bench-scale experiments may only be able to detect fouling due to cake- or gel-layer formation present only after several days of filtration. Flux decline experiments are insensitive to fouling due to foulant adsorption at the membrane surface, interactions that directly initiate subsequent membrane fouling and fouling layer formation [147]. Secondly, due to the nature of the interfacial

polymerization process, membrane chemistry and material can vary significantly over the membrane surface area. Several techniques and instruments outside of membrane filtration experiments directly have promised to be helpful for characterizing membrane adsorption, including surface plasmon resonance (SPR), atomic force microscopy (AFM), and quartz crystal microbalance with dissipation (QCM-D) [68, 88, 130, 160, 174]. However, the issue of mechanistically understanding adsorption onto heterogeneous membrane material with many imperfections still limits our ability to isolate specific variables, such as surface charge, well-characterized functionality, and surface roughness.

Being able to create of a synthetic membrane surface through interfacial polymerization at a smaller scale than membranes are typically mass produced would allow for systematic study of controlled chemical and surface modification of membranes for a more thorough understanding of the initial interactions that control membrane adsorption and fouling. In this chapter, we explore the process for creating synthetic membrane surfaces on solid substrates for eventual use with instruments such as SPR, AFM and QCM-D that would be able to quantify membrane adsorption.

7.2. Materials and Methodology.

7.2.1. Materials.

Polysulfone beads (PSf, Udel P3500) were obtained from Solvay Membranes. m-Phenylenediamine (MPD), or 1,3,benzenediamine, was obtained from Sigma-Aldrich (St. Louis, MO). Piperazine anhydrous was obtained from Fluka Analytical (Sigma-Aldrich, St. Louis, MO). Trimesoyl chloride (TMC) or 1,3,5-benzenetricarboxylic acid chloride, was obtained from Sigma-Aldrich (St. Louis, MO). n-Hexane (Fluka) and N,N-dimethylformamide (DMF) (Omnisolv, Charlotte, NC) were both used as solvents. 1.0 N NaOH (EMD Chemicals, Darmstadt, Germany) and 20% sodium dodecyl sulfate (SDS) (MP Biomedicals, LLC, Solon, Ohio) were used as stock solutions.

7.2.2. Methodology.

7.2.2.1. Polysulfone base layer.

The first layer of the synthetic membrane is a polysulfone support layer, whose porous layer will serve as a collector for the aqueous-phase amine in the subsequent interfacial polymerization step. Gold-coated silicon surfaces are prepared as described elsewhere [167]. An 8% PSf solution in N,N-dimethylformamide (DMF) was stirred and heated to 70°C to dissolve completely. The solution was then cooled for 30 min. and dropped by pipette onto gold-coated

silicon wafers to be spin coated at 2000rpm for 2 min. (Model WS-650S-6NPP/LITE, Laurell Technologies Corp., North Wales, PA). Phase inversion of the layer for pore formation occurs by immersing the layer in a solution composed of DI water, 2% DMF and 1% SDS. Layer is thoroughly rinsed with DI water to remove excess DMF and SDS, dried by spin coating for 2 min. at 2000rpm and then air dried for at least 30 min.

7.2.2.2. Preparation of thin-film composite polyamide layer.

Two types of polyamide membranes were of interest in this study: a fully aromatic, polyamide TFC and a semi-aromatic, poly(piperazineamide) TFC. In order to create these two polyamide surfaces, two diamines in aqueous phase were used: MPD and piperazine, respectively. The chemistry for the reaction is illustrated in Figure 7.1. In the interfacial polymerization process, the PSf membrane support was immersed for 4 min in either 2.0 wt% MPD or 4.0 wt% piperazine in DI water solution containing 1% SDS and 1% NaOH to allow all the PSf pores to contain the aqueous phase amine. The excess solution is then removed by spinning the immersed surface at 1500rpm for 15 sec. These semi-dried surfaces are then put in contact with 0.2 wt% TMC in hexane for 10 s to allow the interfacial polymerization reaction to take place. Excess TMC solution is then removed and the surface is dried by spinning at 3000rpm for 1min. Formed TFC layers are then dried in vacuum oven conditions (50°C) for a minimum of 3 hours to allow annealing to take place.

7.2.3. Membrane layer characterization.

All stages of the membrane layer formation were directly imaged using emission scanning electron microscopy (ESEM). Arial view images of dried membrane layers were taken with a FEI Quanta 400 ESEM FEG at 20 kV in high vacuum mode after coating with approximately 10 nm of gold (CrC-150 Sputtering System, TORR International) to observe membrane surface features, homogeneity and pore structure.

Chemical and elemental composition was verified through X-Ray Photoelectron Spectroscopy (XPS) (PHI Quantera XPS, Physical Electronics, Inc. Chanhassen, MN) and ATR-FTIR (Nicolet 6700 ATR-FTIR Infrared Microscope, Thermo Nicolet, Madison, WI) measurements. The combination of XPS and ATR-FTIR measurements provide a complimentary analysis of the membrane layers across a large length scale, since XPS is a highly surface sensitive technique with a penetration depth of 1 – 5 nm and ATR-FTIR can penetrate up to ~300 nm depending on the incident wave number.

ATR-FTIR spectra were obtained on dry membrane surfaces using Omnic 6.2 software (Thermo Electron Corporation) and an ATR element (Golden Gate Single Reflection Diamond ATR, Specac Ltd., Kent, United Kingdom). The active layer of the surface was pressed tightly against the crystal plate and the baseline background was subtracted out from the measurement. Spectra were measured

from 800 to 4000 cm^{-1} and each measurement was an average over 164 scans. At least 4 replicates were measured per sample.

XPS measurements were taken after membrane surfaces were stored in a vacuum oven (Fisher Scientific) at 50°C. Survey scans swept over 0-1100 eV electron binding energy at a resolution of 0.5eV. Relative elemental composition was determined based on intensity of the O(1s), N(1s) and C(1s) peaks centered around 532, 399, and 284.5 eV, respectively.

7.3. Results and Discussion

7.3.1. FTIR characterization.

The FTIR spectra over the range of 1800 – 800 cm^{-1} for the completed membrane TFCs and membranes with respective similar chemistries (NF90 and NF270) are shown in Figure 7.2. NF90 was previously reported to be an unmodified, fully aromatic polyamide membrane [6]. NF270 was characterized as an unmodified, semi-aromatic poly(piperazinamide) membrane [6, 175]. Also shown in Figure 7.2 is the polysulfone base layer. Because the TFC is formed on top of an existing polysulfone layer and the penetration depth of the ATR-FTIR technique is several hundred micrometers, the spectra for polysulfone is able to be detected in all samples.

Table 7.1 describes the peak assignments for the peaks associated with polysulfone, polyamide and poly(piperazinamide) layers. These latter peaks are identified in Figure 7.2 with arrows.

Peaks that describe polysulfone bonds, such as aromatic in-plane ring bend stretching vibration (~1587, 1504, and 1488 cm^{-1}), asymmetric SO$_2$ stretching vibration (1350-1280 cm^{-1}), and the C-O-C asymmetric stretching vibration of the aryl-O-aryl group (~1245 cm^{-1}), are all described in Table 7.1 and indicated in Figure 7.2a and b as the support layer of each TFC. Three other FTIR peaks have been identified as relevant peaks for fully aromatic polyamides:

1.   Amide I band (C=O stretching – dominant contributor, C-N stretching, and C-C-N deformation vibration in a secondary amide group) [176, 177]

2.   Aromatic amide (N-H deformation vibration [178] or C=C ring stretching vibration [179]

3.   Amide II band (N-H in-plane bending and N-C stretching vibration of a –CO-NH- group [176, 178]

These peaks are all present in the spectra of the polyamide TFC created by interfacial polymerization of m-phenylenediamine and trimesoyl chloride (Figure 7.2a). Spectra of semi-aromatic membranes lack the amide II band (1541 cm^{-1})and the aromatic amide peak (at 1609 cm^{-1}), but contain a amide I band that is shifted to 1630 cm^{-1} from 1661 cm^{-1}[6]. This peak is seen and indicated in Figure 7.2b. This

confirms that a sufficient poly(piperazinamide) TFC is being formed in this reaction of piperazine and trimesoyl chloride.

7.3.2. XPS characterization.

XPS results revealed that TFC membrane layers created contained oxygen, nitrogen, and carbon as dominate peaks, with additional trace amounts of sulfur and chlorine present as well. XPS has a penetration depth of about 5 nm, so trace amounts of sulfur indicate that the TFC layer is thinner than that amount in certain areas. Trace amounts of chlorine means that some of the trimesoyl chloride is left un-reacted. For simplicity, these trace amounts (less than 1%) are not included in the total atomic wt%. The relative elemental composition of C(1s), O(1s) and N(1s) was determined based on the intensity of those peaks and is shown in Table 7.2.

For a fully cross-linked polyamide formed from trimesoyl chloride and m-phenylenediamine, the molecular formula is C_6H_4ON and the O/N is therefore 1. For a fully linear polyamide, the molecular formula is $C_{15}H_{10}O_4N_2$ and the O/N is therefore 2. Corresponding carbon content for the fully cross-linked and fully linear polyamide layers are 75.0% and 71.4%. A poly(piperazinamide) layer, fully cross-linked and fully linear, would have molecular formula of C_5H_5ON and $C_{13}H_{12}O_4N_2$, respectively, and O/N ratios of 1 and 2, respectively, as well (shown in Table 7.2)[6, 8]. Corresponding carbon content for the fully cross-linked and fully linear poly(piperazinamide) layers are 71.4% and 68.4%.

According to Table 7.2, both the TFC polyamide and poly(piperazinamide) layers are nearly fully cross-linked, with O/N ratios of 1.11 and 1.04 respectively. Additionally, both the polyamide and poly(piperazinamide) layers have carbon contents (74.97 and 71.98 wt.%) that closely match theoretical values for their molecular formulas. Both TFCs formed under these conditions are fully cross-linked, which closely mimics those found in commercial membranes.

7.3.3. SEM characterization.

Directly observing the membrane layers using SEM can determine membrane surface features and membrane homogeneity. In order to prove consistent reaction conditions, we must be able to observe a continuous layer across the silicon surface. Figure 7.3 contains both close-up and more distant images of the polysulfone layer alone (a and b), the fully aromatic layer (c and d) and the semi-aromatic layer (e and f). Figure 7.3 a and b show consistent pore formation of the polysulfone base layer, which serves as the base for the other Figure 7.3 images. Images of the fully aromatic layer shows a rough layer that closely resembles SEM images of other fully aromatic membranes taken in literature [131, 180]. Previous studies have measured the roughness of the NF90 membrane, a fully aromatic membrane, at around 50 nm [180, 181]. Images of the fully aromatic layer show a surface that indicates a rough polymerization reaction occurred (Figure 7.3c and d). These features decreased in size and AFM roughness with increasing spin-off

velocity of the second step in the polymerization reaction (images for comparison not shown). NF270, the semi-aromatic membrane, is a much smoother membrane with a reported roughness on the scale of a few nanometers, between 4 – 15 nm [175, 180]. Figure 7.3e and f show a much smoother surface. The larger creases and ridges are from the drying procedure and not from polymerization reaction.

7.3.4. Application of substrate-based polyamide layers.

Originally, interfacial polymerized polyamide layers attached to gold-coated silicon substrates were created for use on Q-Sense QCM-D crystal sensors in order to directly detect changes in organic adsorption for different membrane chemistries. However, although chemically representative of commercial membranes and typical membrane chemistry, the current thickness and porosity of the created layers limits its use with the QCM-D technique, which relies on establishing a resonant frequency. The layer is able to be immersed in experimental conditions and remains attached after removal and drying, but the layer attached to the crystal sensor surface remains too porous to detect a consistent resonant frequency. It is possible that changes may be made to this protocol to make these surfaces more reliable for microbalance changes in mass and suitable for the QCM-D technique. However, creating membranes on solid substrates is shown to be a perfect method for small scale techniques interested in examining membrane chemistries or characteristics, such as XPS, SPR, or AFM. Additionally, different membrane modification

techniques can be examined without creating an entire sheet of membrane, which tends to contain numerous heterogeneities.

Table 7.1 – Peak assignment for FTIR spectra over wave number 1800-800 cm^{-1}.

Adapted from a table in [6].

Assignable to:	FTIR peaks	Peak assignments
Polysulfone	~1587, 1504, and 1488 cm^{-1}	Aromatic in-place ring bend stretching vibration[176]
	1385-1365 cm^{-1}	C-H symmetric deformation vibration of >C(CH$_3$)$_2$ [178]
	~1350-1280 cm^{-1}	Asymmetric SO$_2$ stretching vibration [176]
	~1245 cm^{-1}	C-O-C asymmetric stretching vibration of the aryl-O-aryl group [182]
	1180-1145 cm^{-1}	Symmetric SO$_2$ stretching vibration
	~830 cm^{-1}	In-phase out-of-plane hydrogen deformation of para-substituted phenyl groups [182]
Fully aromatic polyamide	1663 cm^{-1}	Amide I band (C=O stretching – dominant contributor, C-N stretching, and C-C-N deformation vibration in a secondary amide group) [176, 177]
	1609 cm^{-1}	Aromatic amide (N-H deformation vibration [178] or C=C ring stretching vibration [179]
	1541 cm^{-1}	Amide II band (N-H in-plane bending and N-C stretching vibration of a – CO-NH- group [176, 178]
Semi-aromatic poly(piperazinamide)	1630 cm^{-1}	Amide I band for poly(piperazinamide) [183]

Table 7.2 – XPS elemental composition and peak atomic wt. % for C(1s), O(1s) and N(1s). Trace amounts of Cl (1s) and S(1s) were also detected, but not included in the overall wt. %. Theoretical values calculated from [8].

	XPS Atomic Wt. %			
	C(1s)	O(1s)	N(1s)	O/N
Fully Aromatic Polyamide	74.97	12.89	11.61	1.11
Semi-Aromatic Poly(piperazinamide)	71.98	14.26	13.77	1.04
NF270	72.53	17.72	9.74	1.82
NF90	75.15	13.66	11.2	1.22
Theoretical Fully Cross-linked Values	75.0	12.5	12.5	1.0
Theoretical Fully Linear Values	71.4	19.1	9.5	2.0

Figure 7.1 – Chemistry of a) polyamide and b) poly (piperazinamide) thin-film composite layers created, from [6]. (n=1 for a fully crosslinked layer, n=0 for a fully linear layer).
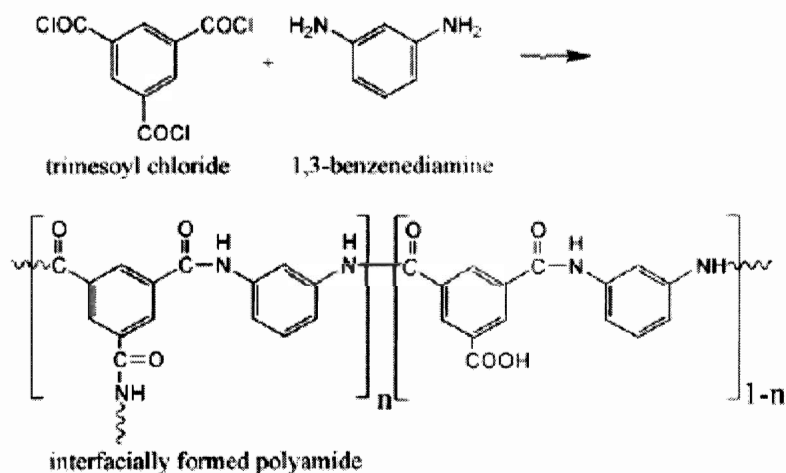
(a) Fully aromatic polyamide based on trimesoyl chloride and 1,3-benzenediamine
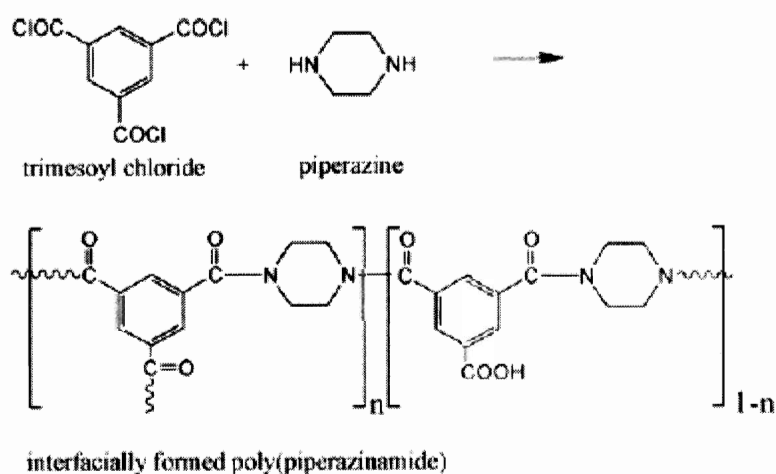
(b) Semi-aromatic polyamide based on trimesoyl chloride and piperazine

Figure 7.2 – ATR-FTIR spectra for (a) semi-aromatic TFC and NF270 membrane and (b) fully-aromatic TFC and NF90 membrane. Spectra of 8% PSf base layer is also shown. Peaks assigned to polyamide and poly(piperazinamide) bonds are indicated (black arrows), as well as polysulfone peaks (gray arrows).
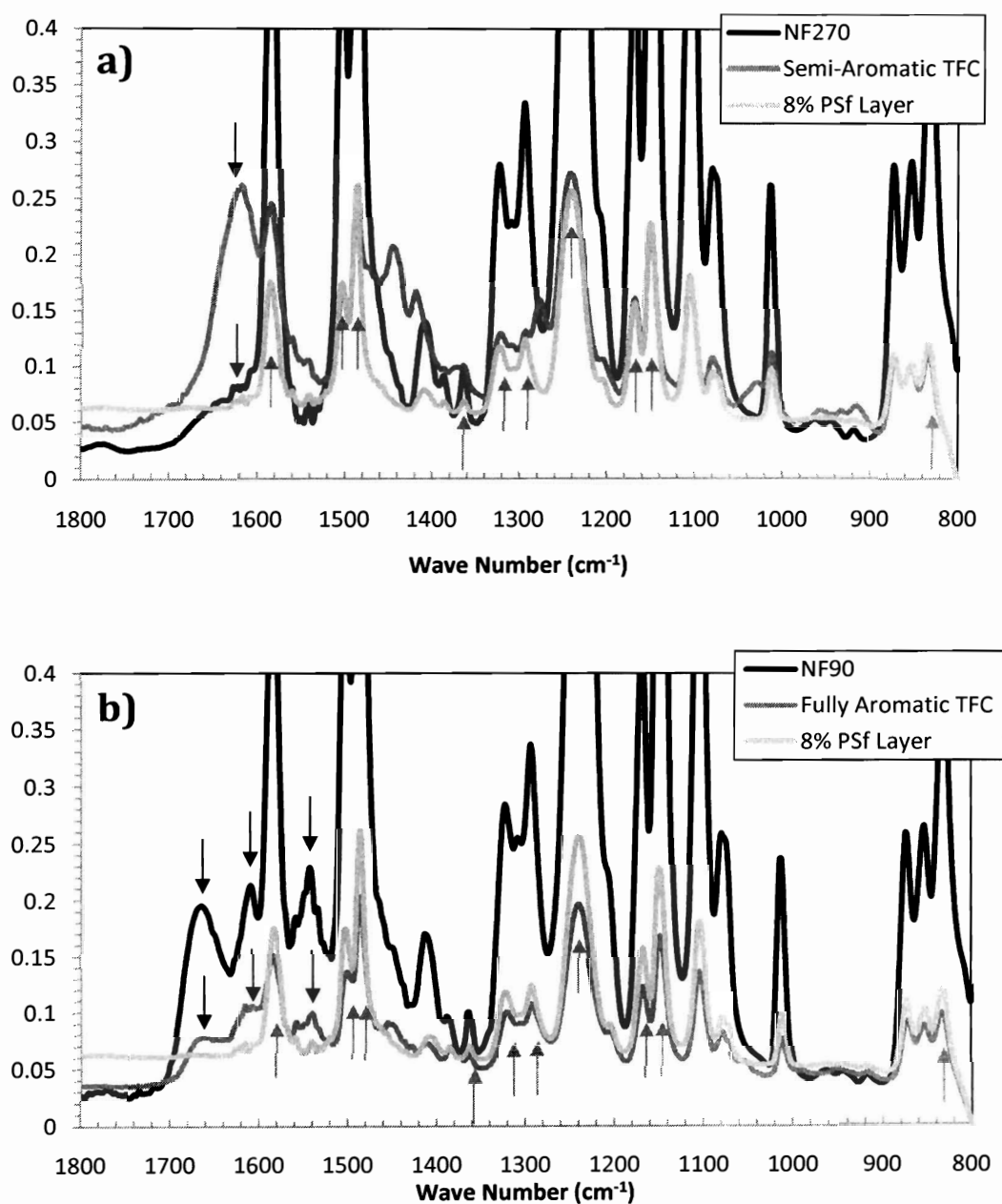
Figure 7.3 – SEM images of PSf support layer (a and b), fully aromatic polyamide (c and d), and semi-aromatic poly(piperazine)amide (e and f)
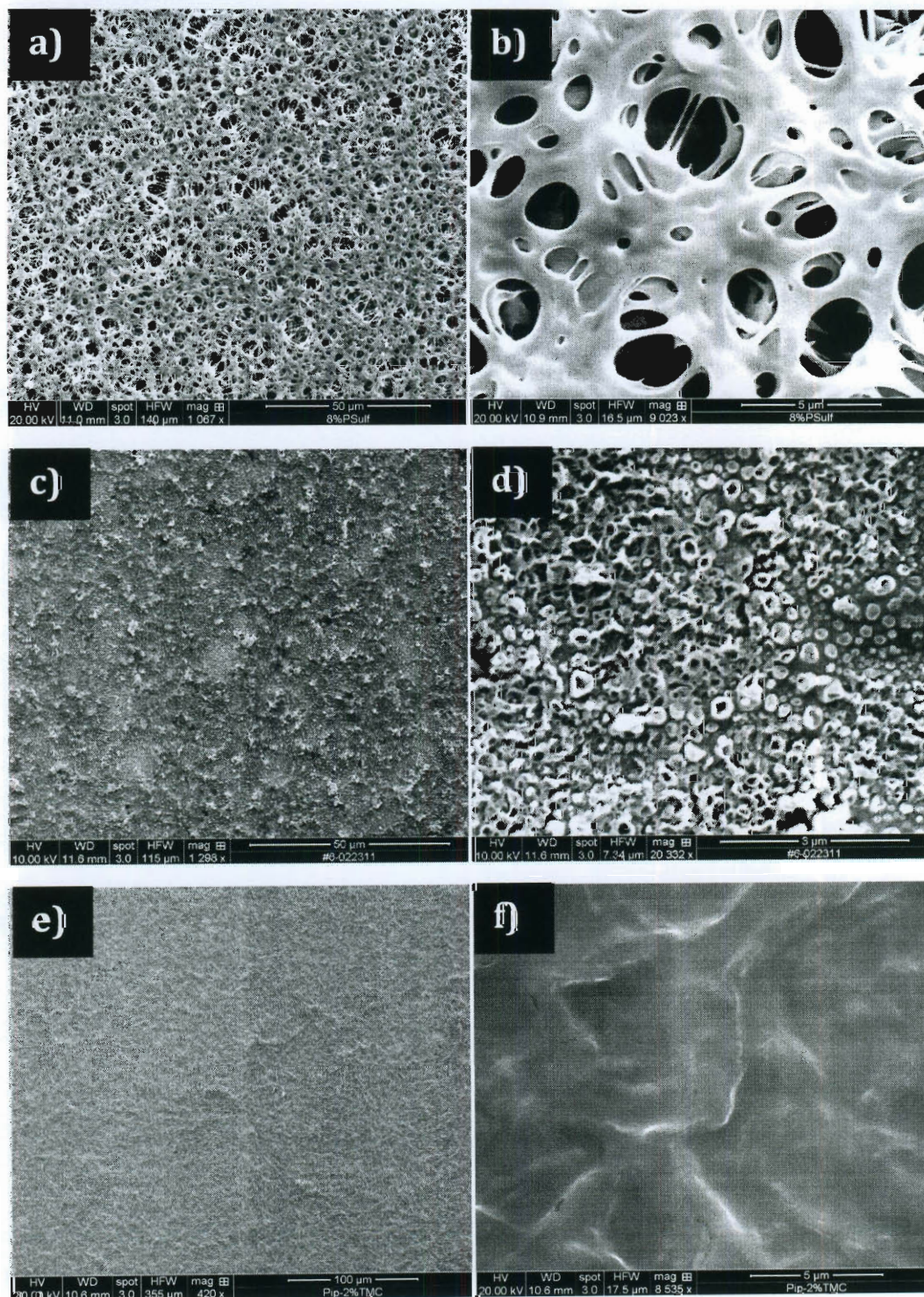
Conclusions

Membrane fouling is an inherent obstacle to the more widespread use of membrane filtration technologies. In order to develop the most robust pretreatment, fouling control strategies, and effective membrane cleaning protocols that will drive down energy costs and increase efficiency, fouling mechanisms of well-characterized yet relevant feed water solutions must be understood. The flux decline behavior of nanofiltration and reverse osmosis membrane in the presence of four model organic macromolecules and one model silica colloidal foulant was systematically investigated to examine mechanisms involved in combined fouling. All model organic foulants tested exhibited a synergistic effect when in combination with the model silica colloids during nanofiltration. The extent of the synergy, however, strongly depended on the molecular characteristics of the organic foulant. Three mechanisms: increased resistance of the mixed fouling layer, hindered back diffusion, and organic foulant adsorption were shown to have varying effects on combined fouling, depending on the specific organic foulant. The greatest synergism was observed in the presence of BSA, which adsorbs onto silica colloids as well as membrane surfaces to reduce repulsive interactions between foulants and the membrane as well as that among foulants. This resulted in aggregation of silica colloids in the fouling layer and consequently a fouling layer structure that enhances the cake enhanced osmotic pressure mechanism. The combined fouling layer structure was found to depend on membrane salt rejection. A stratified fouling layer structure was observed in filtration of the humic acid/ST-XL by a RO membrane vs.

a completely mixed structure when an NF membrane was used. The stratified structure caused lower-than-predicted flux decline by rejecting salt, which negates the effect of CEOP. Alginate formed a gel layer of significant resistance in the presence of Ca^{2+}; the presence of silica colloids during combined fouling, however, disrupts the cross-linked alginate layer to reduce fouling.

The effect of membrane surface chemistry on organic fouling and chemical cleaning was investigated using SAMs with ending functionalities found in commercial and surface modified membranes (-OPh, -NH$_2$, -CONH$_2$, -EG$_6$OH, -COOH, -OH, and –CH$_3$). Organic adsorption of alginate and humic acid was strongly correlated to water contact angle measurements of the surface while BSA adsorption did not correlate, indicating that common parameters used to characterize membrane chemistry, such as hydrophobicity, may not predict organic adsorption during membrane fouling. In order to understand specific interactions controlling organic adsorption, surface and interfacial free energies that account for van der Waals and Lewis acid-base interactions were calculated. Surface and interfacial free energy analysis revealed that acid-base interactions play a more important role than van der Waals interactions in adsorption of all three organic foulants studied. Although humic acid and alginate adsorption is well described using this thermodynamic approach, interactions determining BSA adsorption are not well captured. Dynamic adsorptive layer energy dissipation and mass data support the conclusion that adsorption onto charged (–NH$_2$ and –COOH) surfaces

are initiated by electrostatic interactions by observation of molecular reconfiguration.

This study shows evidence for the first time that specific interactions, such as hydrogen bonding and electrostatic interaction between specific functionalities, play a more important role than non-specific electrostatic and hydrophobic interactions in adsorption of and irreversible fouling by proteins. Because the initial adsorption of proteins and polysaccharides (i.e., surface conditioning) has important impacts on the subsequent formation of scales and biofilms, these results suggest that specific surface functionality may be more important than bulk surface properties, such as zeta potential and hydrophobicity, in long term fouling and cleaning of NF and RO membranes. Therefore, surface modifications of NF and RO membranes that minimize the presence –COOH and -NH$_2$ functionalities as well as other charged sites may be an effective approach to developing fouling resistant membranes. We also show for the first time that proteins, although usually found in smaller quantity on fouled membranes [165, 166], adsorb much faster to functional groups typically found on NF and RO membrane surfaces and are more difficult to remove by chemical cleaning than polysaccharides. These results suggest that proteins may play an important role in initiating bio-fouling despite their smaller quantity. Therefore, pretreatment and chemical cleaning methods should also target protein removal.

References

1.   Belfort, G., R.H. Davis, and A.L. Zydney, *The behavior of suspensions and macromolecular solutions in crossflow microfiltration.* Journal of Membrane Science, 1994. **96**(1-2): p. 1-58.

2.   Hong, S. and M. Elimelech, *Chemical and physical aspects of natural organic matter (NOM) fouling of nanofiltration membranes.* Journal of Membrane Science, 1997. **132**(2): p. 159-181.

3.   Mulder, M., *Basic Principles of Membrane Technology.* 1996, Dordrecht: Kluwer Academic Publishers.

4.   Petersen, R.J., *Composite reverse osmosis and nanofiltration membranes.* Journal of Membrane Science, 1993. **83**(1): p. 81-150.

5.   Ghosh, A.K. and E.M.V. Hoek, *Impacts of support membrane structure and chemistry on polyamide-polysulfone interfacial composite membranes.* Journal of Membrane Science, 2009. **336**(1-2): p. 140-148.

6.   Tang, C.Y., Y.-N. Kwon, and J.O. Leckie, *Effect of membrane chemistry and coating layer on physiochemical properties of thin film composite polyamide RO and NF membranes: I. FTIR and XPS characterization of polyamide and coating layer chemistry.* Desalination, 2009. **242**(1-3): p. 149-167.

7.   Ghosh, A.K., et al., *Impacts of reaction and curing conditions on polyamide composite reverse osmosis membrane properties.* Journal of Membrane Science, 2008. **311**(1-2): p. 34-45.

8.   Tang, C.Y., Y.-N. Kwon, and J.O. Leckie, *Probing the nano- and micro-scales of reverse osmosis membranes--A comprehensive characterization of physiochemical properties of uncoated and coated membranes by XPS, TEM, ATR-FTIR, and streaming potential measurements.* Journal of Membrane Science, 2007. **287**(1): p. 146-156.

9.   Tang, C.Y., Y.-N. Kwon, and J.O. Leckie, *Effect of membrane chemistry and coating layer on physiochemical properties of thin film composite polyamide RO and NF membranes: II. Membrane physiochemical properties and their dependence on polyamide and coating layers.* Desalination, 2009. **242**(1-3): p. 168-182.

10. Boussu, K., et al., *Influence of membrane and colloid characteristics on fouling of nanofiltration membranes.* Journal of Membrane Science, 2007. **289**(1-2): p. 220-230.

11. Norde, W., *Colloids and Interfaces in Life Sciences.* 2003, New York: Dekker.

12. Van der Bruggen, B., L. Braeken, and C. Vandecasteele, *Flux decline in nanofiltration due to adsorption of organic compounds.* Separation and Purification Technology, 2002. **29**(1): p. 23-31.

13. Baronti, C., et al., *Monitoring Natural and Synthetic Estrogens at Activated Sludge Sewage Treatment Plants and in a Receiving River Water.* Environ. Sci. Technol., 2000. **34**(24): p. 5059-5066.

14. Kimura, K., et al., *Adsorption of hydrophobic compounds onto NF/RO membranes: an artifact leading to overestimation of rejection.* Journal of Membrane Science, 2003. **221**(1-2): p. 89-101.

15. Lee, S. and C.-H. Lee, *Effect of operating conditions on CaSO4 scale formation mechanism in nanofiltration for water softening.* Water Research, 2000. **34**(15): p. 3854-3866.

16. Vrouwenvelder, H.S., et al., *Biofouling of membranes for drinking water production.* Desalination, 1998. **118**(1-3): p. 157-166.

17. Chellam, S. and M.R. Wiesner, *Evaluation of crossflow filtration models based on shear-induced diffusion and particle adhesion: Complications induced by feed suspension polydispersivity.* Journal of Membrane Science, 1998. **138**(1): p. 83-97.

18. Seidel, A. and M. Elimelech, *Coupling between chemical and physical interactions in natural organic matter (NOM) fouling of nanofiltration membranes: implications for fouling control.* Journal of Membrane Science, 2002. **203**(1-2): p. 245-255.

19. Mänttäri, M., et al., *Fouling effects of polysaccharides and humic acid in nanofiltration.* Journal of Membrane Science, 2000. **165**(1): p. 1-17.

20. Peng, W., I.C. Escobar, and D.B. White, *Effects of water chemistries and properties of membrane on the performance and fouling--a model development study.* Journal of Membrane Science, 2004. **238**(1-2): p. 33-46.

21.   Boussu, K., C. Vandecasteele, and B. Van der Bruggen, *Relation between membrane characteristics and performance in nanofiltration.* Journal of Membrane Science, 2008. **310**(1-2): p. 51-65.

22.   Elimelech, M., et al., *Role of membrane surface morphology in colloidal fouling of cellulose acetate and composite aromatic polyamide reverse osmosis membranes.* Journal of Membrane Science, 1997. **127**(1): p. 101-109.

23.   Hoek, E.M.V., S. Bhattacharjee, and M. Elimelech, *Effect of membrane surface roughness on colloid-membrane DLVO interactions.* Langmuir, 2003. **19**(11): p. 4836-4847.

24.   Vrijenhoek, E., S. Hong, and M. Elimelech, *Influence of membrane surface properties on initial rate of colloidal fouling of reverse osmosis and nanofiltration membranes* Journal of Membrane Science, 2001. **188**(1): p. 115-128.

25.   Riedl, K., B. Girard, and R.W. Lencki, *Influence of membrane structure on fouling layer morphology during apple juice clarification.* Journal of Membrane Science, 1998. **139**(2): p. 155-166.

26.   Tang, C.Y., Y.-N. Kwon, and J.O. Leckie, *Fouling of reverse osmosis and nanofiltration membranes by humic acid--Effects of solution composition and hydrodynamic conditions.* Journal of Membrane Science, 2007. **290**(1-2): p. 86-94.

27.   Mo, H., K.G. Tay, and H.Y. Ng, *Fouling of reverse osmosis membrane by protein (BSA): Effects of pH, calcium, magnesium, ionic strength and temperature.* Journal of Membrane Science, 2008. **315**(1-2): p. 28-35.

28.   Lee, S., J.W. Cho, and M. Elimelech, *Combined influence of natural organic matter (NOM) and colloidal particles on nanofiltration membrane fouling.* Journal of Membrane Science, 2005. **262**(1-2): p. 27-41.

29.   Li, Q.L. and M. Elimelech, *Organic fouling and chemical cleaning of nanofiltration membranes: Measurements and mechanisms.* Environmental Science & Technology, 2004. **38**(17): p. 4683-4693.

30.   Rodgers, J.L. and W.A. Nicewander, *Thirteen Ways to Look at the Correlation Coefficient.* The American Statistician, 1988. **42**(1): p. 59-66.

31. Chen, J.C., M. Elimelech, and A.S. Kim, *Monte Carlo simulation of colloidal membrane filtration: Model development with application to characterization of colloid phase transition.* Journal of Membrane Science, 2005. **255**(1-2): p. 291-305.

32. Song, L. and E. Menachem, *Theory of concentration polarization in crossflow filtration.* J. Chem. Soc., Faraday Trans., 1995. **91**(19): p. 3389-3398.

33. P. Bacchin, P.A.V.S., *Model for colloidal fouling of membranes.* AIChE Journal, 1995. **41**(2): p. 368-376.

34. Stamatakis, K. and C. Tien, *A simple model of cross-flow filtration based on particle adhesion.* AIChE Journal, 1993. **39**(8): p. 1292-1302.

35. Carman, P.C., *Fundamental principles of industrial filtration.* Trans. Inst. Chem. Eng., 1938. **16**: p. 168-187.

36. Happel, J., *Viscous flow in multiparticle systems: Slow motion of fluids relative to beds of spherical particles.* AIChE Journal, 1958. **4**(2): p. 197-201.

37. Kilduff, J.E., et al., *Modeling Flux Decline during Nanofiltration of NOM with Poly(arylsulfone) Membranes Modified Using UV-Assisted Graft Polymerization.* Environmental Engineering Science, 2002. **19**(6): p. 477 - 495.

38. Ho, C.-C. and A.L. Zydney, *A Combined Pore Blockage and Cake Filtration Model for Protein Fouling during Microfiltration.* Journal of Colloid and Interface Science, 2000. **232**(2): p. 389-399.

39. Park, C., et al., *Effect of cake layer structure on colloidal fouling in reverse osmosis membranes.* Desalination, 2008. **220**(1-3): p. 335-344.

40. Kim, A.S., et al., *Fundamental Mechanisms of Three-Component Combined Fouling with Experimental Verification.* Langmuir. **0**(0).

41. Foley, G., D.M. Malone, and F. MacLoughlin, *Modeling the effects of particle polydispersity in crossflow filtration.* Journal of Membrane Science, 1995. **99**(1): p. 77-88.

42. Potts, D.E., R.C. Ahlert, and S.S. Wang, *A critical review of fouling of reverse osmosis membranes.* Desalination, 1981. **36**(3): p. 235-264.

43. Dharmappa, H.B., et al., *A comprehensive model for cross-flow filtration incorporating polydispersity of the influent.* Journal of Membrane Science, 1992. **65**(1-2): p. 173-185.

44. Hoek, E.M.V., A.S. Kim, and M. Elimelech, *Influence of crossflow membrane filter geometry and shear rate on colloidal fouling in reverse osmosis and nanofiltration separations.* Environmental Engineering Science, 2002. **19**(6): p. 357-372.

45. Hoek, E.M.V. and M. Elimelech, *Cake-enhanced concentration polarization: A new fouling mechanism for salt-rejecting membranes.* Environmental Science & Technology, 2003. **37**(24): p. 5581-5588.

46. Li, Q.L. and M. Elimelech, *Synergistic effects in combined fouling of a loose nanofiltration membrane by colloidal materials and natural organic matter.* Journal of Membrane Science, 2006. **278**(1-2): p. 72-82.

47. Kim, A.S. and A.N.L. Ng, *Hydraulic permeability of polydispersed cake layers: an analytic approach.* Desalination, 2007. **207**(1-3): p. 144-152.

48. Baruah, G.L. and G. Belfort, *A Predictive Aggregate Transport Model for Microfiltration of Combined Macromolecular Solutions and Poly-Disperse Suspensions: Model Development.* Biotechnol. Prog., 2003. **19**: p. 1524-1532.

49. Ke Ming Hsieh, G.A.M.L.W.L.M.L.S., *Interactions of microbial biofilms with toxic trace metals: 1. Observation and modeling of cell growth, attachment, and production of extracellular polymer.* Biotechnology and Bioengineering, 1994. **44**(2): p. 219-231.

50. Reichert, U., et al., *Visualising protein adsorption to ion-exchange membranes by confocal microscopy.* Journal of Membrane Science, 2002. **199**(1-2): p. 161-166.

51. Satulovsky, J., M.A. Carignano, and I. Szleifer, *Kinetic and thermodynamic control of protein adsorption.* Proceedings of the National Academy of Sciences of the United States of America, 2000. **97**(16): p. 9037-9041.

52. Roach, L.S., H. Song, and R.F. Ismagilov, *Controlling Nonspecific Protein Adsorption in a Plug-Based Microfluidic System by Controlling Interfacial Chemistry Using Fluorous-Phase Surfactants.* Analytical Chemistry, 2004. **77**(3): p. 785-796.

53. Gomes, A.C., I.C. Gonçalves, and M.N.d. Pinho, *The role of adsorption on nanofiltration of azo dyes.* Journal of Membrane Science, 2005. **255**(1-2): p. 157-165.

54. Elwing, H., et al., *A wettability gradient method for studies of macromolecular interactions at the liquid/solid interface.* Journal of Colloid and Interface Science, 1987. **119**(1): p. 203-210.

55. Gourley, L., et al., *Characterization of adsorptive fouling on ultrafiltration membranes by peptides mixtures using contact angle measurements.* Journal of Membrane Science, 1994. **97**: p. 283-289.

56. Roudman, A.R. and F.A. DiGiano, *Surface energy of experimental and commercial nanofiltration membranes: effects of wetting and natural organic matter fouling.* Journal of Membrane Science, 2000. **175**(1): p. 61-73.

57. Bowen, W.R., T.A. Doneva, and J.A.G. Stoton, *Protein deposition during cross-flow membrane filtration: AFM studies and flux loss.* Colloids and Surfaces B: Biointerfaces, 2003. **27**(2-3): p. 103-113.

58. Fraaije, J.G.E.M., et al., *Interfacial thermodynamics of protein adsorption, ion co-adsorption and ion binding in solution : I. Phenomenological linkage relations for ion exchange in lysozyme chromatography and titration in solution.* Biophysical Chemistry, 1991. **40**(3): p. 303-315.

59. Norde, W., *The behavior of proteins at interfaces, with special attention to the role of the structure stability of the protein molecule.* Clinical Materials, 1992. **11**(1-4): p. 85-91.

60. Norde, W. and A.C.I. Anusiem, *Adsorption, desorption and re-adsorption of proteins on solid surfaces.* Colloids and Surfaces, 1992. **66**(1): p. 73-80.

61. Norde, W. and J. Lyklema, *Protein adsorption and bacterial adhesion to solid surfaces: A colloid-chemical approach.* Colloids and Surfaces, 1989. **38**(1): p. 1-13.

62. Norde, W. and J. Lyklema, *The adsorption of human plasma albumin and bovine pancreas ribonuclease at negatively charged polystyrene surfaces : I. Adsorption isotherms. Effects of charge, ionic strength, and temperature.* Journal of Colloid and Interface Science, 1978. **66**(2): p. 257-265.

63. Van Dulm, P. and W. Norde, *The adsorption of human plasma albumin on solid surfaces, with special attention to the kinetic aspects.* Journal of Colloid and Interface Science, 1983. **91**(1): p. 248-255.

64. Van Dulm, P., W. Norde, and J. Lyklema, *Ion participation in protein adsorption at solid surfaces.* Journal of Colloid and Interface Science, 1981. **82**(1): p. 77-82.

65. Lee, S.H. and E. Ruckenstein, *Adsorption of proteins onto polymeric surfaces of different hydrophilicities--a case study with bovine serum albumin.* Journal of Colloid and Interface Science, 1988. **125**(2): p. 365-379.

66. Norde, W., et al., *Protein adsorption at solid-liquid interfaces: Reversibility and conformation aspects.* Journal of Colloid and Interface Science, 1986. **112**(2): p. 447-456.

67. Cosgrove, T., T.M. Obey, and B. Vincent, *The configuration of sodium poly(styrene sulfonate) at polystyrene/solution interfaces.* Journal of Colloid and Interface Science, 1986. **111**(2): p. 409-418.

68. Sethuraman, A., et al., *Effect of Surface Wettability on the Adhesion of Proteins.* Langmuir, 2004. **20**(18): p. 7779-7788.

69. Jönsson, U., I. Lundström, and I. Rönnberg, *Immunoglobulin G and secretory fibronectin adsorption to silica : The influence of conformational changes on the surface.* Journal of Colloid and Interface Science, 1987. **117**(1): p. 127-138.

70. Shirahama, H. and T. Suzawa, *Adsorption of bovine serum albumin onto styrene/2-hydroxyethyl methacrylate copolymer latex.* Journal of Colloid and Interface Science, 1985. **104**(2): p. 416-421.

71. Kim, S. and E.M.V. Hoek, *Interactions controlling biopolymer fouling of reverse osmosis membranes.* Desalination, 2007. **202**(1-3): p. 333-342.

72. Pontié, M., et al., *The streaming potential method for the characterization of ultrafiltration organic membranes and the control of cleaning treatments.* Journal of Membrane Science, 1997. **129**(1): p. 125-133.

73. Derjaguin, B.V. and L. Landau, *Theory of the stability of strongly charged lyophobic sols and of the adhesion of strongly charged particles in solutions of electrolytes.* Acta Physicohim. (URSS), 1941. **14**: p. 633-662.

74.   Verwey, E.J. and J.T.G. Overbeek, *Theory of the stability of lyophobic colloids.* 1948, Elsevier: Amsterdam.

75.   Bhattacharjee, S., A. Sharma, and P.K. Bhattacharya, *Estimation and Influence of Long Range Solute. Membrane Interactions in Ultrafiltration.* Industrial & Engineering Chemistry Research, 1996. **35**(9): p. 3108-3121.

76.   Bhattacharjee, S., C.-H. Ko, and M. Elimelech, *DLVO Interaction between Rough Surfaces.* Langmuir, 1998. **14**(12): p. 3365-3375.

77.   Yotsumoto, H. and R.-H. Yoon, *Application of Extended DLVO Theory: I. Stability of Rutile Suspensions.* Journal of Colloid and Interface Science, 1993. **157**(2): p. 426-433.

78.   van Oss, C.J., *Acid--base interfacial interactions in aqueous media.* Colloids and Surfaces A: Physicochemical and Engineering Aspects, 1993. **78**: p. 1-49.

79.   Brant, J.A. and A.E. Childress, *Assessing short-range membrane-colloid interactions using surface energetics.* Journal of Membrane Science, 2002. **203**(1-2): p. 257-273.

80.   Lee, S., et al., *Natural organic matter fouling due to foulant-membrane physicochemical interactions.* Desalination, 2007. **202**(1-3): p. 377-384.

81.   Hook, F., et al., *Variations in Coupled Water, Viscoelastic Properties, and Film Thickness of a Mefp-1 Protein Film during Adsorption and Cross-Linking: A Quartz Crystal Microbalance with Dissipation Monitoring, Ellipsometry, and Surface Plasmon Resonance Study.* Analytical Chemistry, 2001. **73**(24): p. 5796-5804.

82.   Welin-Klintström, S., A. Askendal, and H. Elwing, *Surfactant and Protein Interactions on Wettability Gradient Surfaces.* Journal of Colloid and Interface Science, 1993. **158**(1): p. 188-194.

83.   Sigal, G.B., M. Mrksich, and G.M. Whitesides, *Effect of Surface Wettability on the Adsorption of Proteins and Detergents.* Journal of the American Chemical Society, 1998. **120**(14): p. 3464-3473.

84.   Chapman, R.G., et al., *Polymeric Thin Films That Resist the Adsorption of Proteins and the Adhesion of Bacteria.* Langmuir, 2001. **17**(4): p. 1225-1233.

85. Mrksich, M., G.B. Sigal, and G.M. Whitesides, *Surface Plasmon Resonance Permits in Situ Measurement of Protein Adsorption on Self-Assembled Monolayers of Alkanethiolates on Gold.* Langmuir, 1995. **11**(11): p. 4383-4385.

86. Chapman, R.G., et al., *Surveying for Surfaces that Resist the Adsorption of Proteins.* Journal of the American Chemical Society, 2000. **122**(34): p. 8303-8304.

87. Lee, S. and M. Elimelech, *Relating organic fouling of reverse osmosis membranes to intermolecular adhesion forces.* Environmental Science & Technology, 2006. **40**(3): p. 980-987.

88. Liu, S.X. and J.-T. Kim, *Study of adsorption kinetics of surfactants onto polyethersulfone membrane surface using QCM-D.* Desalination, 2009. **247**(1-3): p. 355-361.

89. Munro, J.C. and C.W. Frank, *Polyacrylamide Adsorption from Aqueous Solutions on Gold and Silver Surfaces Monitored by the Quartz Crystal Microbalance.* Macromolecules, 2004. **37**(3): p. 925-938.

90. Vogt, B.D., et al., *Moisture absorption into ultrathin hydrophilic polymer films on different substrate surfaces.* Polymer, 2005. **46**(5): p. 1635-1642.

91. Bandey, H.L., et al., *Viscoelastic characterization of electroactive polymer films at the electrode/solution interface.* Faraday Discussion, 1997. **107**(1): p. 105-121.

92. Voinova, M.V. and et al., *Viscoelastic Acoustic Response of Layered Polymer Films at Fluid-Solid Interfaces: Continuum Mechanics Approach.* Physica Scripta, 1999. **59**(5): p. 391.

93. Diethelm, J., *Viscoelastic analysis of organic thin films on quartz resonators.* Macromolecular Chemistry and Physics, 1999. **200**(3): p. 501-516.

94. Prime, K.L., Whitesides, George M. , *Self-Assembled Organic Monolayers: Model Systems for Studying Adsorption of Proteins at Surfaces.* Science, 1991. **252**(5009): p. 1164-1166.

95. Bertilsson, L. and B. Liedberg, *Infrared study of thiol monolayer assemblies on gold: preparation, characterization, and functionalization of mixed monolayers.* Langmuir, 1993. **9**(1): p. 141-149.

96. Prime, K.L. and G.M. Whitesides, *Adsorption of proteins onto surfaces containing end-attached oligo(ethylene oxide): a model system using self-assembled monolayers.* Journal of the American Chemical Society, 1993. **115**(23): p. 10714-10721.

97. Roach, P., D. Farrar, and C.C. Perry, *Interpretation of Protein Adsorption: Surface-Induced Conformational Changes.* Journal of the American Chemical Society, 2005. **127**(22): p. 8168-8173.

98. Griffin, V.L., *Protein Adsorption on Tailored Oligo(ethylene glycol) Surfaces*, in *Chemical Engineering.* 2006, Rice University: Houston. p. 97.

99. Katsoufidou, K., S.G. Yiantsios, and A.J. Karabelas, *Experimental study of ultrafiltration membrane fouling by sodium alginate and flux recovery by backwashing.* Journal of Membrane Science, 2007. **300**(1-2): p. 137-146.

100. Sayed Razavi, S.K., J.L. Harris, and F. Sherkat, *Fouling and cleaning of membranes in the ultrafiltration of the aqueous extract of soy flour.* Journal of Membrane Science, 1996. **114**(1): p. 93-104.

101. Muñoz-Aguado, M.J., D.E. Wiley, and A.G. Fane, *Enzymatic and detergent cleaning of a polysulfone ultrafiltration membrane fouled with BSA and whey.* Journal of Membrane Science, 1996. **117**(1-2): p. 175-187.

102. Koyuncu, I., A. Lüttge, and M.R. Wiesner, *Interferometric observations and kinetic modeling of the chemical cleaning of humic materials deposited on membranes.* Journal of Membrane Science, 2008. **313**(1-2): p. 127-134.

103. Bartlett, M., M.R. Bird, and J.A. Howell, *An experimental study for the development of a qualitative membrane cleaning model.* Journal of Membrane Science, 1995. **105**(1-2): p. 147-157.

104. Ang, W.S., S. Lee, and M. Elimelech, *Chemical and physical aspects of cleaning of organic-fouled reverse osmosis membranes.* Journal of Membrane Science, 2006. **272**(1-2): p. 198-210.

105. Liikanen, R., J. Yli-Kuivila, and R. Laukkanen, *Efficiency of various chemical cleanings for nanofiltration membrane fouled by conventionally-treated surface water.* Journal of Membrane Science, 2002. **195**(2): p. 265-276.

106. Zondervan, E. and B. Roffel, *Evaluation of different cleaning agents used for cleaning ultra filtration membranes fouled by surface water.* Journal of Membrane Science, 2007. **304**(1-2): p. 40-49.

107. Arkhangelsky, E., D. Kuzmenko, and V. Gitis, *Impact of chemical cleaning on properties and functioning of polyethersulfone membranes.* Journal of Membrane Science, 2007. **305**(1-2): p. 176-184.

108. Bae, T.H., I.C. Kim, and T.M. Tak, *Preparation and characterization of fouling-resistant TiO2 self-assembled nanocomposite membranes.* Journal of Membrane Science, 2006. **275**(1-2): p. 1-5.

109. Kilduff, J.E., et al., *Photochemical modification of poly(ether sulfone) and sulfonated poly(sulfone) nanofiltration membranes for control of fouling by natural organic matter.* Desalination, 2000. **132**(1-3): p. 133-142.

110. Kim, I.C., et al., *Preparation of Fouling Resistant Nanofiltration and Reverse Osmosis Membranes and Their Use for Dyeing Wastewater Effluent.* Journal of Industrial & Engineering Chemistry, 2004. **10**(1): p. 115-121.

111. Baggott, S.R. and A. Jaffer, *The application of a novel chemical treatment program to mitigate scaling and fouling in reverse osmosis units.* Desalination, 1991. **83**(1-3): p. 119-119.

112. Leiknes, T., H. Ødegaard, and H. Myklebust, *Removal of natural organic matter (NOM) in drinking water treatment by coagulation-microfiltration using metal membranes.* Journal of Membrane Science, 2004. **242**(1-2): p. 47-55.

113. Ning, R.Y., T.L. Troyer, and R.S. Tominello, *Chemical control of colloidal fouling of reverse osmosis systems.* Desalination, 2005. **172**(1): p. 1-6.

114. Song, W., et al., *Nanofiltration of natural organic matter with H2O2/UV pretreatment: fouling mitigation and membrane surface characterization.* Journal of Membrane Science, 2004. **241**(1): p. 143-160.

115. Schäfer, A.I., et al., *Microfiltration of colloids and natural organic matter.* Journal of Membrane Science, 2000. **171**(2): p. 151-172.

116. Tarabara, V.V., et al., *Morphology of Deposits Formed from Chemically Heterogeneous Suspensions: Application to Membrane Filtration.* Journal of Colloid and Interface Science, 2002. **256**(2): p. 367-377.

117. Kim, A.S.L., Yuewei *Irreversible Chemical Potential and Shear-Induced Diffusion in Crossflow Filtration.* Industrial Engineering and Chemistry Research, 2008. **In press**.

118. Amirbahman, A. and T.M. Olson, *Transport of humic matter-coated hematite in packed beds.* Environ. Sci. Technol., 1993. **27**(13): p. 2807-2813.

119. Kretzschmar, R. and H. Sticher, *Transport of Humic-Coated Iron Oxide Colloids in a Sandy Soil: Influence of Ca2+ and Trace Metals.* Environ. Sci. Technol., 1997. **31**(12): p. 3497-3504.

120. Akbour, R.A., J. Douch, M. Hamdani, and P. Schmitz, *Transport of Kaolinite Colloids through Quartz Sand: Influence of Humic Acid, Ca2+, and Trace Metals* Journal of Colloid and Interface Science, 2002. **253**(1): p. 1-8.

121. Chen, K.L. and M. Elimelech, *Influence of humic acid on the aggregation kinetics of fullerene (C60) nanoparticles in monovalent and divalent electrolyte solutions.* Journal of Colloid and Interface Science, 2007. **309**(1): p. 126-134.

122. Bellona, C. and J.E. Drewes, *The role of membrane surface charge and solute physico-chemical properties in the rejection of organic acids by NF membranes.* Journal of Membrane Science, 2005. **249**(1-2): p. 227-234.

123. Childress, A.E. and M. Elimelech, *Effect of solution chemistry on the surface charge of polymeric reverse osmosis and nanofiltration membranes.* Journal of Membrane Science, 1996. **119**(2): p. 253-268.

124. Barker, D.J. and D.C. Stuckey, *A review of soluble microbial products (SMP) in wastewater treatment systems.* Water Research, 1999. **33**(14): p. 3063-3082.

125. Jarusutthirak, C., G. Amy, and J.-P. Croué, *Fouling characteristics of wastewater effluent organic matter (EfOM) isolates on NF and UF membranes.* Desalination, 2002. **145**(1-3): p. 247-255.

126. Jarusutthirak, C. and G. Amy, *Understanding soluble microbial products (SMP) as a component of effluent organic matter (EfOM).* Water Research, 2007. **41**(12): p. 2787-2793.

127. Howe, K.J. and M.M. Clark, *Fouling of Microfiltration and Ultrafiltration Membranes by Natural Waters.* Environ. Sci. Technol., 2002. **36**(16): p. 3571-3576.

128. Levine, A.D., G. Tchobanoglous, and T. Asano, *Characterization of the size distribution of contaminants in waste-water-treatment and reuse implications.* J. Water Polut. Control Fed., 1985. **57**: p. 805.

129. Leppard, G.G., D. Mavrocaordatos, and D. Perret, *Electron-optical characterization of nano- and micro-particles in raw and treated waters: an overview.* Water Science Technology, 2004. **50**: p. 1.

130. Höök, F., *Development of a noval QCM technique for protein adsorption studies,* in *Department of Biochemistry and Biophysics and Department of Applied Physics.* 1997, Chalmers University of Technology, Götebory University: Göteborg, Sweden. p. 60.

131. Li, Q., Z. Xu, and I. Pinnau, *Fouling of reverse osmosis membranes by biopolymers in wastewater secondary effluent: Role of membrane surface properties and initial permeate flux.* Journal of Membrane Science, 2007. **290**(1-2): p. 173-181.

132. Sauerbrey, G., *Verwendung von Schwingquarzen zur Wagung diinner Schicten und zur Mikrowagung.* Z. Phys., 1959. **155**(1): p. 206-222.

133. Song, L., et al., *Performance limitation of the full-scale reverse osmosis process.* Journal of Membrane Science, 2003. **214**(2): p. 239-244.

134. Kilduff, J.E., et al., *Kinetics of Membrane Flux Decline: The Role of Natural Colloids and Mitigation via Membrane Surface Modification.* Journal of Nanoparticle Research, 2005. **7**(4): p. 525-544.

135. Violleau, D., et al., *Fouling studies of a polyamide nanofiltration membrane by selected natural organic matter: an analytical approach.* Desalination, 2005. **173**(3): p. 223-238.

136. Contreras, A.E., A. Kim, and Q. Li, *Combined fouling of nanofiltration membranes: Mechanisms and effect of organic matter.* Journal of Membrane Science, 2009. **327**(1-2): p. 87-95.

137. Kim, A.S. and R. Yuan, *Hydrodynamics of an ideal aggregate with quadratically increasing permeability.* Journal of Colloid and Interface Science, 2005. **285**(2): p. 627-633.

138. Kim, A.S., et al., *Fundamental Mechanisms of Three-Component Combined Fouling with Experimental Verification.* Langmuir, 2009. **25**(14): p. 7815-7827.

139. Kim, A.S. and E.M.V. Hoek, *Cake Structure in Dead-End Membrane Filtration: Monte Carlo Simulations.* Environmental Engineering Science, 2002. **19**(6): p. 373-386.

140. Tang, C.Y., Q. Shiang Fu, A. P. Robertson, C.S. Criddle, and J.O. Leckie, *Use of Reverse Osmosis Membranes to Remove Perfluorooctane Sulfonate (PFOS) from Semiconductor Wastewater.* Environmental Science & Technology, 2006. **40**(23): p. 7343–7349.

141. Glauert, A.M. and P.R. Lewis, *Biological specimen preparation for transmission electron microscopy.* 1998, Princeton, NJ: Princeton University Press.

142. Flemming, H.C., et al., *Biofouling--the Achilles heel of membrane processes.* Desalination, 1997. **113**(2-3): p. 215-225.

143. Baker, J.S. and L.Y. Dudley, *Biofouling in membrane systems -- A review.* Desalination, 1998. **118**(1-3): p. 81-89.

144. Cho, J., et al., *Characterization of clean and natural organic matter (NOM) fouled NF and UF membranes, and foulants characterization.* Desalination, 1998. **118**(1-3): p. 101-108.

145. Cho, J., G. Amy, and J. Pellegrino, *Membrane filtration of natural organic matter: initial comparison of rejection and flux decline characteristics with ultrafiltration and nanofiltration membranes.* Water Research, 1999. **33**(11): p. 2517-2526.

146. Rebhun, M. and J. Manka, *Classification of organics in secondary effluents.* Environmental Science & Technology, 1971. **5**(7): p. 606-609.

147. Chen, M.-Y., et al., *Fluorecent Staining for Study of Extracellular Polymeric Substances in Membrane Biofouling Layers.* Environmental Science & Technology, 2006. **40**(21): p. 6642-6646.

148. Combe, C., et al., *The effect of CA membrane properties on adsorptive fouling by humic acid.* Journal of Membrane Science, 1999. **154**(1): p. 73-87.

149. Ostuni, E., et al., *A Survey of Structure-Property Relationships of Surfaces that Resist the Adsorption of Protein.* Langmuir, 2001. **17**(18): p. 5605-5620.

150. Höök, F., et al., *Energy Dissipation Kinetics for Protein and Antibody-Antigen Adsorption under Shear Oscillation on a Quartz Crystal Microbalance.* Langmuir, 1998. **14**(4): p. 729-734.

151. Steiner, Z., J. Miao, and R. Kasher, *Development of an oligoamide coating as a surface mimetic for aromatic polyamide films used in reverse osmosis membranes.* Chemical Communications. **47**(8): p. 2384-2386.

152. Steiner, Z., et al., *Effect of Surface-Exposed Chemical Groups on Calcium-Phosphate Mineralization in Water-Treatment Systems.* Environmental Science & Technology. **44**(20): p. 7937-7943.

153. Jenkins, F.A. and H.E. White, *Fundamentals of Optics.* 4th Ed. ed. 1981: McGraw-Hill Inc.

154. Brunner, H., et al., *Formation of Ultrathin Films at the Solid-Liquid Interface Studied by In Situ Ellipsometry.* Journal of Colloid and Interface Science, 1999. **212**(2): p. 545-552.

155. Tanahashi, M. and T. Matsuda, *Surface functional group dependence on apatite formation on self-assembled monolayers in a simulated body fluid.* Journal of Biomedical Materials Research, 1997. **34**(3): p. 305-315.

156. Rice, G., et al., *Fouling of NF membranes by dairy ultrafiltration permeates.* Journal of Membrane Science, 2009. **330**(1-2): p. 117-126.

157. Broeckmann, A., T. Wintgens, and A.I. Schäfer, *Removal and fouling mechanisms in nanofiltration of polysaccharide solutions.* Desalination, 2005. **178**(1-3): p. 149-159.

158. Myers, J.L. and A.D. Well, *Research Design and Statistical Analysis* 2nd ed, ed. L. Erlbaum. 2003. pp. 508.

159. Herrwerth, S., et al., *Factors that Determine the Protein Resistance of Oligoether Self-Assembled Monolayers â˜ Internal Hydrophilicity, Terminal Hydrophilicity, and Lateral Packing Density.* Journal of the American Chemical Society, 2003. **125**(31): p. 9359-9366.

160. Silin, V., H. Weetall, and D.J. Vanderah, *SPR Studies of the Nonspecific Adsorption Kinetics of Human IgG and BSA on Gold Surfaces Modified by Self-Assembled Monolayers (SAMs).* Journal of Colloid and Interface Science, 1997. **185**(1): p. 94-103.

161. Degefa, T.H., et al., *Elucidation of the electron transfer mechanism of marker ions at SAMs with charged head groups.* Journal of Electroanalytical Chemistry, 2004. **574**(1): p. 49-62.

162. Jin, X., X. Huang, and E.M.V. Hoek, *Role of Specific Ion Interactions in Seawater RO Membrane Fouling by Alginic Acid.* Environmental Science & Technology, 2009. **43**(10): p. 3580-3587.

163. Hashino, M., et al., *Effect of membrane surface morphology on membrane fouling with sodium alginate.* Journal of Membrane Science. **366**(1-2): p. 258-265.

164. Nakata, S., et al., *Chemisorption of proteins and their thiol derivatives onto gold surfaces: characterization based on electrochemical nonlinearity.* Biophysical Chemistry, 1996. **62**(1-3): p. 63-72.

165. Le-Clech, P., V. Chen, and T.A.G. Fane, *Fouling in membrane bioreactors used in wastewater treatment.* Journal of Membrane Science, 2006. **284**(1-2): p. 17-53.

166. Park, N., et al., *Foulants analyses for NF membranes with different feed waters: coagulation/sedimentation and sand filtration treated waters.* Desalination, 2007. **202**(1-3): p. 231-238.

167. Contreras, A.E., et al., *Studying the Impact of Membrane Surface Chemistry on Adsorption and Cleaning of Organic Foulants Using QCM-D* Environ. Sci. Technol., 2011. **In Review**.

168. Van Oss, C.J., R.J. Good, and M.K. Chaudhury, *Additive and nonadditive surface tension components and the interpretation of contact angles.* Langmuir, 1988. **4**(4): p. 884-891.

169. Young, T., *An essay on the cohesion of fluids.* Phil. Trans. R. Soc. Lond., 1805. **95**: p. 65-87.

170. van Oss, C.J., et al., *Influence of macroscopic and microscopic interactions on kinetic rate constants: I. Role of the extended DLVO theory in determining the*

kinetic adsorption constant of proteins in aqueous media, using von Smoluchowski's approach. Colloids and Surfaces B: Biointerfaces, 1999. **14**(1-4): p. 99-104.

171. Hering, J.G. and F.M.M. Morel, *Humic acid complexation of calcium and copper.* Environmental Science & Technology, 1988. **22**(10): p. 1234-1237.

172. van Oss, C.J., R.J. Good, and M.K. Chaudhury, *Solubility of proteins.* Journal of Protein Chemistry, 1986. **5**(6): p. 385-405.

173. van Oss, C.J., M.K. Chaudhury, and R.J. Good, *Monopolar surfaces.* Advances in Colloid and Interface Science, 1987. **28**: p. 35-64.

174. Frank, B.P. and G. Belfort, *Polysaccharides and sticky membrane surfaces: critical ionic effects.* Journal of Membrane Science, 2003. **212**(1-2): p. 205-212.

175. Mänttäri, M., T. Pekuri, and M. Nyström, *NF270, a new membrane having promising characteristics and being suitable for treatment of dilute effluents from the paper industry.* Journal of Membrane Science, 2004. **242**(1-2): p. 107-116.

176. Kwon, Y.-N. and J.O. Leckie, *Hypochlorite degradation of crosslinked polyamide membranes: II. Changes in hydrogen bonding behavior and performance.* Journal of Membrane Science, 2006. **282**(1-2): p. 456-464.

177. Skrovanek, D.J., et al., *Hydrogen bonding in polymers: infrared temperature studies of an amorphous polyamide.* Macromolecules, 1985. **18**(9): p. 1676-1683.

178. Socrates, G., *Infrared Characteristic Group Frequencies.* 1994: Wiley-Interscience.

179. Wu, S., et al., *Chlorination and oxidation of aromatic polyamides. I. Synthesis and characterization of some aromatic polyamides.* Journal of Applied Polymer Science, 1996. **61**(3): p. 415-420.

180. Subramani, A. and E.M.V. Hoek, *Direct observation of initial microbial deposition onto reverse osmosis and nanofiltration membranes.* Journal of Membrane Science, 2008. **319**(1-2): p. 111-125.

181. Van Wagner, E.M., et al., *Surface modification of commercial polyamide desalination membranes using poly(ethylene glycol) diglycidyl ether to enhance membrane fouling resistance.* Journal of Membrane Science. **367**(1-2): p. 273-287.

182. Sadtler, *The Infrared Spectra Atlas of Monomers and Polymers: Sadtler Reserach Laboratories.* 1980.

183. Oh, N.-W., J. Jegal, and K.-H. Lee, *Preparation and characterization of nanofiltration composite membranes using polyacrylonitrile (PAN). II. Preparation and characterization of polyamide composite membranes.* Journal of Applied Polymer Science, 2001. **80**(14): p. 2729-2736.

Nomenclature

<u>**Roman –**</u>

A - piezoelectrically active crystal area (m^2),

A_m - membrane area (m^2)

b - diameter of the composite sphere (m)

C - concentration of the solute (M)

C_b - bulk molar salt concentration (M)

C_m - membrane surface molar salt concentration (M)

C_p - permeate molar salt concentrations (M)

C_{QCM} - mass sensitivity constant based on sensor properties (per overtone number)

d_f - film thickness (m)

d_p - particle diameter (m)

d_l - thickness of adsorbed layer (m)

D - back diffusion coefficient (m^2/s)

D_∞ - bulk diffusion coefficient of the solute (m^2/s)

D^* - effective diffusivity (m^2/s)

ΔD - change in energy dissipation ($\times 10^{-6}$)

Δf - change in resonant frequency (Hz)

f_0 - resonant frequency of the crystal sensor(Hz)

f_{os} - the osmotic coefficient

ΔG^{AB} – Interfacial free energy due to Lewis acid-base contributions (mJ/m^2)

ΔG_{ADH} – Interfacial free energy of adhesion (also ΔG_{LOS}), sum of ΔG_{AB} and ΔG_{LW}

(mJ/m^2)

ΔG_{SL} – Interfacial free energy between the solid (S) and liquid (L) (mJ/m^2)

ΔG^{LW} – Interfacial free energy due to Lifshitz-van der Waals contributions (mJ/m^2)

ΔG_{OLO} – Interfacial free energy of cohesion of the organic (O) in liquid (L) (mJ/m^2)

ΔG_{SLO} – Interfacial free energy of adhesion of organic (O) to surface (S) in liquid (L)

(mJ/m^2)

H – membrane channel height (m)

k - mass-transfer coefficient (m/s)

k_0 - the initial mass-transfer coefficient (m/s)

L - membrane channel length (m)

L_p - permeability of the membrane (m/s·Pa)

m_p - mass of particles deposited on the membrane (kg)

Δm - change in mass adsorbed (kg)

n - overtone number(= 1, 3, 5,…)

ΔP - applied trans-membrane pressure (Pa)

Q - volumetric feed flow rate (m^3/s)

R_c - resistance attributed to the colloidal cake layer (m^{-1})

R'_c - resistance attributed to the colloidal cake layer, including osmotic pressure (m^{-1})

R_{com} - resistance attributed to the combined fouling cake layer (m^{-1})

R'_{com} - resistance attributed to the combined fouling cake layer, including osmotic pressure (m^{-1})

$\bar{R}_c$ - specific resistance of the colloidal cake layer

$\hat{R}_{cg}(\phi_c, \varphi_g)$ - combined fouling layer specific resistance by using a composite cell model approach (m^{-1})

R_{cp} – hydraulic resistances due to the foulant concentration polarization (CP) layers (of both salt ions and foulant particles) (m^{-1})

R_f - hydraulic resistances due to the fouling layer (formed from the rejection of the foulant) (m^{-1})

R_g - resistance due to the organic gel layer (m^{-1})

R'_g - resistance due to the organic gel layer, including osmotic pressure (m^{-1})

R_i – intrinsic salt rejection

R_m - hydraulic resistance due to the membrane (m^{-1})

R'_m - resistance attributed to the membrane and the concentration polarization layer at the end of the conditioning phase (m^{-1})

R_o - observed salt rejection

ΔS_{ads} – change in entropy of adsorption (J/kg/mol)

T - absolute temperature (K)

W – membrane channel width (m)

Greek -

α - factor corresponding to the permeability composite layer

β - factor corresponding to the permeability composite layer

γ^{AB} - Lewis acid-base parameter of the surface tension (mJ/m^2)

γ^{LW} - Lifshitz-van der Waals parameter of the surface tension (mJ/m^2)

γ^{TOT} - Sum of all surface tension parameters (LW and AB) (mJ/m^2)

γ^+ - electron-acceptor parameter of the surface tension (mJ/m^2)

γ^- - electron-donor parameter of the surface tension (mJ/m^2)

ε - porosity of the cake layer

ε_c - cake layer porosity

ζ – surface zeta potential (mV)

κ_B - Boltzmann constant (1.38 × 10^{-23} m^2 kg/s^2/K)

η_f – film viscosity (Pa·s)

η_l - viscosity of the adsorbed layer (Pa·s)

θ - water contact angle (°)

μ - solution viscosity (Pa·s)

μ_f – film elastic modulus (Pa)

μ_q - shear modulus of quartz (Pa)

μ_l - shear elastic modulus of adsorbed layer (Pa)

v - permeate flux (m^3/m^2·s)

v_c – permeate flux due to inorganic colloids alone (m^3/m^2·s)

v_{com} – permeate flux due to combined foulants in solution (m^3/m^2·s)

v_0 - flux of clean water (m³/m²·s)

$v_{eq}^{`}$ - the strong form of the equivalent flux, assumes that the flux of a combined solution (v_{com}) is equivalent to the sum of the fluxes of the individual components

v_g - the flux due to organic alone (m³/m²·s)

v_w - membrane permeate flux during filtration (m³/m²·s)

$\bar{v}$ - permeate flow velocity (m³/m²·s)

$\Delta\pi_m$ - trans-membrane osmotic pressure due to rejection increasing the concentration of salt ions (Pa)

ρ_l - density of adsorbed layer (kg/m³)

ρ_p - density of the particles (kg/m³)

ρ_f – film density (kg/m³)

ρ_q - density of quartz (kg/m³),

τ - tortuousity

ϕ_c - volume fraction of the colloid

φ_g - volume fraction of the organic

Ω_{KY} - Happel's correction factor

Abbreviations –

AFM – Atomic force microscopy

ALG – Sodium alginate, model organic foulant

ATR-FTIR – Attenuated total reflectance – Fourier transform infrared spectroscopy

BSA – Bovine serum albumin, model organic foulant

CECP – Cake-enhanced concentration polarization (same as CEOP)

CEOP – Cake-enhanced osmotic pressure (same as CECP)

CP – Concentration polarization

DEX – Dextran, model organic foulant

DI – De-ionized (water)

DLS – Dynamic light scattering

DLVO – Derjaguin, Landau, Verwey and Overbeek theory

EDCs – Endocrine disrupting compounds

EDTA - Ethylenediaminetetraacetic acid

EPS – Extracellular polymeric substances

HA – Suwannee River humic acid, Standard II

IEP – Iso-electric point

LFC1 – High salt rejecting RO membrane (Hydranautics, Nitto Denko, Oceanside, CA)

MF – Microfiltration

MPD - m-Phenylenediamine

MWCO – Molecular weight cut-off

NF – Nanofiltration

NF270 – Low salt rejecting NF membrane (Dow-FilmTec, Minneapolis, MN)

NOM – Natural organic matter

PPMC – Pearson product-moment coefficient

PES – Polyethersulfone

PSf - Polysulfone

PVA – Polyvinyl alcohol

QCM – Quartz crystal microbalance

QCM-D – Quartz crystal microbalance with dissipation monitoring

RO – Reverse osmosis

SAM – Self-assembled monolayer

SDS – Sodium dodecyl sulfate

SEM – Scanning electron microscopy

SPR – Surface plasmon resonance

SRHA – Suwannee river humic acid (Standard II), model organic foulant

ST-XL – Snowtex – XL, colloidal silica, model inorganic foulant

TEM – Transmission electron microscopy

TFC – Thin-film composite

TMC - Trimesoyl chloride

TOC – Total organic carbon

UF - Ultrafiltration

XPS – X-ray photoelectron spectroscopy

xDVLO – Extended DLVO theory

Appendix A – Complete Characterization of Model Foulants

<u>Alginate:</u>

Particle Size of ST-XL & Alginate Solutions in 10 mM NaCl

Particle Diameter of ST-XL & Alginate Solutions in 7 mM NaCl/1 mM CaCl$_2$

Zeta Potential of ST-XL & Alginate Solutions in 10 mM NaCl

Zeta Potential of ST-XL & Alginate Solutions in 7 mM NaCl/1 mM CaCl$_2$
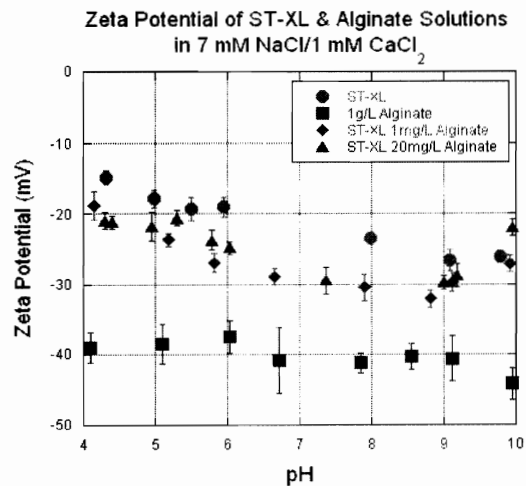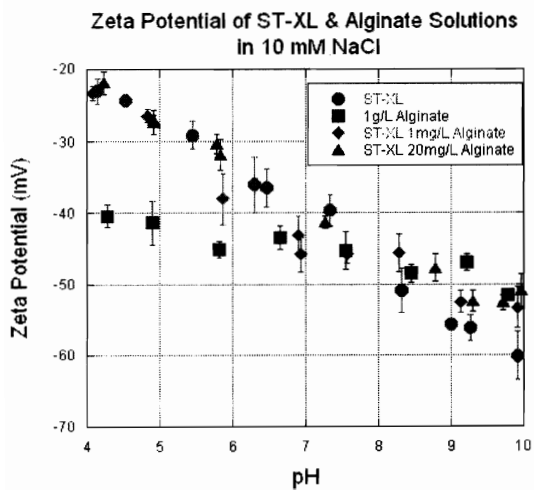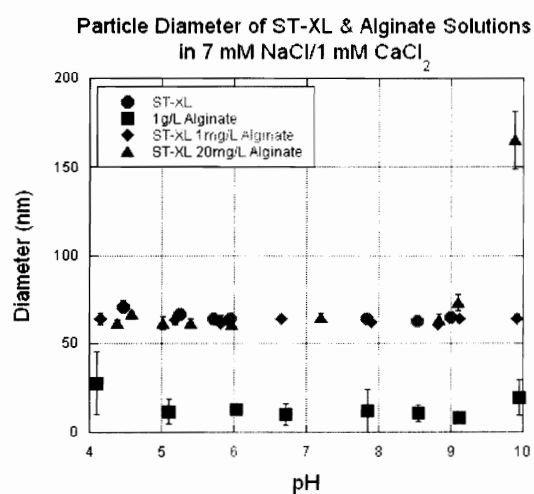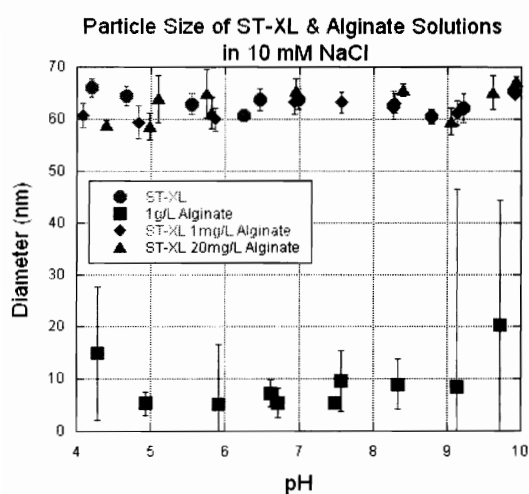
Bovine Serum Albumin (BSA):

Zeta Potential of ST-XL & BSA Solutions in 10 mM NaCl
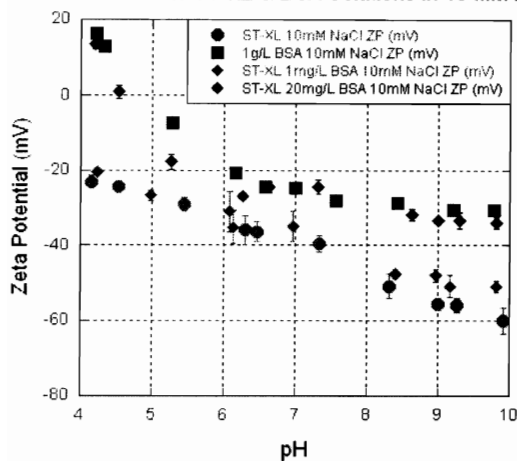
Particle Size of ST-XL & BSA Solutions in 10mM NaCl
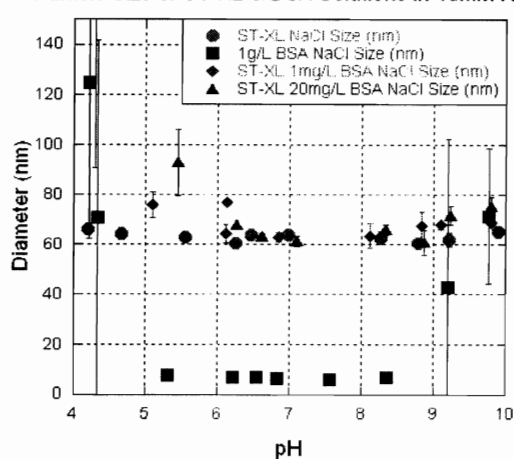
Zeta Potential of ST-XL & BSA Solutions in 7mM NaCl/1mM CaCl2
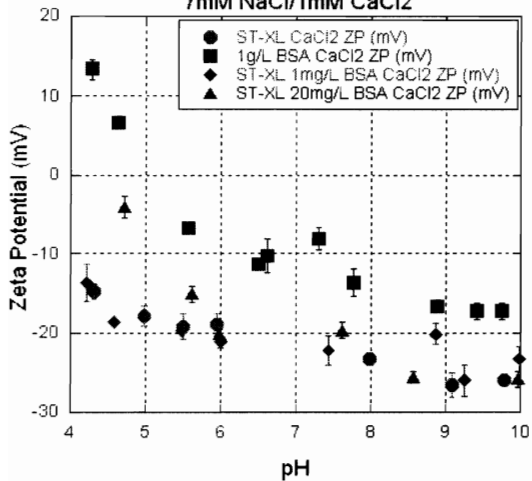
Particle Size of ST-XL & BSA Solutions in 7mM NaCl/1mM CaCl2

Dextran:

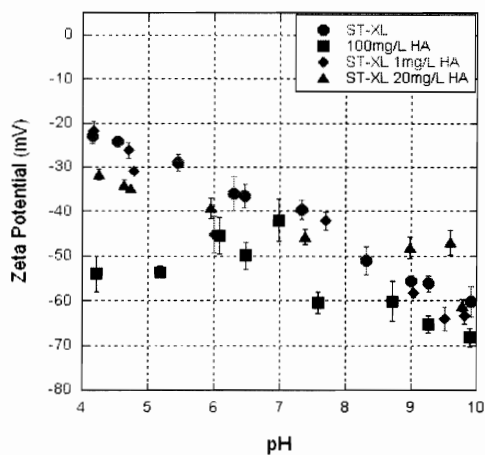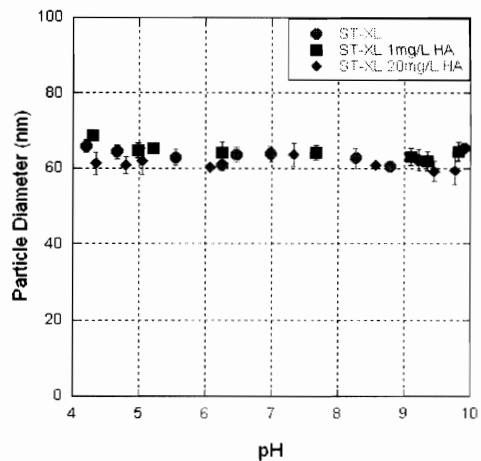### Zeta Potential of ST-XL & Dextran Solutions in 10 mM NaCl

Legend:
- ST-XL 10mM NaCl ZP (mV)
- 1g/L Dex Ave 10mM NaCl ZP (mV)
- 0.5g/L Dex 410' 10mM NaCl ZP (mV)
- ST-XL 1mg/L Dex 10mM NaCl ZP (mV)
- ST-XL 20mg/L Dex 10mM NaCl ZP (mV)

Particle Size of ST-XL & Dextran Solutions in 10 mM NaCl

Legend:
- ST-XL NaCl Size (nm)
- 1g/L Dex Ave NaCl Size (nm)
- ST-XL 1mg/L Dex NaCl Size (nm)
- ST-XL 20mg/L Dex NaCl Size (nm)
- 0.5 g/L Dex 410' NaCl Size (nm)

Zeta Potential of ST-XL & Dextran Solutions in 7 mM NaCl/1 mMCaCl2

Legend:
- ST-XL CaCl2 ZP (mV)
- 1g/L Dex Ave CaCl2 ZP (mV)
- ST-XL 1mg/L Dex CaCl2 ZP (mV)
- ST-XL 20mg/L Dex CaCl2 ZP (mV)
- 0.5 g/L Dex 410' CaCl2 ZP (mV)

Particle Size of ST-XL & Dextran Solutions in 7 mM NaCl/1 mM CaCl2

Legend:
- ST-XL CaCl2 Size (nm)
- 1g/L Dex Ave CaCl2 Size (nm)
- ST-XL 1mg/L Dex CaCl2 Size (nm)
- ST-XL 20mg/L Dex CaCl2 Size (nm)
- 0.5 g/L Dex Ave CaCl2 Size (nm)

Humic Acid (HA):

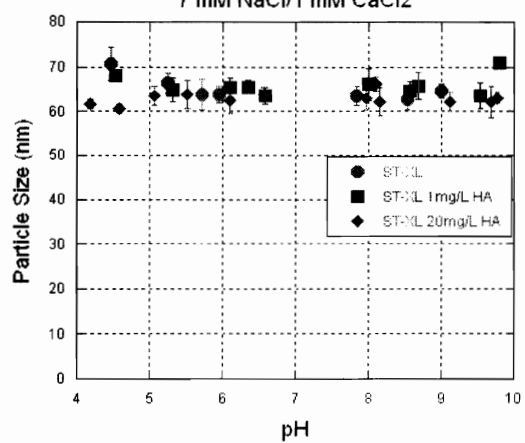Zeta Potential of ST-XL & HA Solutions in 10 mM NaCl

Particle Diameter of ST-XL & HA Solutions in NaCl

Zeta Potential of ST-XL & HA Solutions in 7 mM NaCl/ 1 mM CaCl2
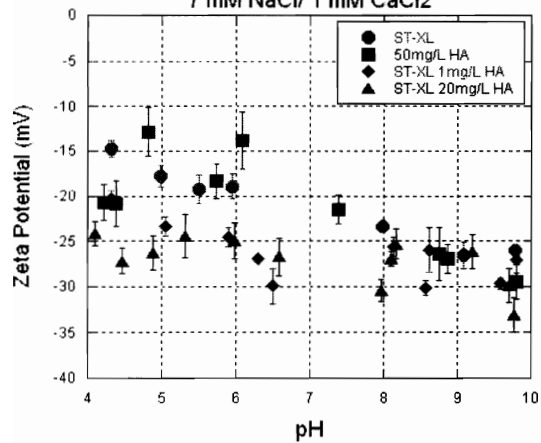
Particle Diameter of ST-XL & HA Solutions in 7 mM NaCl/1 mM CaCl2

Appendix B – Statistical Tools

1. **<u>Pearson product moment correlation coefficient (PMCC)[30]-</u>**

PMCC is a measure of the strength of correlation (or linear dependence) of two variables, between -1 (highly negatively correlated) and +1 (highly positively correlated). A PMCC of 0 represents zero linear correlation. The PMCC ($\rho_{X,Y}$) is calculated by the covariance (*cov*) of two variables (*X* and *Y*) divided by the product of their standard deviations (σ):

$$\rho_{X,Y} = \frac{\text{cov}(X,Y)}{\sigma_X \sigma_Y}$$

Large correlation is considered to be a PMCC value between -0.5 and -1 or 0.5 and 1.

2. **<u>Spearman's rank correlation coefficient[158] –</u>**

Spearman's rank (ρ_S) is a measure of strength of correlation between two variables (X_i and Y_i) that can be described by any monotonic function, as opposed to only a linear function as described by the PMCC. Assuming no tied variables:
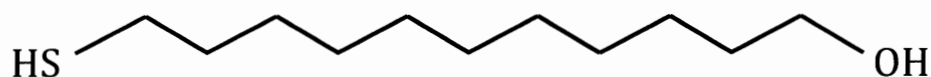
$$\rho_S = 1 - \frac{6\sum d_i^2}{n(n^2 - 1)}$$

where $d_i = x_i - y_i$, the difference between the ranks (x_i, y_i) of variables (X_i, Y_i) and n is the sample number. Significance is determined using the student t-test with $n-2$ degrees of freedom under the null-hypothesis.

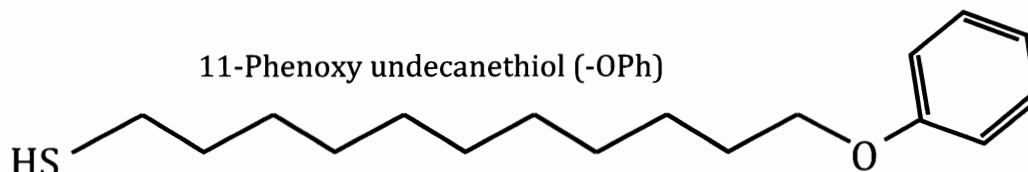# Appendix C – Chemical Structure of Alkanethiols Used in SAMs
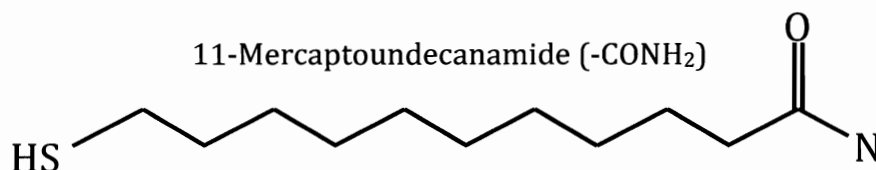
1-Dodecanethiol (-CH_3)
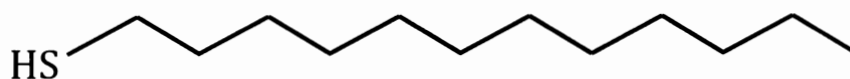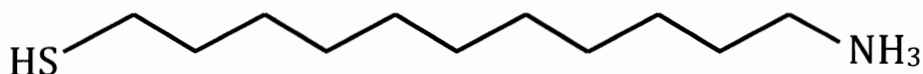
11-Hydroxy-1-Undecanethiol (-OH)
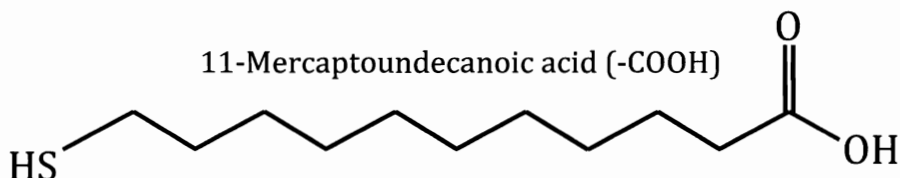
11-Phenoxy undecanethiol (-OPh)
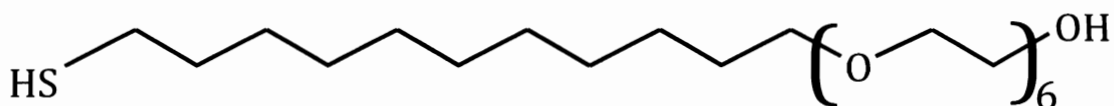
11-Mercaptoundecanamide (-$CONH_2$)

11-Amino-1-undecanethiol, hydrochloride (-NH_2)

11-Mercaptoundecanoic acid (-COOH)

(1-Mercapto-11-undecyl)hexa(ethylene glycol) (-EG_6OH)

Appendix D - Fundamental Mechanisms of Three-Component Combined Fouling with Experimental Verification

Albert S. Kim,*,† Alison E. Contreras,‡ Qilin Li,‡ and Rong Yuan†

†Department of Civil and Environmental Engineering, University of Hawaii at Manoa, 2540 Dole Street, Holmes Hall 383, Honolulu, Hawaii 96822, and ‡Department of Civil and Environmental Engineering, Rice University, 6100 Main MS-318, Houston, Texas 77005

Abstract.

The present article describes a novel fundamental theory for investigating combined fouling by colloids (ST-XL), macromolecules, and solute ions (NaCl). Three macromolecules were used for the combined fouling study, bovine serum albumin (BSA), alginate, and dextran. The presented theory unifies singlet, doublet, and triplet fouling phenomena, including cake-enhanced osmotic pressure and binary colloidal fouling models, giving rise to the combined flux equation for three-component fouling assuming a completely mixed fouling layer. The predicted combined flux was compared to two equivalent fluxes calculated from individual foulant contributions. The strong form of the equivalent flux, known as the additive flux, was based on a linear superposition of flux decline due to individual foulants. The weak form of equivalent flux assumed stratification of individual foulant layers and hence a linear superposition of the individual fouling resistance. A comparison

of experimental data and theoretical calculations revealed that the weak form of equivalent flux and the combined flux that was predicted by the novel theory provided the upper and lower limits, respectively, of the observed permeate flux. Furthermore, the model simulation results suggested a structural compression of the BSA gel layer, where as such a compression did not occur in cases of alginate and dextran. The gel concentrations of alginate and dextran in the combined fouling layer seemed to be less than those in the macromolecular gel layer.